15 JUNE 1963 TO 15 AUGUST 1964

FINAL REPORT

HOLLOW GLASS FIBER REINFORCED LAMINATES

Contract NOw-63-0674-c

SPACE SCIENCES
LABORATORY

MISSILE AND SPACE DIVISION

GENERAL ELECTRIC

HOLLOW GLASS FIBER REINFORCED LAMINATES

Prepared under U. S. Navy, Bureau of Naval Weapons

Contract NOw-63-0674-c

Final Report

15 June 1963 through 15 August 1964

MECHANICS SECTION

Space Sciences Laboratory
Missile and Space Division
General Electric Company
Box 8555, Philadelphia 1, Pa.

TABLE OF CONTENTS

SCOPE

Previous studies of hollow glass fiber reinforced plastics (ref. 1) have indicated that these composites offer the potential of significant structural weight savings for structures which are design limited by compressive strength or stability considerations or by bending or deflection criteria. The improved performance of these materials under uniaxial compressive loads was demonstrated. Performance of the hollow fiber composites under certain conditions of bi-axial or tri-axial states of stress was also treated theoretically, although experimental verification was lacking. One of the purposes of the present program was to perform mechanical tests of structural elements having bi-axial stiffening subjected to various loads in order to demonstrate the expected performance. Tests of shells subjected to internal and external pressure and to axial compression were performed. The experimental results were compared with analytical results for elastic moduli and failure.

A second major area of the present program is the consideration of hollow fiber composites subjected to thermal and electrical environments. The demonstration of properties differing significantly from those of equivalent solid fiber composites would offer the potential of additional applications. Thermal properties were studied both theoretically and experimentally and electrical properties were measured experimentally.

This report on the accomplishments of the present program consists of two parts. The first presents the development of new analytical tools for the evaluation of composite performance. Included in this section are analyses

relating the thermal expansion coefficients and thermal conductivities of a fibrous composite to those of the constituents. Also, further study of the stresses in the vicinity of a fiber discontinuity are presented.

The second phase of the report describes the experimental program including mechanical, thermal and electrical property measurements. Test results are compared with analytical results where possible. The results indicate potential for application of the material to new areas.

RESULTS AND RECOMMENDATIONS

This report presents the results of the first phase of a study to evaluate the properties of hollow glass fiber reinforced plastics for potential application in thermal and electrical as well as various mechanical functions. The overall program, as initially formulated, includes analytical and experimental studies of various composite properties. The initial phase, reported herein, consists of an exploratory treatment of pertinent material properties. The results, as discussed below in detail, indicate certain areas in which theory and experiment are in agreement and others in which presently unexplainable incompatibilities between theory and experiment exist. It appears that further study of fabrication techniques for the hollow fibers and the hollow fiber composite are required, as well as a more detailed investigation of composite properties.

The test program was performed with three major objectives. First, to compare the properties of hollow fiber composites with those of similar (same matrix geometry and properties) solid fiber composites; second to compare theoretical and experimental results; and third, to provide initial property data for use in other evaluations.

One of the major areas of investigation was the study of thermal properties. Thermal conductivity in directions parallel and normal to the fiber direction was evaluated analytically and experimentally. Conductivity transverse to the fibers of a hollow fiber composite was found to be substantially lower than that of an equivalent solid fiber composite. All experimental thermal

conductivity values were slightly lower than the analytical values. The analytical assumption of perfect thermal contact at the internal interfaces may explain this discrepancy. However, the magnitude of the effect is small so that the analytical results are a valid estimate of the composite properties.

Thermal expansion measurements indicated large differences between hollow and solid composites with the hollow fiber results being higher. An analysis was developed relating composite longitudinal and transverse expansion coefficients to constituent properties. The results agree well with the experimental results for solid fiber composites, but predict a small difference in properties for hollow and solid fiber composites while experimental differences are very large. The lack of agreement between theory and experiment for hollow fiber composite expansion coefficients, particularly in the longitudinal (or fiber) direction, is unexpected and not readily explained. The possibility of fiber damage during fabrication must be considered.

Ablation tests were performed on similar hollow and solid fiber composites. Hollow fibers showed a small improvement relative to solid fibers but did not compare well with previous phenolic nylon results. However, a better configuration having the hollow fibers at a small angle to the specimen surface (say 10° - 20°) could be expected to take better advantage of the low transverse thermal conductivity and yet utilize the high longitudinal strength. Specific heat and thermogravimetric measurements were also performed and the results are presented.

Electrical properties were measured to assess the potential of hollow fiber composites for radome and other similar applications. Results show that the hollow fiber materials are better transmitters of incident electromagnetic energy than are solid fiber materials. The relative dielectric constants for the samples tested remained essentially constant in the frequency ranges tested. As expected, the absolute values are between the values for pure glass and pure epoxy resin.

The experimental values for electromagnetic energy absorption show that solid glass materials absorb more than the hollow with both showing decreasing absorption with increasing frequency.

No fiber orientation effects on test results were observed, primarily because the fiber spacing is too small to be resolved by the test frequencies used.

Mechanical property measurements were made under loading conditions which simulated a variety of structural applications. Also analytical studies of the internal stresses were extended, and the effect of inelastic matrix materials was considered. There was no experimental verification of these latter results. Internal and external pressure tests of hollow and solid fiber laminated shells were performed.

Internal pressure tests to evaluate tensile strength of the fibers in a composite gave lower values than expected. Though fiber damage prior to winding, caused by poor packaging, can explain some of the reduction, vessel preparation techniques also caused problems and could account for part of the

poorer than expected test results.

External hydrostatic pressure tests were used to evaluate structural efficiencies of the hollow and solid fiber materials and to evaluate some composite physical properties. Here again, poor specimen fabrication hampered the experimental program but some quantitative values for composite physical constants were obtained.

Axial compression tests of filament wound cylindrical shells were performed. The results were compared with theoretical treatments developed under another program. Remarkable agreement was evidenced between theoretical and experimental buckling loads. However, the associated elastic constants did not correlate well. The analyses are subject to the uncertainties resulting from air inclusions caused by the fabrication process. It does appear that the triaxial (or "isotropic") laminate provides maximum resistance to elastic instability of cylindrical shells in axial compression. It also appears that the theoretical expectations of improved performance of hollow fiber composites, relative to similar solid fiber composites, in this loading condition are achieved.

Fatigue tests were also performed. Using the Prot-Wohler progressive stress technique the endurance limits for the solid fiber and hollow fiber laminates were investigated. Solid fiber composite endurance limits were found to be approximately 37% greater than for hollow fiber composites, which means that the hollow fiber material has a slightly higher endurance limit to density ratio.

On an equal weight basis, hollow fiber composites were shown to have superior mechanical strength, mechanical rigidity, thermal insulation, and electrical transparency properties. Many of these improvements can be adequately predicted analytically, but experimental and analytical results for other properties did not agree, thus requireing additional investigation. The analyses, in general, indicate that when hollow fiber composites are better than solid fiber composites, fibers of greater hollowness (larger ratio of inner to outer fiber radii) than those presently available are desirable.

Accordingly it is recommended that:

1. The indicated benefits associated with the use of hollow glass fibers for selected thermal, electrical, and mechanical applications should be pursued with particular emphasis on achieving reliable composites with fibers of higher hollowness (larger ratio of inner to outer fiber diameters).

2. Fabrication techniques for producing consistent hollow fibers and composites utilizing them should be explored to assess ways of minimizing fiber damage and deviations from nominal geometry.

I. THEORETICAL STUDIES

Studies of the relationship between constituent thermal properties and composite thermal properties have been performed during this contract period. The thermal conductivity and thermal expansion coefficient in directions parallel and normal to the fibers of a matrix reinforced by a uniaxial set of fibers have been evaluated. In addition, further consideration has been given to the influence of hollow fibers upon the tensile strength of glass reinforced plastics. The effect of fiber shape on internal stresses was treated. These studies are described below.

A. Thermal Conductivity

The thermal conductivity of hollow glass fiber reinforced composites with parallel fibers has been defined. The thermal conductivity of an homogeneous and isotropic material is defined by the relation

$$q = -k \nabla T \tag{1}$$

where q is the heat flux vector, k the conductivity and ∇T is the gradient of the temperature, T. For an anisotropic materials (1) has to be replaced by a tensorial relation of the form

$$q_i = -k_{ij} \frac{\partial T}{\partial x_j} \tag{2}$$

where i, j are subscripts of range 1, 2, 3 referring to Cartesian coordinates and the repeated subscript denotes summation.

The effective thermal conducitivity of a heterogeneous material which is statistically homogeneous will be defined in analogy with effective elastic moduli of such materials. The definition is:

$$q_i = -k^*_{ij} \frac{\overline{\partial T}}{\partial x_j} \tag{3}$$

and is restricted to the case of heterogeneous bodies with boundary conditions which would produce space constant heat flux fields and space constant temperature gradient fields in homogeneous bodies. Such boundary conditions are:

(a) Linear temperature variation prescribed over entire boundary.

(b) Constant heat flux vector prescribed over entire boundary.

The overbars in (3) denote volume averages over regions large compared to the inhomogeneities size. In accordance with previous work such regions are called representative volume elements, (RVE). Because of the boundary conditions (a) or (b) and the assumed statistical homogeneity of the material, the RVE averages are in the limit equal to body averages. The k^*_{ij} are then the components of the effective conductivity tensor.

The fiber reinforced material, to be investigated here is transversely isotropic. Choosing x in fiber direction and x_2 and x_3 in the transverse plane, eqs. (3) reduce to

$$\overline{q}_1 = -k^*_1 \frac{\overline{\partial T}}{\partial x_1} \tag{4}$$

$$\overline{q}_2 = -k^*_2 \frac{\overline{\partial T}}{\partial x_2} \tag{5}$$

$$\bar{q}_3 = -k_t^* \frac{\overline{\partial T}}{\partial x_3} \tag{6}$$

where

$$k_t^* = k_2^* = k_3^* \tag{7}$$

Derivation of expressions for k_l^* and k_t^* is based on hypothetical steady conductivity experiments, performed on a cylindrical specimen of the composite whose generators are in fiber direction. The specimen is assumed to be very long in comparison to fiber cross sections and contains a very large amount of fibers which extend from base to base.

It can readily be shown that the effective longitudinal conductivity is given by:

$$k_l^* = k_b v_b + k_f v_f \tag{8}$$

where v_b and v_f are the fractional volumes of binder and fiber materials, respectively.

For analysis of the transverse conductivity problem, leading to an expression for k_t^*, the composite cylinder approximation will again be introduced. Consider a very long composite cylinder, containing one central fiber. On the outer boundary a linear temperature is prescribed, i.e.

$$T_{(r=r_b)} = -\mu x_2 = -\mu r_b \cos\theta \tag{9}$$

where μ is a constant. There are two different temperature fields, T_b and T_f, in binder and fiber region, respectively. Both have to satisfy the heat conduction equation and the continuity conditions at the fiber-binder interface.

Only the radial heat flux on the boundary $r=r_b$ is needed. This is found to be

$$q_{r_{(r=r_b)}}^{b} = -\mu m \cos\theta \tag{10}$$

where

$$m = \frac{\eta(1-\alpha^2)(1+\beta^2) + (1+\alpha^2)(1-\beta^2)}{\eta(1-\alpha^2)(1-\beta^2) + (1+\alpha^2)(1+\beta^2)} k_b \tag{11}$$

Here

$$\eta = \frac{k_f}{k_b}$$

$$\alpha = \frac{r_o}{r_f} \tag{12}$$

$$\beta = \frac{r_f}{r_b}$$

Because of the relation (1) it is not difficult to realize that (9) and (10) are equivalent to the solution for a homogeneous cylinder of radius r_b with conductivity m. Assume that an homogeneous cylindrical specimen of conductivity m is subjected to constant transverse temperature gradients and hence constant heat fluxes. If a cylindrical region, extending from base to

base is replaced by a composite cylinder of the kind analyzed here, the material will not know the difference since the radial heat flux and the temperature will remain the same on the cylinder boundary. Such replacements can then be made indefinitely (conserving the ratios $r_o:r_f:r_b$ and binder and fiber conductivities). Going to smaller and smaller replacing cylinders, the specimen can in the limit be replaced entirely by such composite cylinders, the conductivity remaining the same. Thus, it has been shown that there exists a special fiber reinforced material whose transverse conductivity is m. It may be assumed that for any fiber reinforced material the transverse conductivity is then approximately m. Thus

$$k_t^* = k_b \frac{\eta (1 - \alpha^2) (1 + v_t) + (1 + \alpha^2) v_b}{\eta (1 - \alpha^2) v_b + (1 + \alpha^2) (1 + v_t)} \tag{13}$$

where v_b is the fractional volume of binder and v_t that of gross fiber material (including voids).

This analysis has been used to obtain the effective longitudinal and transverse thermal conductivities for hollow glass reinforced plastic with a binder volume fraction of 0.3. The results are presented in fig. 1.

B. Thermal Expansion Coefficient

The evaluation of the effective thermal expansion coefficients of a hollow fiber composite will be based on the mechanical model of the material which was used in the evaluation of the elastic constants (ref. 16). The

material treated is a homogeneous isotropic matrix reinforced by uniaxially oriented hollow fibers. The material in cross-section is considered to be divided so that each fiber is surrounded by a portion of the matrix with the ratio of areas of the two constituents the same as their respective volume fractions in the composite. Each portion of the matrix material is then approximated by a circular cylinder of the same volume which is concentric with the fiber. The approximation inherent in the final result is that associated with this geometric approximation. The results are exact for the special material composed of a set of composite cylinders of varying diameters, from some finite maximum size to vanishingly small size, arranged to fill the entire volume. Each of the composite cylinders contains a fiber surrounded by binder material with the relative volume fractions the same for all cylinders.

When these composite cylinders are subjected to a uniform temperature increase, each cylinder will have the same average transverse strain, since the relative proportions of the constituents are the same. Thus, all cylinders which formed a continuous medium before temperature increase, will also form a continuous medium after temperature increase with zero tractions on the outer cylindrical surface of each composite cylinder. When the elasticity solution for an individual cylinder is known, these stresses and displacements will then form a compatible set which satisfies equilibrium for the entire composite. The average strains in the longitudinal and transverse directions in each cylinder will then be given by $\bar{\alpha}_L \Delta T$ and $\bar{\alpha}_T \Delta T$, respectively, where ΔT is the uniform temperature rise and $\bar{\alpha}_L$ and $\bar{\alpha}_T$ are the

desired average longitudinal and transverse coefficients of thermal expansion.

The analysis follows that for loads applied to a composite cylinder as presented in ref. 1 with the stress-strain relations modified to include temperature terms. Thus:

$$\epsilon_r = \frac{1}{E}\left[\sigma_r - \nu(\sigma_\theta + \sigma_z)\right] + \alpha \Delta T \tag{14}$$

$$\epsilon_\theta = \frac{1}{E}\left[\sigma_\theta - \nu(\sigma_z + \sigma_r)\right] + \alpha \Delta T \tag{15}$$

$$\epsilon_z = \frac{1}{E}\left[\sigma_z - \nu(\sigma_\theta + \sigma_r)\right] + \alpha \Delta T \tag{16}$$

Neglecting edge effects the longitudinal strain, ϵ_L, is constant and given by (see e.g. ref. 17):

$$\epsilon_{Lf} = \frac{\sigma_{Lf}}{E_f} - \frac{2\nu_f}{E_f}\left(\frac{p r_f^2}{r_f^2 - r_o^2}\right) + \alpha_f \Delta T \tag{17}$$

for $r_o \leq r \leq r_f$

$$\epsilon_{Lb} = \frac{\sigma_{Lb}}{E_b} + \frac{2\nu_b}{E_b}\left(\frac{p r_f^2}{r_b^2 - r_f^2}\right) + \alpha_b \Delta T \tag{18}$$

for $r_f \leq r \leq r_b$

where p = interface radial stress.

The radial displacements, u, are similarly given by:

$$u_f = \frac{1 - \nu_f}{E_f}\left(\frac{p r r_f^2}{r_f^2 - r_o^2}\right) + \frac{1 + \nu_f}{r E_f}\left(\frac{p r_o^2 r_f^2}{r_f^2 - r_o^2}\right) - \nu_f r \frac{\sigma_{Lf}}{E_f} + \alpha_f r \Delta T \quad (19)$$

for $r_o \leq r \leq r_f$

$$u_b = -\frac{1 - \nu_b}{E_b}\left(\frac{p r r_f^2}{r_b^2 - r_f^2}\right) - \frac{1 + \nu_b}{r E_b}\left(\frac{p r_f^2 r_b^2}{r_b^2 - r_f^2}\right) - \nu_b r \frac{\sigma_{Lb}}{E_b} + \alpha_b r \Delta T \quad (20)$$

for $r_f \leq r \leq r_b$

For compatibility:

$$u_f(r_f) = u_b(r_f) \quad (21)$$

and $$\epsilon_{Lf} = \epsilon_{Lb} = \epsilon_L \quad (22)$$

For equilibrium:

$$v_f \sigma_{Lf} + v_b \sigma_{Lb} = 0 \quad (23)$$

Substitution of eqs. (17) - (20) into eqs. (21) - (23) yields a set of three equations in the three unknown stresses, σ_{Lf}, σ_{Lb} and p. The solutions can then be substituted into eqs. (18) and (20) in order to obtain the effective expansion coefficients which are defined by:

$$\bar{\alpha}_L \equiv \frac{\epsilon_L}{\Delta T} \quad (24)$$

and $$\bar{\alpha}_T \equiv \frac{u_b(r_b)}{r_b \Delta T} \quad (25)$$

The results are given by:

$$\bar{\alpha}_L = \frac{\alpha_f - \alpha_b}{E\,(A\phi_2 - B\phi_1)} \left\{ \frac{1 + \nu_f}{v_f E_f} \left[v_f + 2v_o - 2\nu_b (v_f + v_o) \right] + \frac{1 + \nu_b}{v_b E_b} \left[1 + v_f + v_o - 2\nu_b (v_f + v_o) \right] \right\} + \alpha_b \qquad (26)$$

$$\bar{\alpha}_T = \frac{\alpha_f - \alpha_b}{E_b (A\phi_2 - B\phi_1)} \left\{ \frac{1 + \nu_f}{v_f E_f} \left[2(v_f + v_o) - \nu_b (v_f + 2v_o) \right] + \frac{1 + \nu_b}{v_b E_b} \left[2(v_f + v_o) - \nu_b (1 + v_f + v_o) \right] \right\} + \alpha_b \qquad (27)$$

where

$$A = \frac{1}{E_f} \left(\frac{v_f + 2v_o}{v_f} \right) - \frac{\nu_f}{E_f} + \frac{1}{E_b} \left(\frac{1 + v_f + v_o}{v_b} \right) + \frac{\nu_b}{E_b}$$

$$B = \frac{2\nu_f}{E_f} \left(\frac{v_f + v_o}{v_f} \right) + \frac{2\nu_b}{E_b} \left(\frac{v_f + v_o}{v_b} \right)$$

$$\phi_1 = \frac{\nu_b}{E_b} + \frac{\nu_f}{E_f} \left(\frac{v_b}{v_f} \right)$$

$$\phi_2 = \frac{1}{E_b} + \frac{1}{E_f} \left(\frac{v_b}{v_f} \right)$$

The variation of expansion coefficients with binder volume fraction for solid and hollow glass fiber reinforced epoxy is shown in fig. 2. The effect of fiber hollowness is shown in fig. 3.

C. Internal Stresses

The effect of fiber hollowness upon tensile strength of uniaxially oriented glass fiber reinforced plastics has been explored further, following the failure model proposed in ref. 2. This model treats the fibers as having a statistical distribution of flaws or imperfections which result in fiber failure at various stress levels well below the ultimate failure stress level of the composite. In the vicinity of these internal breaks, the axial load carried by the fiber is transmitted by shear through the matrix to adjacent fibers. A portion of the fiber at each break is therefore not fully effective in resisting the applied stress. As the composite stress is increased, there will be an increasing accumulation of fiber fractures and two possible events can occur. One possibility is that the interface shear stress may increase to reach the strength of the interface bond causing an interface failure which would result in the fractured fibers being totally ineffective in carrying load. A second possibility is then an increasing number of ineffective fiber lengths, at the fiber breaks, may combine to produce a weak surface. Either event can result in composite failure and both the magnitude of the interface shear stress and the ineffective length at a fiber break are important measures of the tensile strength of a fibrous composite.

The computation of stress in the vicinity of a discontinuous fiber is quite complex, and an exact solution for the complex geometry which exists appears to be unattainable from a practical veiwpoint. Such stresses were evaluated (ref. 3) for idealized fiber shape and without the effect of surrounding

fibers. Approximations based on a shear lag type of analysis appear to be a reasonable approach for the inclusion of adjacent fibers. Shear lag analyses for similar problems have been performed in refs. 4 and 5. The former treated two concentric cylinders representing fiber and binder; the latter treated a two-dimensional fibrous composite. In the present model, as shown in fig. 4, the fiber and binder are surrounded by an average material with the effective elastic properties of the composite. The extensional stresses in the matrix are neglected relative to those in the fiber and the shear strains in the fiber are neglected relative to those in the matrix. The shear strains in the average material are assumed to decay in a negligible distance from the inclusion interface. These assumptions are considered appropriate for fibers which are very strong and stiff relative to the matrix. The shear stresses, τ, which result from this analysis, are given by:

$$\frac{\tau}{\sigma_{fo}} = \frac{1}{2}\left(\frac{G_b}{E_f}\right)^{1/2}\left(\frac{v_t^{1/2}}{1 - v_t^{1/2}}\right)^{1/2}(1 - \alpha^2)^{1/2}(\cosh \beta_1 x - \sinh \beta_1 x) \quad (28)$$

where

$$\beta_1^2 = \frac{G_b}{E_f}\left(\frac{v_t^{1/2}}{1 - v_t^{1/2}}\right)\left(\frac{1}{r_f}\right)^2\left(\frac{1}{1 - \alpha^2}\right)$$

G_b = shear modulus of binder

E_f = Young's modulus of fiber

v_t = gross volume fraction of fibers ($v_t = 1 - v_b$)

x = distance from fiber end

σ_{fo} = extensional stress in the fiber at a large distance from the fiber end

Similarly, the variation of extensional stress in the fiber is found to be:

$$\frac{\sigma_f}{\sigma_{fo}} = 1 + \sinh \beta_1 x - \cosh \beta_1 x \qquad (29)$$

The fiber extensional and interface shear stress are plotted in fig. 5 for hollow and solid glass fibers. It can be seen that the shear stresses are quite localized and decay within several fiber diameters, at which point the fiber stresses approach their undisturbed value, σ_{fo}. The fiber ineffective length can be quantitatively defined by specifying some fraction, ϕ, of the undisturbed stress value below which the fibers shall be considered ineffective. The fiber ineffective length, δ, can then be shown to be (when normalized with respect to the fiber diameter, d_f):

$$\frac{\delta}{\varphi_f} = \frac{1}{2}\left[(1 - \alpha^2)\left(\frac{1 - v_t^{1/2}}{v_t^{1/2}}\right)\left(\frac{E_f}{G_b}\right)\right]^{1/2} \cosh^{-1}\left[\frac{1 + (1 - \varphi)^2}{2(1 - \phi)}\right] \qquad (30)$$

For 90% as the limit of effectiveness, fig. 6 shows the fiber ineffective length as a function of the gross fiber volume fraction. It can be seen that the ineffective length is substantially less than that of the solid fiber.

The maximum shear stresses associated with this configuration are shown in fig. 7. Curves labelled 1 and 2 compare the stresses for hollow and solid fibers in the same configuration when the same stress level exists in the glass. Again it can be seen that the hollow fibers have a substantially lower shear stress on their interface. For comparison, two alternate changes in material characteristics are also shown. The effect of a high modulus

glass fiber is to lower the interface stresses but only by about half the change produced by hollow fibers. An increase in binder modulus has a significant and unfavorable effect upon the shear stresses. All shear stresses shown have been normalized with respect to the axial fiber stress. Thus, for fibers which fail at 200 ksi, shear stresses would be in the range of 18-30 ksi for glass fibers with a gross volume fraction of 0.7. These stresses are beyond the elastic limit for most epoxies ans it is necessary to consider the effect of an inelastic binder material.

As a first approximation to the inelastic problem, the binder was considered to have an elastic-plastic stress strain curve. This combination of linear elasticity to a given yield stress and then constant stress for all larger strains is a gross idealization of an actual epoxy stress-strain curve but it does enable an estimate of the nature of inelastic effects. The resulting effects on the interface shear stresses are shown in fig. 8 for a binder shear yield stress equal to 5% of the extensional stress in the fiber. Note that maximum shear stresses are of course lower, while ineffective fiber lengths have increased. The stress decrease is beneficial but the ineffective length increase can result in a reduced composite tensile strength. The magnitude of the ineffective length change is shown in fig. 9 for a solid glass fiber and epoxy composite with a binder volume fraction of 0.3. For high binder yield stress values the elastic result is obtained. At lower yield values the curve rises sharply and may produce a substantial decrease in composite strength.

II. EXPERIMENTAL STUDIES

The experimental studies fall in the general categories of mechanical thermal and electrical property measurements. These areas are described following the definition of the constituents used.

A. Constituents

Glass fiber development and procurement: All glass fibers, hollow and solid, used in this program were supplied by Pittsburgh Plate Glass Co. (PPG). Physical properties of the fibers are detailed in Table 1. At the start of the program, PPG offered on a production basis, fibers with hollowness ratios, α, of 0 and 0.6. Because interest lies in an assessment of the influence on composite performance of changes in hollowness ratio, PPG agreed to attempt the manufacture of fibers with a hollowness ratio of 0.75. After several months of development effort, it was found that manufacturing difficulties made it impossible to supply quantities of these fibers. The test phase of the program was then reoriented to obtain and test composites of only two fiber configurations, $\alpha = 0.0$ (solid) and 0.6 (hollow).

The initial rovings of hollow glass fibers received for use in the isotensoid bottle program showed signs of fiber breakage on the reel ends. However, in order to prevent delay of the program, these fibers were used to wind the first five isotensoid bottles to evaluate the workability of the resin system chosen and to check fiber finish compatibility with the resin system.

Problems associated with the fiber fabriciation apparently indicate the data obtained in this program are not yet representative of a production material. The analytically indicated potential as well as the experimental results must be considered in assessing possible future applications of this material.

Resin system: Two resin systems described as systems 1 and 2 in Table 2 were originally designed for use during this program. They were the results of attempts to design a resin system that would optimize the most desirable resin-glass composite properties. The composite properties of most interest were, in order, strength at both room and elevated temperatures, dielectric constant, thermal conductivity, shear strength, susceptibility to water intrusion, heat of ablation and acoustic response. Formulation No. 2 was chosen over No. 1 because of its longer pot life at the recommended winding temperature of 150^{o}F.

Problems of maintaining this temperature during winding of isotensoid bottles were encountered. Additional developmental work was then done on winding tension, resin uniformity during winding, and cure cycle modifications. Fabrication of the first lot of isotensoid bottles (Nos. 1 to 5) revealed serious brittleness problems with the resin system, and it was decided to abandon the attempt to idealize the resin system in so short a time and to redefine the resin design criteria.

An easy to use, well-known (by the filament winding industry) and uncomplicated resin system possessing good overall properties with no further development required became the goal. The system selected is listed as No. 3 in Table 2. Room temperature tensile properties of this resin system are listed in Table 2 and fig. 10. As shown by these data, this sytem is a high grade reinforced plastic production system, not an R&D system. The system can by used at room temperature and is completely compatible with the standard binder applied by PPG to their fibers. All test plates fabricated by 3M Corporation and all isotensoid bottles wound by GE used this system.

Lamtex Industries, however, used another, similar, formulation in fabricating all hydrostatic pressure shells and axial compression shells. This is listed in Table 2 as System No. 4.

The finish and sizing system supplied by the glass vendor on all filaments is a proprietary system compatible with epoxy base resin systems.

Since it is in use by other manufacturers (Brunswick Corp., Hercules Powder Co.) to produce satisfactory test and aircraft flight hardware, it was not deemed necessary to perform compatibility tests under this program.

B. Test Specimens

The specimen manufacture and procurement to be discussed in this section is limited to the plates fabricated by the 3M Corporation and the shells supplied by Lamtex Industries. Test specimens for the ablation, electrical, thermal and fatigue tests were all fabricated from the 3M plates and the individual specimens will be discussed in their respective sections. The isotensoid bottle manufacture is discussed separately in section E-1.

The 3M Co. of St. Paul, Minnesota, was selected to fabricate flat plate specimens with the following fiber geometries:

β \ α	0.0	0.6	Total
0	1	2	3
$\pm 45^{o}$	1	2	3
$\pm 60^{o}$	1	2	3
			9

where α is the ratio of fiber inner to outer diameter and β is the angle between the fibers and the plate centerline.

Fig. 11 shows a pair of plates manufactured by 3M Company for this program. The difference in appearance between solid and hollow fibers is immediately recognizable.

Table 3 summarizes density and glass and resin contents by weight for each plate configuration.

Lamtex Industries, Inc. was selected to fabricate the cylindrical shells to be used in the hydrostatic pressure and axial load portions of this program. The following shell sizes were selected:

ID	= 15 in	ID	= 8 in
L	= 15 in	L	= 16 in
t	= .05 in	t	= .05 in

Twelve shells of each size were specified as follows:

β \ α	0	.6
30°	2	2
90°	2	2
60°Isotropic	2	2

where β = helix angle, with respect to the longitudinal axis of the shell. The 60° isotropic shells had 1/3 the total number of fibers wound in the circumferential direction. The first 1/6 of the fibers were circumferential the following 2/3 were at a helix angle of $\pm 30°$ and the remaining 1/6 were circumferential.

Also four thick shells with the following geometries were made:

ID	=	8.0 in	ID	=	8.0 in
L	=	16.0 in	L	=	16.0 in
t	=	.50 in	t	=	0.50 in
α	=	0	α	=	0.6
β	=	90°	β	=	90°

These shells were designed to explore the nature of hollow fiber behavior where compressive strength, rather than elastic stability is the major contributor to shell failure.

Figs. 12, 13, and 14 show the shell dimensions as developed by GE and Lamtex. These dimsneions and tolerances reflect state of the art requirements.

Because of fiber supply problems the initial shell deliveries were delayed. Because of poor quality (rough surfaces, broken fibers on surfaces, gaps in windings and very high resin content) some of the shells were rejected and the delivery schedule was delayed further.

Lengthy discussions with Lamtex technical and management personnel uncovered several areas where additional manufacturing development work should be done to efficiently wind hollow fibers into structural shapes. Included among these are breakage of filaments during the winding process. The broken fibers tended to gather at restricted points in their travels from reel to mandrel and cause very uneven supply to the traveling guides. Also the hollow fibers did not lay down in a uniform band on the mandrel; instead, the rovings coming

from the bank reels (Lamtex used nine reels of fibers at one time to wrap shells with helix angles other than 90°, and up to six reels for circumferential windings) tended to gather together in a rope-like shape. The resultant variation in the width of the roving caused overlaps or gaps in the glass layers. The resultant non-uniformity of physical properties must be taken into account when comparing experimental and analytical results.

C. Electrical Properties

Measurements of the dielectric properties of hollow glass fiber reinforced plastics were conducted at the GE Re-entry Systems Department Materials Performance Laboratory using well-known wave-guide impedance techniques. Measurements were conducted in the L, C, and X bands on the materials in question using a coaxial transmission line for the L band and rectangular wave-guides for the C and X bands. The slotted line technique was employed in all cases. Complete discussions of the theory and use of these techniques are found in refs. 6 and 7. A brief theoretical background development follows.

Background: The electromagnetic behavior of materials is usually characterized by specifying the following quantities: dielectric constant (permittivity), dielectric loss tangent, permeability, and magnetic loss tangent. The former two quantities yield information about the material's electric behavior, while the latter two yield information about the material's magnetic behavior in an electromagnetic field. Since the materials of interest here are non-magnetic, the permeability μ is taken to be that of free space; i.e., $\mu = \mu_o$, the magnetic loss tangent is taken to be zero,

since there are no magnetic effects to produce losses. The dielectric properties are therefore of prime interest here, and the magnetic properties will not be treated.

The quantity which sums up all the dielectric information is called the complex dielectric constant or, more correctly, the complex permittivity, since in general the quantity does not remain constant over a wide frequency range. The expression for the complex dielectric constant is derived very simply from Maxwell's equations as follows:

Beginning with the following relationship from Maxwell:

$$\nabla \times \overline{H} = \dot{\overline{D}} + \overline{i} \tag{31}$$

where $\overline{H}$, $\overline{D}$, and $\overline{i}$ represent the magnetic field intensity, the electric displacement density, and the current density, respectively. Since

$$\overline{D} = \epsilon' \overline{E}$$

and

$$\overline{i} = \sigma \overline{E}$$

eq. (31) becomes:

$$\nabla \times \overline{H} = \epsilon' \dot{\overline{E}} + \sigma \overline{E} \tag{32}$$

where $\overline{E}$ is the electric field intensity and σ is the material conductivity. $\overline{H}$ and $\overline{E}$ are assumed sinusoidal with respect to time; i.e.,

$$\overline{H} = \overline{H}_o e^{j\omega t}$$

$$\overline{E} = \overline{E}_o e^{j\omega t}$$

Since

$$\dot{\overline{E}} = \frac{\partial \overline{E}}{\partial t} = j\omega \overline{E}_o e^{j\omega t} = j\omega \overline{E},$$

eq. (32) becomes:

$$\nabla \times \overline{H} = (\epsilon' j\omega + \sigma)\overline{E} \tag{33}$$

Factoring out $j\omega$:

$$\nabla \times \overline{H} = j\omega(\epsilon' - j\frac{\sigma}{\omega})\overline{E} \tag{34}$$

Eq. (34) must be of the form

$$\nabla \times \overline{H} = j\omega \text{ (dielectric constant) } \overline{E}$$

so we define

$$\epsilon^* = \epsilon' - j\frac{\sigma}{\omega} \tag{35}$$

as the complex dielectric constant and obtain

$$\nabla \times \overline{H} = j\omega \epsilon^* \overline{E}. \tag{36}$$

By allowing

$$\epsilon'' = \frac{\sigma}{\omega} \tag{37}$$

the expression for the complex dielectric constant becomes

$$\epsilon^* = \epsilon' - j\epsilon'' \tag{38}$$

The real part ϵ' is called the dielectric constant while the imaginary part ϵ'' is called the loss factor. In terms of relative values

$$\epsilon^* = K'\epsilon_o - jK''\epsilon_o = (K' - jK'')\epsilon_o = K^*\epsilon_o$$

where K^* is the complex relative dielectric constant, K' is the relative dielectric constant, K'' is the relative loss factor, and ϵ_o is the free space permittivity.

$$K^* = K' - jK'' \tag{39}$$

The quantities presented in the remainder of this report will be the relative quantities. If the absolute quantities are desired, they may be obtained by multiplying the relative values by ϵ_o. Note that the conductivity of a material may be obtained by using eq. (37)

$$\sigma = \omega\epsilon'' = \omega K''\epsilon_o$$

where, unless ϵ'' is truly constant, ω is the angular frequency at which the measured value ϵ'' is obtained.

The dielectric loss tangent is defined as

$$\tan\delta = \frac{\epsilon''}{\epsilon'} = \frac{K''}{K'}$$

A value of tan $\delta \gg 1$ indicates a good conductor while a value of tan $\delta \ll 1$ indicates a good dielectric material.

Physically, the dielectric constant or relative dielectric constant gives a measure of the reflection and transmission of incident electromagnetic energy by the material, while the loss tangent gives an indication of the material's ability to absorb or dissipate energy.

Table 4 summarizes test conditions and test results for the three frequencies investigated. Fig. 15 illustrates the specimen configurations and figs. 16 and 17 show the test apparatus setups. Table 5 gives an equipment list for the experimental measurements.

Results: Since the specimens tested are mixtures of glass and epoxy resin the relative dielectric constant would be expected to lie between the constants for these component materials which is indeed the case, a typical K' value for glass being 5 or 6 and for epoxy being about 3.

The effect of fiber orientation on test results appears negligible. The reason is that the glass fibers are too close together to be resolved by the electromagnetic waves at the frequencies used. Since this degree of resolution is inversely proportional to the wave length of the electromagnetic radiation being used, optical frequencies would be necessary to cause fiber orientation effects to appear.

The relative dielectric constant (K') remains essentially constant for a given fiber over the frequency range tested. This effect is due to the material being non-polar, thus exhibiting no orientational or ionic polarization effects

which would cause noticeable changes in K'. The relative dielectric constant of the solid fiber materials are higher than those of the hollow fiber materials. This is to be expected because the air in the hollow fibers contributes toward lowering the overall dielectric constant. The extra measurements in the C & X bands on the hollow fiber longitudinal samples were made to determine the effect of bonding together several laminates of material in two different orientations. In one case the bond lines were horizontal, while in the other the bond lines were oriented vertically and ran parallel to the direction of propagation. This variation had no effect whatsoever on the results.

In general, the loss tangents for each specimen configuration decreased with increasing frequency. Such a trend agrees with the behavior of a pure epoxy which exhibits a loss tangent peak of 0.028 at L band and decreases with increasing frequency. Glass typically has a very low loss tangent at the frequencies tested so that tangent behavior may be attributed to the epoxy. Values of the loss tangent exhibited by the materials indicate it is a high loss material compared to polyethylene or teflon which exhibit loss tangents on the order of .0002.

Figs. 18 and 19 show the variation in dielectric constant and loss tangent with frequency for all the specimens tested. Figs. 16 and 17 show that both of these electrical properties are lower for hollow than for solid fiber reinforced plastics. The average decrease for K' is approximately 30 percent. The decrease in loss tangent varies from 12 to 45 percent in the L-band and is quite small for the C and X band values.

On the whole, transmission losses (in db per equal thickness) are approximately 15 percent less for hollow than for solid fiber reinforced plastics. For most structural applications hollow fiber material will be somewhat thicker than solid fiber material. Therefore, no significant advantage in electrical transmissibility properties appears to accrue for solid vs. hollow fiber reinforced epoxies under structural applications. Low dielectric resins (like Buton A-500) should be used if electric transmissibility is a primary requirement.

D. Thermal Properties

Determination of the temperature dependent thermal conductivity, specific heat and thermal expansion coefficients of the fiber reinforced plastics and resin system, was made by General Electric's Re-entry Systems Department. Ablation tests were performed by the Space Sciences Laboratory. The experimental equipment, techniques and results will be discussed separately for each property.

1. Conductivity

A Dynatech TC-1000 comparator, shown in fig. 20 with the bell jar removed, was used to evaluate the thermal conductivity coefficients of the various configurations. The principle of operation is based upon comparing the unknown specimens' ability to conduct heat with that of heat meters of known thermal conductivity. The apparatus consists of a power supply for supplying heater power, a water cooled heat sink, and a test stack assembly

which consists of two identical heat meters between which the specimen is sandwiched. Armco iron, Inconel 702 and fused silica heat meters are used depending upon the thermal conductivity of the unknown specimen. The range of test temperatures is -300°F to +700°F. The test stack is housed in a bell jar capable of achieving a vacuum of 10^{-6} mm of Hg. The test specimen size was 2 1/2" x 2 1/2" x 1/4". All specimens were cut from the plates described in Section 2.

The test is performed on a specimen of unknown thermal conductivity sandwiched between two identical heat meters of known thermal conductivity. The specimen and heat meters are, in turn, held between a heater and a fluid-cooled heat sink. Thus, the test section consists of a stack containing a heater heat meter, specimen, a second heat meter, and finally a heat sink at the bottom. A typical test stack is shown in fig. 21. During the test, the heat flows from the heater assembly through the stack to the heat sink. Surface temperatures are measured on each heat meter and specimen.

The temperature dependent thermal conductivity coefficients of the specimen are determined by substituting recorded temperatures and gradients, heat meter thermal conductivity coefficients, and specimen and heat meter thicknesses into the following relationship:

$$K_s = K_m \left(\frac{\Delta \overline{T}_m}{\Delta T_s}\right) \left(\frac{\Delta X_s}{\Delta X_m}\right)$$

where K_s is specimen thermal conductivity, K_m is heat meter thermal conductivity, ΔX_s and ΔX_m are specimen and heat meter thicknesses

respectively, $\Delta \overline{T}_m$ is the average temperature drop across the heat meters, and ΔT_s is the specimen temperature drop.

The test results are presented in figs. 25, 26, and 27 which show, respectively, the thermal conductivity variation with temperature for the hollow fiber, solid fiber and epoxy resin samples tested. For the fiber specimens, the same trend can be detected for both hollow and solid fibers: the specimens with fibers running in the direction of heat flow have the highest coefficient, the unidirectional transversely oriented fibers show the lowest conductivity, and the bidirectional transverse specimens fall between these extremes. (Refer to fig. 33 for fiber orientations and nomenclature.) The values for the resin conductivity coefficient in fig. 27 and the literature value for thermal conductivity of glass were used in the equations of Part I to predict composite thermal conductivity. The results are plotted as solid points on figs. 25 and 26. The analytical points are consistently higher than experimental values. This could be attributed to the neglect of thermal resistance at the interfaces.

Comparison values of thermal conductivity for glass-reinforced phenolic resin and phenolic refrasil, an ablative material, are shown in fig. 28 with test values for solid and hollow transverse unidirectional specimens. The samples are ranked generally according to density. Hollow glass structures show up well on this basis although a much more thorough investigation would be necessary to establish complete relative value.

2. Specific Heat

A Dynatech SH-100 Continuous Specific Heat apparatus, as shown in fig. 22, was used to determine the specific heat coefficients of the various configurations. In principle, an accurately measured quantity of heat is supplied to the test specimen and the functional relationships between the temperature response of the specimen and the quantity of added heat obtained. This data together with the mass of the specimen is sufficient to determine the specific heat of the material. The range of test temperatures available is -300°F to +700°F. The test specimens' size was 2 1/2" x 2 1/2" x 1/4" and their fiber orientations were as shown in fig. 33. All specimens were cut from the plates discussed in Section 2.

The specimen is sandwiched between two identical heater assemblies. These heaters serve to supply the heat which is added to the test sample. A thermocouple is connected to each of the main heaters, one to monitor the sample and heater assembly temperature, and the other serving as a reference temperature signal for the guard heater. The specimen and main heater assembly, shown in fig. 23, is suspended in a triple walled chamber, the innermost being an electrically heated guard whose temperature is automatically maintained equal to the main heater assembly. The outer chamber serves as a vacuum chamber for minimizing convection losses. The specimen heating rate is determined by the voltage setting of the main heater power supply.

The continuous temperature-time response of the heater and heater specimen assemblies are reduced to an accumulated heat curve as a function

of specimen temperature. The temperature-dependent specific heat coefficients are then derived from the accumulated heat (or enthalpy) data according to the definition

$$C_p = \left(\frac{dH}{dT}\right) P$$

where C_p is the specific heat, H is the accumulated heat (or enthalpy), and T is temperature, P is the constant pressure.

The test results are presented in figs. 29, 30, and 31 which show, respectively, the thermal specific heat variation with temperature for the hollow fiber, solid fiber and epoxy resin samples tested. The coefficients are greatly dissimilar for the fiber reinforced samples although the hollow specimens do run a bit higher with the hollow longitudinal specimen being highest. It should be noted however, that the longitudinal specimens are made by cutting 1/4" wide strips and bonding them together so that the fibers run normal to the 2 1/2" x 2 1/2" face of the specimen rather than parallel to it. Additional thermal energy may have been absorbed by the bonding resin used in fabricating these specimens. The specific heat of the Epon resin is higher than for any of the glass-epoxy composites.

Comparisons are made in fig. 32 between the specific heats of hollow transverse unidirectional and solid transverse bidirectional fiber specimens with glass-reinforced phenolic resin and phenolic refrasil. Here hollow glass structures have the lowest specific heat. The samples are ranked generally according to resin content.

3. Expansion

A specially developed machine made by Materials Technology Incorporated shown in fig. 24 was used to determine the thermal expansion coefficients of the various configurations. The unique principle of operation of the device is its ability to provide a continually changing temperature in the specimen compared with the earlier methods of evaluating thermal expansion coefficients at discrete temperatures. The specimen is connected to a Linear Variable-Differential Transducer (LVDT) which provides a record of the change in specimen size with temperature change. The data is recorded on the Mosley-Offner combination also shown in fig. 24.

The test was performed simultaneously on all specimens with the same fiber orientation. Length measurements were made of all samples before and after testing to evaluate dimensional stability. After soaking at -250°F for one-half hour, the specimens were heated to +400°F at a rate of 1°F per minute. The specimen sizes were 2.00" x 3/4" x 1/4". Change of length was measured along the 2" length in all cases. Fig. 34 shows the test specimen configurations.

The test results are shown in figs. 35 through 40 as traces of $\Delta L/L$ vs Temperature variation. In all cases, the thermal growth of the hollow fiber specimens is greater than for the solid fiber specimens. The growth for both hollow fiber and solid fiber specimen series appears to be related to fiber angle. This demonstrates the increasing effect of the resin's greater rate of thermal expansion on the composite thermal expansion as the quantity of glass in the direction of measurement goes from maximum for the longitudinal

to minimum for the transverse specimens. Fig. 41 shows the thermal expansion variation with temperature for the epon resin used in making the specimens. Its greater expansion coefficient is readily apparent.

The shrinkage recorded in the first runs on figs. 36 and 37 and for the solid fiber 60° combination specimen indicates a curing process in the specimens' resin occurring above approximately 200°F. The second runs shown in figs. 36 and 37 indicate the thermal expansion values of the fully cured specimens. The hollow and solid transverse specimens showed permanent changes of length of .010" after the first runs but showed no change after the second runs, again showing incomplete cure before testing and completed cure after run #1. The solid fiber specimen in fig. 40 showed a change in length of .005" after the first run.

The equations of Part I for thermal expansion coefficient were used to compare analytical to experimental results. The expansion in the range 0-160°F was considered. The epoxy coefficient was taken from fig. 41 and the glass value was taken from the literature (ref. 15). The results are presented in the following table.

Average Thermal Expansion Coefficients for Glass Fiber Composites in the Range 0° - +160°F

Type of fiber	Direction	Analytical	Experimental
Solid	Longitudinal	$3.90 \times 10^{-6}/°F$	$3.75 \times 10^{-6}/°F$
Solid	Transverse	$17.1 \times 10^{-6}/°F$	$14.1 \times 10^{-6}/°F$
Hollow	Longitudinal	$4.81 \times 10^{-6}/°F$	$10.9 \times 10^{-6}/°F$
Hollow	Transverse	$19.1 \times 10^{-6}/°F$	$28.8 \times 10^{-6}/°F$

The agreement for solid fibers is considered good. The lack of correlation for the hollow fibers may be associated with the uncertainties of hollow fiber geometries.

4. Thermogravimetry

The results of a thermo-gravimetric analysis run on a hollow fiber unidirectional specimen are presented in fig. 42. This figure can be used in conjunction with the thermal conductivity and thermal specific heat plots to show the correlation between degradation of these coefficients and the loss of material from the specimen. In addition, such data are used in evaluating candidate materials for ablative applications. Here, the products given off at temperature and the temperature at which losses begin are of importance to re-entry body designers.

5. Ablation

Evaluation of materials for ablation characteristics is conducted by the General Electric Space Sciences Laboratory in a Shroud Nozzle Air Arc. (Figs. 43 and 44) This facility is equipped with a vortex stabilized, axial flow electric arc unit which is employed to heat air (or another gas) prior to its passage through a nozzle which is restricted by the test specimen. The inlet gas flow is metered and regulated, the stagnation pressure then being controlled by maintaining the proper annualr clearance between the test specimen and the nozzle wall, even as the specimen surface recedes. Controls permit rapid insertion of the specimen into test position after the hot flow has stabilized

and withdrawal after a pre-established test period.

In this program, the specimens tested were .670 inch diameter cylinders with spherical nose radii of .50 inches. Each specimen was built up of carefully oriented .25 inch thick blocks cemented together with the same Epon 828 resin system used in fabricating the sheets from which the blocks were cut. The specimens were then cemented to phenolic nylon strings and the entire assembly machined to the dimensions noted above. (See fig. 45.)

Operating conditions for each test are summarized in Table 6 together with the heat transfer rate measurements associated with the program. The specimens were tested in the Shroud Nozzle Air Arc to provide an environment of moderate enthalpy (6700 Btu/lb) and of high rates of heat transfer (1850 Btu/sec-ft^2 to a cold wall). These values are representative of current ballistic re-entry conditions.

The compuation of the heats of ablation (q^*) can be treated by either of two methods: for a net change in weight of the specimen

$$q^* = \frac{\dot{q}_c A t}{\Delta m}$$

and for a net change in length

$$q^* = \frac{\dot{q}_c t}{\rho \Delta L}$$

q^*	=	heat of ablation
$\dot{q}$	=	corrected rate of heat transfer
A	=	cross sectional area of specimen
m	=	net weight change of specimen during test
t	=	time
ρ	=	density of material under test
ΔL	=	net change of length of specimen during test.

Assuming that no material is removed below the surface to which the specimen has ablated, the two methods should yield identical results, because they are alternate forms of the same expression. However, it is not unusual for the severe heating to drive out material below the apparent surface to which ablation has progressed (e.g. a resin binder material). In such a circumstance, q^* based on mass loss will frequently appear to be lower in value.

The corrected heat transfer rate, $\dot{q}_c$, was evaluated at 1380 Btu/sec-ft^2. Corrections applied were for anthalopy of gas adjacent to the specimen wall and for re-radiation. Enthalpy difference is the driving potential delivering heat to the surface under test. As the surface temperature rises, this difference is decreased. It is accepted practice to take the enthalpy of gas at the wall to be tha corresponding to the surface temperature of the model since no discontinuity may exist at the wall-gas interface. Surface temperatures were measured with a two color pyrometer calibrated to graphite with which the test facility is equipped. Since the surface of the specimens tended to develop a char, the reported surface color temperatures (fig. 45 through 48) are probably quite close to the true values.

The correction for re-radiation was based on a surface emissivity of 0.86, corresponding to that of graphite. Since the surface did indeed develop a char, the assumed emissivity is believed reasonable. The application of these two corrections reduces the cold wall heat transfer rate of 1850 Btu/sec-ft^2 to an effective value of 1380 Btu/sec-ft^2 on the hot surface of the specimen.

Examination of the exposed specimens showed that unidirectionally oriented fibers, aligned perpendicularly to the flow, were removed unevenly. The short fibers most remote from the diametral fibers formed when the cylindrical model was machined, suffered greater ablation than those on or near the diameter. Thus, ablation was generally not symmetrical (figs. 49 through 52). Fibers at the immediate ablation surface were no longer an integral part of the solid; surface fibers could be removed by a very light scraping action. This suggests that the organic binder material was driven from the specimen even below the macroscopic ablation surface. Note that in every case the mass loss q^* values were less than the length change q^*, tending to confirm the above conclusion. Length change measurements reported represent the considered average of the model length after test, subtracted from the original length.

Conclusions: While the differences measured are small, it appears that the hollow fiber specimens showed greater resistance to ablation than did the solid fiber specimens. No distinct difference in performance was observed due to fiber orientation for solid or hollow fiber specimens. None of the specimnes exhibited heats of ablation (q^*) to compare with phenolic nylon ($q^* > 6000$ Btu/lb) a common ablation shield material which, however, has lower mechanical strength than the materials tested herein.

E. Mechanical Properties

The mechanical tests performed during this phase of the program were primarily on typical structural elements. Thus, internal pressure tests of isotensoid bottles, external pressure tests of cylindrical shells and axial compression tests of cylindrical shells were performed on filament wound solid and hollow glass fiber reinforced plastic specimens. Also, an exploratory investigation of the fatigue problems associated with the pratical application of the hollow fibers was undertaken. These various tests are described individually below.

1. Internal Pressure

Prior to the present program, no hollow glass fiber reinforced composites had been made and tested for mechanical strength other than the hand lay-up straight rods made by the General Electric Company for the Bureau of Naval Weapons under Contract no. NOw 61-0613-d, see ref. 1. In order to obtain data on the tensile strength of the hollow fibers in a composite as early as possible in the present program it was decided to wind "Outwater" isotensoid bottles and test them prior to the fabrication of other (cylindrical and plate) specimens. Information gained from these bottles could then be used advantageously in selecting resin systems, winding patterns, and other manufacturing and test parameters for the remainder of the program.

The Vermont Instrument Company isotensoid bottle winder used by the Manufacturing Engineering Research and Development Laboratory of the GE

Missile and Space Division in making these specimens is shown in fig. 54. This polar type filament winding machine lays the windings on a cast mandrel in such a pattern that the fibers are under constant and equal tension when an internal hydrostatic pressure is applied to the finished, cured bottle. The mandrel is cast from a molten salt compound (Rezolin 35) which is dissolved after resin curing. Fig. 54 also shows a mandrel mold, a partially wound bottle and a finished, cured bottle ready for testing.

The first five isotensoid bottles fabricated were used to evaluate the resin system originally selected to be used during this program. This system is noted as No. 2 in Table 2. The fibers used came from a damaged hollow fiber roving received early in the program which was not considered satisfactory for material property evaluation. (See Section 1.) The bottles fabricated from this roving were used to determine compatibility between fiber sizing and resin system, and the adequacy of the cure cycle.

Several dry test windings were made before the first bottle was fabricated to determine the proper lead settings which would eliminate all winding gaps and overlaps. The number of turns which just covered the mandrel with the hollow fiber roving was 225. The bottles were actually wound with 20 extra turns to cover the point of startup and prevent failures due to start-up irregularities. Two complete plies were wound on each bottle.

After the bottles were wound they were removed from the winding machine and cured 2 hr @ 200°F and 16 hr @ 300°F while rotating in a rotisserie after which they were cooled to room temperature at the rate of 50°F/hr.

They were then stored vertically for mandrel removal. Four of the first five specimens developed circumferential surface cracks to varying degrees while stored. The mandrels were removed by immersing the bottles in warm water for six hours, drying at 225°, and slow cooling to room temperature. Mandrel removal aggravated the surface cracks. Complete geometrical characteristics of the fibers and bottles are listed in Table 7.

The bottles were prepared for internal hydrostatic pressure testing by inserting rubber bladders with special high pressure seals and mounting within an armored chamber. Pressure was supplied by an Instron test machine cross-head which actuated a piston in a cylinder connected to the bottle. Burst pressure was read from a Heise maximum reading gage and also recorded on the Instron recorder. The detailed bottle fabrication and test techniques are presented in refs. 8 and 9. Results of the first five bottle tests made with the No. 2 resin system (See Section3) are listed in Table 8. Fig. 55 shows a typical bottle and the mode of failure.

After a change in resin system as discussed in Section 3, and receipt of additional hollow fiber rovings, thirteen more specimens were wound (Nos. 6 through 18). Again, dry test windings were made to determine the number of windings required to cover the mandrel without laps or gaps. The number determined was 252 turns. Actual winding was done with 272 turns. All other data in Table 7 are also applicable to these specimens. The mandrel removal rechnique was modified in order to eliminate the drying cycle needed when the bottles were immersed in water. The mandrels were removed with warm water

hosed directly into the interior of the bottle, and the drying cycle was combined with the postcure cycle. Details of the curing and drying procedure are given in Notes 1 through 3 of Table 9. This table also lists all test results for these specimens.

Specimens 6 and 7 were used to study methods of removing excess resin while winding. The fibers were so fragile, however, that severe breakage resulted and the specimens had to be scrapped. No further attempts were made to wipe off excess resin. All excess resin is removed by the careful application of blotting paper to the outside of the bottles. This avoids fiber damage.

For comparison purposes, five bottles were fabricated and tested using a solid fiber roving. Complete geometrical characteristics of the fiber and bottles are listed in Table 10. Test results are listed in Table 11.

Results: Individual fiber stresses attained in the isotensoid test program are lower than expected. Some reasons for the low values can be advanced but further development work would be necessary to satisfactorily isolate the exact causes.

A likely cause for poor test results from the bottles is the frayed condition of the rovings when received from PPG. The failures noted were all of the localized kind shown in fig. 55, which strengthens the belief that damaged fibers controlled the burst pressures of the bottles.

A problem that developed during the hollow fiber work was the handling of the reels without causing breakage of the fibers. The cardboard cores of the reels should be made longer so that handling can be done using these rather than holding the bulk itself. Fuzziness, denoting broken fibers, was noted on the rovings during all the bottle winding operations, and the surfaces of all bottles showed broken filament ends.

Another characteristic of the rovings used in this phase of the program should be investigated further for its effect on the strength of filament-wound pressure vessels; namely, all rovings used exhibited a twisting movement as they passed from reel to winding machine and over the guide rollers of the machine. This twisting prevented the rovings from lying flat against the mandrel and caused gaps to occur in the winding pattern. These gaps were closed only by resin which had a much lower strength than the glass. Thus, weak spots were built into the bottle windings. A brief investigation of this twisting action disclosed that it is a consequence of the fabrication and reeling operations and could not be removed without expensive modification of this fabricator's equipment.

2. Hydrostatic Pressure

Hydrostatic compression tests of filament wound shells were conducted by General Electric's Re-entry Systems Department. All shells were procured from Lamtex Industries as discussed in Section 2. The geometrical properties of the shells and their serial numbers are listed in Table 12.

Test conditions for the shells specified, among other things, that no end loads were to be applied to the shells. The arrangement shown in fig. 56 was developed to allow proper sealing of the ends of the shells as well as to allow the end loads to be reacted by something other than the shells under test.

The tests were conducted using a converted Naval projectile as the pressure chamber. Mounted, with the pump system, on a ground service cart, it proved a reliable, inexpensively developed pressure test facility. A schematic of the pressurization system is presented as fig. 57.

The sealing systems for the test shells to prevent water intrusion through the shell walls, or between shell walls and end plates, were the first problems encountered in the actual test program. After evaluating several schemes, the system shown in figs. 57 and 59 was adopted for the high pressure testing of the thick-walled shells. For the thin wall shells, the system is identical except that only Johns Manville Duxseal is used to seal the end plates. The much lower pressure made no better system necessary.

The first twelve shells tested were instrumented as follows: two triaxial strain gauges back-to-back on the shell wall to elimimate bending effects with each gauge read as one leg of a bridge circuit, four uniaxial gauges mounted in back-to-back pairs circumferentially on the shell read in series as a single channel. The final four shells carried only the two circumferentially mounted gauges read as single series-connected output.

Recording equipment consisted of two Consolidated Electrodynamics Corporation model 1-127 carrier amplifiers feeding a CEC model 5-124 oscillograph. Balancing of the circuits before test was accomplished to within 5% of null and the overall accuracy of the strain recordings is believed to be well within $\pm$ 10%.

Figs. 60 through 65 present plots of circumferential compression stress in the shells against circumferential strains. From these figures, values of E_c for each shell are calculated and listed on the figure. In figs. 64 and 65, curves for both pairs of circumferential strain gages on each shell are shown since their values differed substantially, affecting the E calculations.

It is difficult to compare hollow fiber performance with that of the solid fibers because of the wide variations in test article quality. It is not felt that the structural capabilities of the respective fiber configuration were fairly demonstrated.

Poisson's ratios as calculated from test data reflect the variation in the experimentally determined values of E. For the thin wall shells tested, the ratio ranged from .127 for shell no. 3 to .156 for shell no. 12. The thick wall shells, as expected, showed a much higher set of values, ranging from .25 to .33.

3. Axial Compression

Cylindrical shells subjected to axial compression have been indicated as a suitable application for fibrous composites. A comparison between the performance of hollow and solid glass fibers for this application was performed using shells of the configuration shown in figure 14. The winding patterns were selected on the basis of analytical studies performed in ref. 11. These studies indicated that "isotropic" windings were of higher efficiency (lower weight) than any two-directional symmetric helical winding pattern and also better than any combination of longitudinal and circumferential windings. Of the helical patterns an angle with the longitudinal axis of just under 30° was optimum. For these reasons the 60° isotropic and the 30° helical patterns were selected. To study a case where transverse shear stresses would be of importance, a circumferential winding pattern was also selected. The shells were instrumented with Budd foil strain gages and tested in axial compression in a Tinius Olsen 120 kip testing machine. All tests were performed at a crosshead velocity of 0.02 inches per minute.

A load-deflection curve for each type of cylinder is presented in fig. 66. It is seen that the curve is essentially linear up to the point of buckling. The failure modes are shown in the photographs of fig. 67. After failure sections of the cylinders were used to determine the volume fractions of the constituents. These data are included in the description of cylinders presented in Table 14 along with the failure loads.

The failure loads were compared to those obtained analytically by the methods of ref. 12. Difficulty in the direct application of these methods is introduced by the relatively large volume of included air in the matrix material (see Table 14). In order to account for this, the following method was utilized: first, the eqs. of ref. 13 for bulk and shear moduli were applied to the matrix material with voids which are assumed to be spherical. For the shear modulus, the equation presented in that reference which lies between the bounds derived therein was used. From these expressions a reduced Young's modulus and the associated Poisson's ratio were obtained and these were used as the elastic constants of a matrix having a volume fraction equal to $v_b + v_a - v_o$ as given in Table 14. From this and the glass properties elastic constants for uniaxially oriented fibers were obtained. These were used in a laminate analysis and a cylinder buckling analysis based on ref. 14 as described in ref. 12. The results of these computations are plotted in fig. 68 in the form of analytical buckling load against maximum experimental load. This perfect agreement is somewhat surprising and will be discussed further below.

A further comparison of analysis with experiment is obtained with the results for axial stiffness of the cylinders. The axial stiffness was measured by longitudinal strain gages and by overall head displacement. The outputs of back-to-back strain gages were averaged to obtain the strain value. In some cases the spread between the two gage values was significant; as much as 50% of the average value. Yet the three average values obtained from

three pairs of gages on a cylinder were generally close to each other. Typical results are plotted in fig. 69 in the form of stress-strain curves. The results for axial stiffness, expressed as the effective longitudinal Young's modulus of the laminate are presented in Table 15. Also shown are the analytical values obtained as described previously.

The analytical and experimental results of Table 15 are not in good agreement. There are factors which make both sets of results suspect. Thus, the corrections of binder moduli for the included air may have been too extreme, resulting in low analytical values. On the other hand, the strain measuring devices may have recorded strain values which are too low; as strain gages may well do. The agreement of the analytical buckling loads with experimental results can be taken as supporting the analytical procedures. Yet, shell buckling loads below the small deflection theory predictions would not be surprising. This would be the case if the experimental moduli were used in the buckling expressions. Unfortunately, experimental values exist only for the longitudinal modulus of the cylinders tested. It should also be noted that the circumferentially wound cylinders failed in what appeared to be a transverse shear failure mode influenced by buckling. The analytical result was based on buckling alone.

The agreement between experimental and small deflection theory buckling loads raises the interesting question of the influence of imperfections on stability failure for filament wound composite shells. It is clear that this set of shells was imperfect. Yet, the imperfections in roving placement,

local wall thickness and the like are superimposed on the overall geometry which is of relatively precise form. That is, the mandrel results in a circular inner contour of high perfection, and the existing imperfections are of characteristic dimension which is small compared to the similar dimension for equivalent metallic shell construction. This could account for the composite buckling loads being a higher fraction of classical values than similar dimension metallic shells.

Conclusions: Variations in shell thickness and constituent volume fractions from shell to shell are large enough so that a direct comparison of buckling loads is not feasible. However, comparison of experiment and theory support the following conclusions.

The test results for this set of filament wound shells provided buckling loads in good agreement with the theory. The elastic moduli obtained are in poor agreement although the reasons for this are not well understood. These results indicate that the improvement in solid wall shell performance indicated analytically for hollow glass fiber composites exists in tests. Also, that the isotropic winding pattern (obtained by placing one third of the windings in each of three directions making equal angles with one another) yields highest buckling strength as predicted by the analytical studies.

4. Fatigue

Because of the extremely long test times involved in usual tests, this approach was abandoned in favor of a technique used by General Electric's Advanced Technology Labo ratories, Schenectady, New York. This method, the Prot progressive loading fatigue test, has been shown to give values of endurance limit in very close agreement with those determined in the Wohler steady stress method. It has the distinct advantage over the Wohler technique of reducing the test time by up to 90%. A thorough discussion of the method and an illustrative application to the evaluation of a non-reinforced plastic is given in Ref. 10.

The fatigue machine used for this study was a Sonntag SF-1-U Universal Fatigue Machine (See fig. 72). It is an alternating-force, axial fatigue machine operating at a frequency of 1800 R. P. M. The machine is equipped with smooth grips accurately aligned to minimize the possibility of applying bending or torsional stresses to the extended axial stress.

An oscillator has been added to the machine to permit changing the axial force being applied to the sample while the machine is operating. Thus, any sequence of stress levels may be applied to the sample without stopping the machine. In addition to the oscillator, a motor-driven set of gears was added which moves the oscillator such that a progressively increasing load may be applied to the sample. By changing the gears, a wide range of loading rates can be obtained (.03 to 22 lb/min.). These gears and the oscillator can both be clearly seen in fig. 72.

As the name of the fatigue test method implies, the primary difference from the Wohler technique is the application of the steadily (usually linearly) increasing load. It was discovered early in this program, however, that the equipment in use at ATL was incapable of applying the increasing load to high enough levels to cause failures in reasonable times. The first standard size specimen in hollow fibers ran over 10^7 cycles with no failure. It was decided to reduce the cross sectional area of the specimen to obtain the necessary failures. After several trials, a size of .10 inch by .10 inch was settled on.

Even with this low test area, the machine was forced to operate closer to its maximum capacity for longer periods than usual in such tests. As a result, a mechanical failure occurred in both the main bearing of the machine and in the device for applying the gradually increasing load. The tests ended at this point and the machine was torn down for repair. The damage was so extensive that the time required for repair precluded any further testing for this program.

The data obtained and recorded in Table 16 is however sufficient to determine the endurance limits for both hollow and solid configurations.

In the Prot test method, the data is presented as a plot of specimen rupture stress against the square root of the rate of load increase. Extending the straight line plot to the zero load rate line gives the endurance limit of the materials tested. Such a plot is shown as fig. 70. The endurance limits for the two material configurations tested can be seen to be approximately 44,000 psi for the solid fiber laminate and 32,000 psi for the hollow fiber laminate.

Fig. 71 shows both the specimen configuration as tested ans some failed specimens with the modes of failure clearly illustrated.

The question of temperature increase during testing was discussed several times with the test engineers. They have evaluated heat buildup in unreinforced plastics in the past but have never recorded temperature increases over about 10°F. Their usual precautions against such a heat buildup is to cool the test specimens with moving, ambient temperature air and such a technique was employed here by having a ventilating fan blow air on the specimen.

REFERENCES

1. Rosen B. W., Ketler, A. E., and Hashin, Z., "Hollow Glass Fiber Reinforced Plastics," General Electric Company, Philadelphia, Pa., Final Report, U.S. Navy, Bureau of Naval Weapons, Contract NOw-61-0613-d, Nov., 1962.

2. Rosen, B. W., "Tensile Failure of Fibrous Composites," presented at the AIAA Aerospace Sciences Meeting, New York, Jan., 1964, Preprint No. 64-73.

3. Sadowsky, M. A., "Transfer of Force by High-Strength Flakes in a Composite Material," Watervliet Arsenal, TR-WVT-RR-6015-R, June, 1961.

4. Dow, N. F., "Study of Stresses Near a Discontinuity in a Filament Reinforced Composite Metal," General Electric Company, Philadelphia, Pa., TIS R63SD61, August, 1963.

5. Hedgepeth, J., "Stress Concentrations in Filamentary Structures," NASA TN D-882, May 1961.

6. Von Hippel, A., "Dielectric Materials and Applications," MIT Tech. Press, 1954.

7. Hefty, R. W., and Jones, R. D., "Techniques for Measuring the Dielectric Properties of Materials at L-, S-, C-, and X-Band Frequencies," Materials Performance Technology, General Electric TIS R64SD252.

8. "Vermont Ball Winding System Vessel Preparation Components," Vermont Instrument Company, Inc., 62 Overlake Park, Burlington, Vermont.

9. "Vermont Ball Winding System Testing Component," Vermont Instrument Company, Inc., 62 Overlake Park, Burlington, Vermont.

10. Paganini, F. T., "Fatigue Properties of "Plexiglas II" - Determination of Fatigue Curve and Endurance Limit from Accelerated Fatigue Data," General Electric Company Report 61GL138, June, 1961.

11. Rosen, B. W., Dow, N. F., and Hashin, Z., "Mechanical Properties of Fibrous Composites," NASA CR-31, August 1963.

12. Rosen, B. W., "A Note on the Failure Modes of Fialment Reinforced Materials--Including the Influence of Constituent Geometry and Properties," Proceedings, 19th Annual Reinforced Plasticis Division Conference, SPI, Feb., 1964.

13. Hashin, Z., " The Elastic Moduli of Heterogeneous Materials," Journal of Applied Mechanics, Vol. 29, Trans. ASME, Vol. 84, 1962, pp. 143-150.

14. Stein, M. and Mayers, J., "Compressive Buckling of Simply Supported Curved Plates and Cylinders of Sandwich Construction," NACA TN 2601, Jan., 1952.

15. "Textile Fiber Materials for Industry," Owens Corning Fiberglas Corp., Feb., 1964.

16. Hashin, Z. and Rosen, B. W., "The Elastic Moduli of Fiber Reinforced Materials," Journal of Applied Mechanics, June, 1964.

17. Timoshenko, S., "Strength of Materials," Part, II, D. Van Nostrand Co., In., New York, 1930.

TABLE 1

GLASS FIBER PROPERTIES*

	Solid Fibers	Hollow Fibers
Material	E.glass	E glass
specific gravity	2.53 gm/cc	2.53 gm/cc
Young's modulus	10.7×10^6 psi	10.7×10^6 psi
α = hollowness ratio	0.0	0.6
$\alpha = \frac{ID}{OD}$		
Finish	HR 1156 finish with an Amino Silane coupling agent	
Ends per roving	10	20
Filaments per end	408	102
OD of single filament	0.00038 in.	0.0006 in.
ID of single filament	———	0.00036 in.

*Source: Pittsburgh Plate Glass Co., Pittsburgh, Pa.

TABLE 2

RESIN SYSTEMS

System No.	Ingredients	PBW	Cure	Potlife at 150°F	Tensile Strength (psi)	E (psi)	Tensile Elongation at Failure
1.	D. E. N. 438	80	2 hours at 212°F	1 1/2 hrs.			
	UNO x 206	20					
	MDA	36	3 hours at 350°F				
	Z-6040	0.5					
2.	D. E. N. 438	100	2 hours at 200°F	6 hrs.			
	MNA	101					
	BDMA	1.5	16 hours at 300°F				
	Z-6040	0.5					
3.	Shell Epon 828	100	2 hours at 200°F	-	10,200	4.6×10^5	2.3%
	MNA	90	4 hours at 250°F				
	BDMA	1.25	6 hours at 300°F				
4.	C. I. B. A. Araldite 6005	100	2 hours at 212°F	-	10,150	4.5×10^5	2.9%
	C. I. B. A. Araldite 906	88	2 hours at 280°F				
	BDMA	1.75	2 hours at 356°F				

TABLE 3

WINDING PROPERTIES OF LAMINATED PLATES

	β	ρ (lb/ft^3)	% Glass by Weight	% Resin by Weight
	0	127.5	77.55	22.45
$\alpha = 0$	45°	126.3	76.6	23.4
	60°	124.7	74.9	25.1
	0	91.9	64.7	35.3
$\alpha = 0.6$	45°	97.0	62.7	37.3
	60°	95.5	62.6	37.4

TABLE 4

TEST CONDITIONS AND RESULTS

Sample Variation			Frequency (mc)	Band	Dielectric Constant (k')	(k'')	Loss Tangent (tan δ)
1.	Longitudinal	1	1221	L	3.64	- j.108	.030
	Unidirectional	2 (Bond Hor.)	5525	C	3.64	- j.061	.017
	Hollow Fibers	3 (Bond Vert.)	5525	C	3.63	- j.062	.017
		4 (Bond Hor.)	9270	X	3.67	- j.051	.014
		5 (Bond Vert.)	9270	X	3.69	- j.051	.014
2.	Transverse	6	1221	L	3.75	- j.095	.025
	Unidirectional	7	5525	C	3.53	- j.058	.017
	Hollow Fibers	8	9270	X	3.58	- j.054	.015
3.	Transverse	9	1221	L	4.93	- j.108	.022
	Unidirectional	10	5525	C	4.66	- j.074	.016
	Solid Fibers	11	9270	X	4.70	- j.068	.015
4.	Transverse	12	1221	L	3.59	- j.142	.040
	Bidirectional	13	5525	C	3.76	- j.067	.018
	90^{o} Hollow Fibers	14	9270	X	3.79	- j.059	.016
5.	Transverse	15	1221	L	4.85	- j.106	.022
	Bidirectional	16	5525	C	4.81	- j.093	.019
	90^{o} Solid Fibers	17	9270	X	4.81	- j.062	.013

TABLE 5

MICROWAVE EQUIPMENT LIST

	Equipment	Manufacturer	Type
C Band	Isolator	PRD Electronics Inc.	1205
	SHF Signal Gen. 3800-7600 mc	Hewlett-Packard	618B
	Slotted Line	Hewlett-Packard	G810B
	Standing Wave Amplifier	PRD Electronics Inc.	2778
X Band	SHF Signal Gen. 7000-11,000 mc	Hewlett-Packard	620A
	Slotted Line	Hewlett-Packard	X810B
	Isolator	PRD Electronics Inc.	1203
L Band	UHF Signal Gen. 450-1230 mc	Hewlett-Packard	612A
	Unit Oscillator 900-2000 mc	General Radio Co.	1218-A
	Unit 1-F Amplifier	General Radio Co.	1216-A
	Microwave Signal Generator 1800-4400 mc	Empire Devices Inc.	SG-12
	Slotted Line	Alford Manufacturing Co.	2181-2
	Isolator	PRD Electronics Inc.	1210-A

TABLE 6

SUMMARY, TEST DATA - ABLATION OF GLASS FIBERS

Run No.	Model	Air Mass Flow #/sec	Plenum Pressure Psia	Time Sec.	Mass Loss Grams	Length Loss In.	q^* Btu/# Mass Base	q^* Btu/# Length Base
2607	H. F. ** 90° T. B.	0.0094	41	10	4.3747	.5160	3600	3540
2608	S. F. *** UNID.		37		5.3512	.4357	2860	2950
2609	S. F. + 90° T. B.		42		5.2377	.4327	2920	3040
2610	H. F. ++ UNID.		42		4.6283	.4945	3250	3530
2611	H. F. 90° T. B.		41		4.5782	.5226	3440	3500
2612	S. F. 90° T. B.		41		5.3787	.4537	2850	2900
2613	H. F. UNID.		42		4.7203	.4962	3290	3640
2616	S. F. UNID.		41		5.5392	.4475	2760	2940

**Hollow Fiber, 90° Transverse Bidirectional
***Solid Fiber, Unidirectional
+Solid Fiber, 90° Transverse Bidirectional
++Hollow Fiber, Unidirectional

$\dot{q}$ = 1850 Btu/sec. ft.^{2}, Cold wall calorimeter

TABLE 7

HOLLOW GLASS FIBER AND BOTTLE WINDING GEOMETRIES

Filament material	E glass
Filament finish	PPG-HR1156 binder with Amino-Silane coupling agent
Ends per roving	20
Filaments per end	102
Filaments per roving	2040
Outside diameter of filament	0.0006 in.
Inside diameter of filament	0.00036 in.
$\alpha = \frac{ID}{OD} = \frac{.00036}{.0006}$	0.6
Cross sectional area of filament	1.81×10^{-7} sq. in.
Number of turns to just cover mandrel	225
Number of single filaments at equator	918,000
Cross sectional area of bottle through equator	46 sq. in.

TABLE 8

HOLLOW FIBER OUTWATER BOTTLE TEST RESULTS--
RESIN SYSTEM NO. 2

Bottle No. (1)	Burst Pressure (psi)	Filament Tensile Stress at Burst (psi) (2)
1	385	114,000
2	360	107,000
3	370	110,000
4	380	113,000
5	385	114,000
	avg: 376	112,000

(1) Cure Cycle: 2 hours at 200°F

16 hours at 300°F

Slow cool to room temperature (50°F per hour)

Mandrel removal

Dried 2 hours at 225°F

(2) Corrected for winding angle.

TABLE 9

HOLLOW FIBER OUTWATER BOTTLE TEST RESULTS--
RESIN SYSTEM NO. 3

Bottle No.		Burst Pressure (psi)	Filament Tensile Stress at Burst (psi) (4)
8		490	128,850
9		416	109,390
10	(1)	420	110,440
11		430	113,000
12		410	107,800
13		485	127,500
14	(2)	475	124,900
15		420	110,400
16	(3)	460	121,000
17		408	107,300
18	(2)	455	119,600
		avg: 443	116,000

Cure Cycle: (1) 2 hours at 212°F

3 hours at 260°F

Slow cool to room temperature (50°F per hr)

Mandrel Removal

Postcure: 2 hours at 212°F

1 hour at 250°F

TABLE 9 (Continued)

		1 hour at 300°F
		2 hours at 360°F
		Slow cool to room temperature (50°F per hr)
Cure Cycle:	(2)	2 hours at 212°F
		6 hours at 260°F
		Slow cool to room temperature (50°F per hr)
		Remove mandrel
Postcure:		2 hours at 212°F
		1 hour at 250°F
		1 hour at 300°F
		2 hours at 360°F
		Slow cool to room temperature (50°F per hr)
	(4)	Corrected for winding angle.

TABLE 10

SOLID GLASS FIBER AND BOTTLE WINDING GEOMETRIES

Filament material	E glass
Filament finish	PPG-HR 1156 binder with Amino Silane coupling agent
Ends per roving	10
Filaments per end	408
Filaments per roving	4080
Outside diameter of filament	0.0038 in.
Cross sectional area of filament	1.13×10^{-7} sq. in.
Number of turns to just cover mandrel	292
Number of single filaments at equator	2,382,720
Cross sectional area of bottle through equator	46 sq. in.

TABLE 11

SOLID FIBER OUTWATER BOTTLE TEST RESULTS--
RESIN SYSTEM NO. 3

Bottle No. (1)	Burst Pressure (psi)	Individual Filament Tensile Stress at Burst (psi) (2)
19	575	104,500
20	690	125,400
21	720	130,800
22	730	132,600
23	670	121,700
	avg: 677	123,000

(1) Cure Cycle: 2 hours at 212°F

6 hours at 260°F

Slow cool to room temperature (50°F per hr)

Remove mandrel

Postcure: 2 hours at 212°F

1 hour at 250°F

1 hour at 300°F

2 hours at 360°F

Slow cool to room temperature (50°F per hr)

(2) Corrected for winding angle.

TABLE 12

GEOMETRIES OF HYDROSTATIC SHELLS

Shell No.	ID (in.)	L (in.)	Ag. Wall Thickness (in.)	Helix Angle (β)	Fiber Hollowness Ratio (ID/OD = α) 0 = solid .6 = hollow
33	8	16	.047	30°	0
34	↓	↓			
7				30°	.6
8					
29			.058	90°	0
30					
3				90°	.6
4					
35			.063	60° Iso	0
36					
11			.086	60° Iso	.6
12					
31A			.345	90°	0
32A					
13	↓	↓	.495	90°	.6
14					

TABLE 13

(See fig. 58)

MATERIALS USED IN SEALING THICK-WALL SHELLS

1. Apiezon sealing compound (Q)
   Mfg. by Associated Electricl Ind., Ltd.
   England
   Sold by James G. Biddle Co.
   Plymouth Meeting, Pa.

2. Apiezon wax (W)

3. Johns Manville Duxseal

4. Polyethylene sheet, .005 inch

5. Neoprene rubber weather balloon
   .004 inch thick-24 inch long-100 gr.
   Kaysam Corp. of America
   Patterson, N. J.

6. Sealed by plastic tape

7. Polyethyene sheet, .005 inch

8. Glass reinforced cylinder

TABLE 14

EXPERIMENTAL FAILURE LOADS FOR CYLINDERS
IN AXIAL COMPRESSION

Spec. No.	Fibers	Winding	Volume Fraction				t (in)	Max. Load (kips)
			v_f	v_b	v_a	v_o*		
9	Solid	Circumferential	0.58	0.39	0.03	----	0.0625	27.8
10	"	"	0.58	0.39	0.03	----	0.0625	28.8
19	"	30° Helical	0.49	0.45	0.07	----	0.0495	11.23
20	"	"	0.49	0.45	0.07	----	0.0495	10.02
21	"	60° Isotropic	0.49	0.40	0.10	----	0.0670	----
22	"	"	0.49	0.40	0.10	----	0.0670	27.0
23	Hollow	30° Helical	0.22	0.57	0.21	0.12	0.0790	18.80
24	"	"	0.22	0.57	0.21	0.12	0.0790	18.37
25	"	60° Isotropic	0.25	0.49	0.26	0.14	0.1025	37.5
26	"	"	0.25	0.49	0.26	0.14	0.1025	36.5
27	"	Circumferential	0.28	0.49	0.23	0.16	0.0615	12.60
28	"	"	0.28	0.49	0.23	0.16	0.0615	9.45

*Based on α = 0.6

TABLE 15

EXPERIMENTAL AND ANALYTICAL YOUNG'S MODULUS DATA

Fiber	Winding	E_{anal}	Spec. No.	E_{exp} (strain)	E_{exp} (Displacement) (First Run)	(Rerun)
Solid	30°	2.14	19	2.96	2.76	2.76
		2.14	20	2.53	2.87	2.41
	90°	1.22	9	1.60	1.54	
		1.22	10	1.78	1.61	
	iso	1.62	21			2.85
		1.62	22	2.94	2.36	2.32
Hollow	30°	1.21	23	1.48	1.33	1.33
		1.21	24	1.51	1.33	1.28
	90°	0.62	27	0.79	0.63	
		0.62	28	0.65	0.60	
	iso	0.98	25	1.52	1.26	
		0.98	26	1.48	1.37	

TABLE 16

FATIGUE TEST RESULTS

Solid Fiber Laminate (α = 0)

Sample No.	Load Rate (lb/min)	Cross Section (in^2)	Load Rate (psi/min)	Rupture Stress (psi)	Cycle to Failure
1	Steady	.0372	---	24,200	No failure - 7.7×10^6 cycles
5	.112	.0123	9.1	46,500	9,259,000
6	.45	.0125	36.0	52,200	2,644,000
4	.89	.0131	67.9	54,700	1,455,000
2	2.25	.0120	188	56,200	548,000
3	2.25	.0098	230	60,000	476,000

Hollow Fiber Laminate (α = 0.6)

15	Steady	.0840	---	11,100	No failure - 10^7 cycles
5	.112	.0126	8.9	37,500	7,659,000
7	.112	.0107	10.5	39,400	6,839,000
3	.45	.0121	37.5	40,700	1,998,000
6	.89	.0124	71.7	46,900	1,179,000

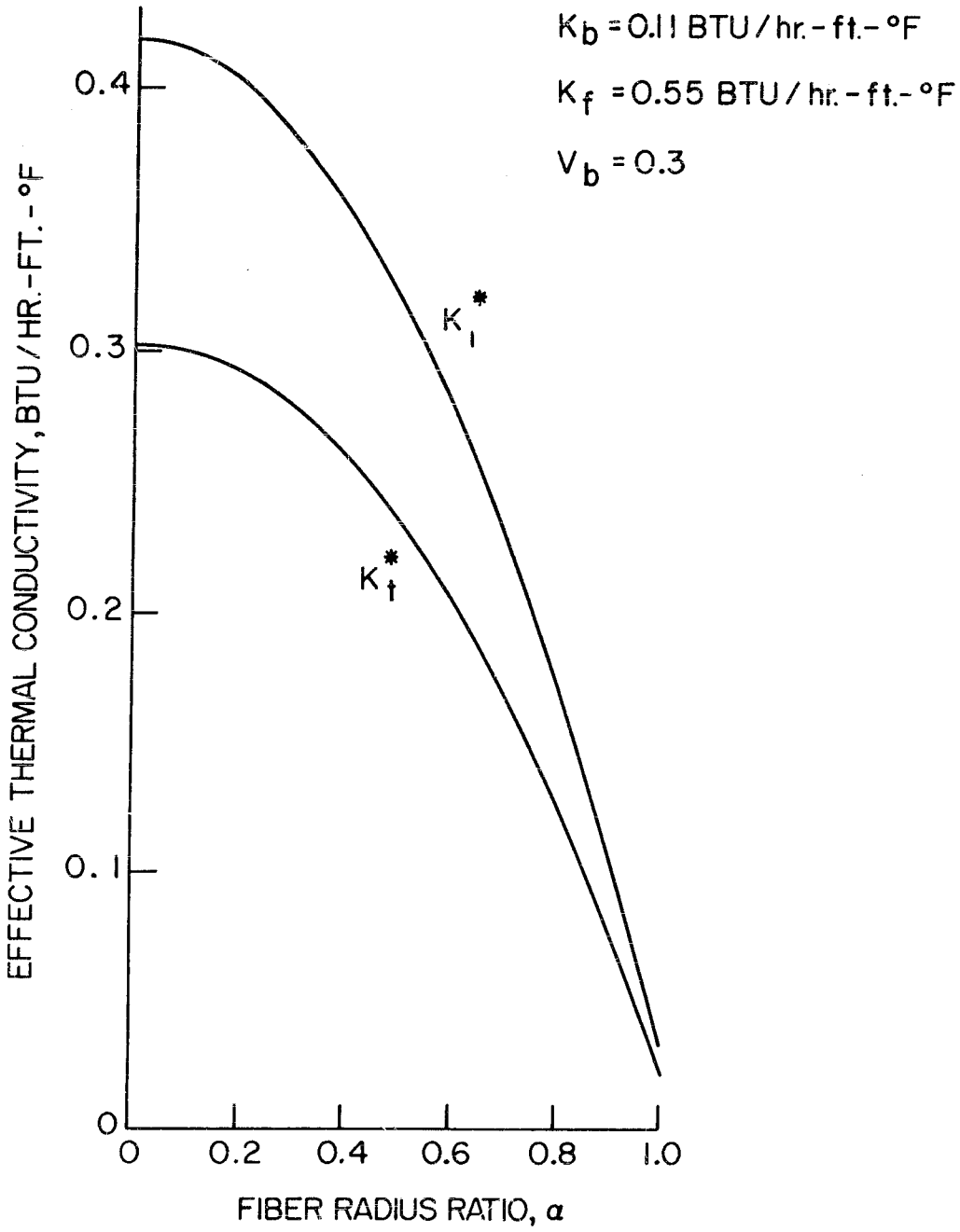

Figure 1. Effective Thermal Conductivities of Glass-Epoxy Fibrous Composites

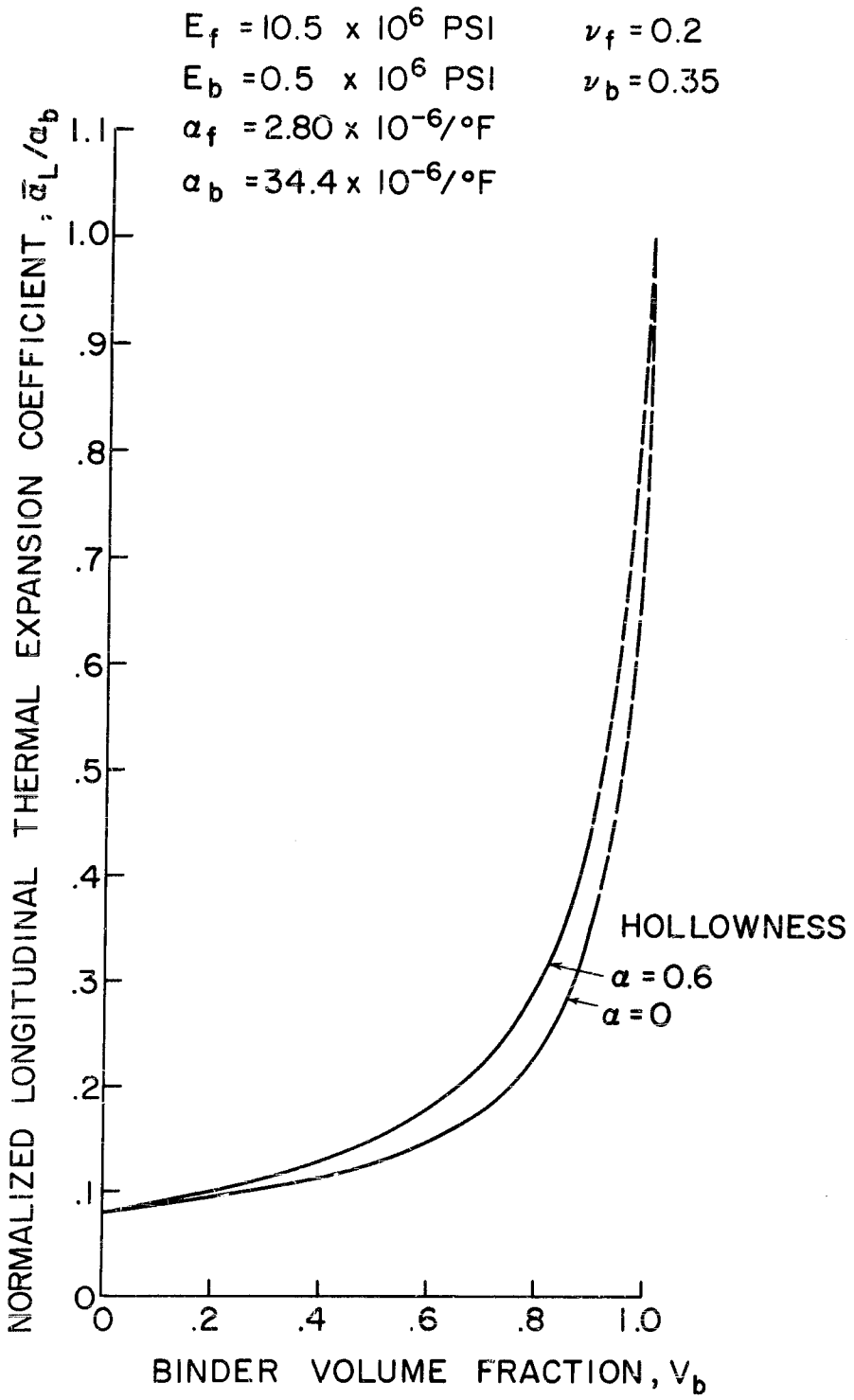

Figure 2. Effective Thermal Expansion Coefficients of Glass-Epoxy Fibrous Composites. a. Longitudinal

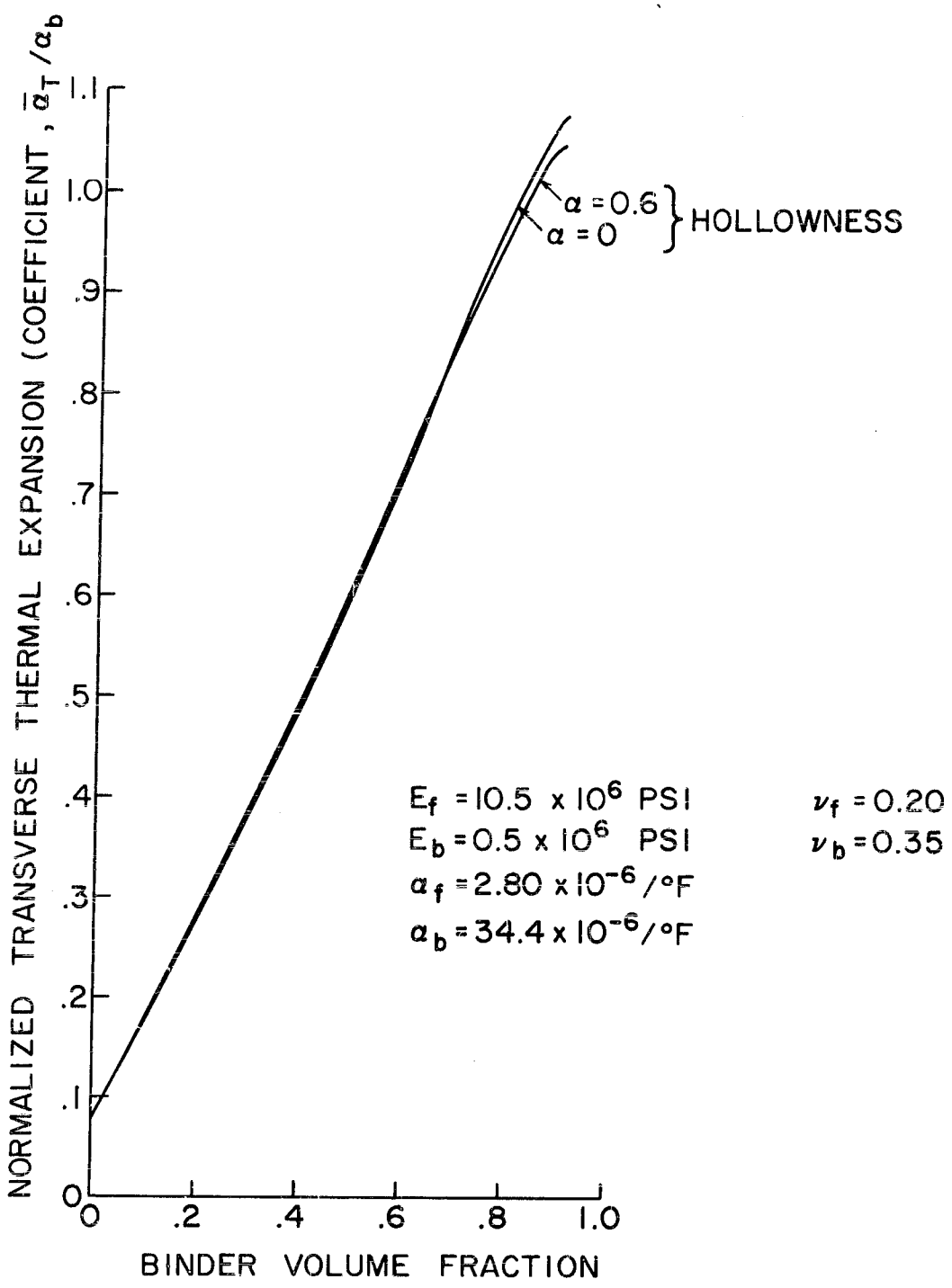

Figure 2. Effective Thermal Expansion Coefficients of Glass-Epoxy Fibrous Composites. b. Transverse

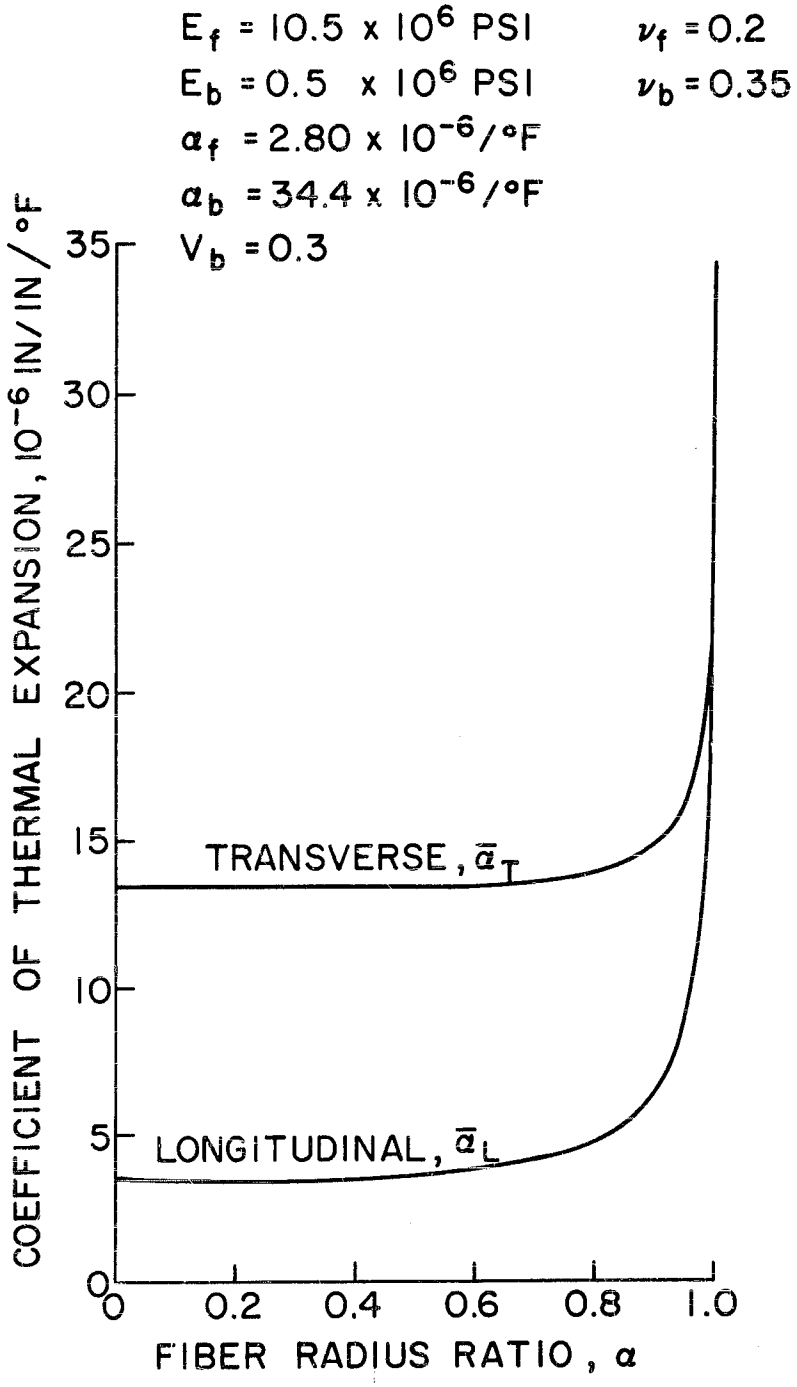

Figure 3. Effect of Fiber Hollowness on Composite Thermal Expansion

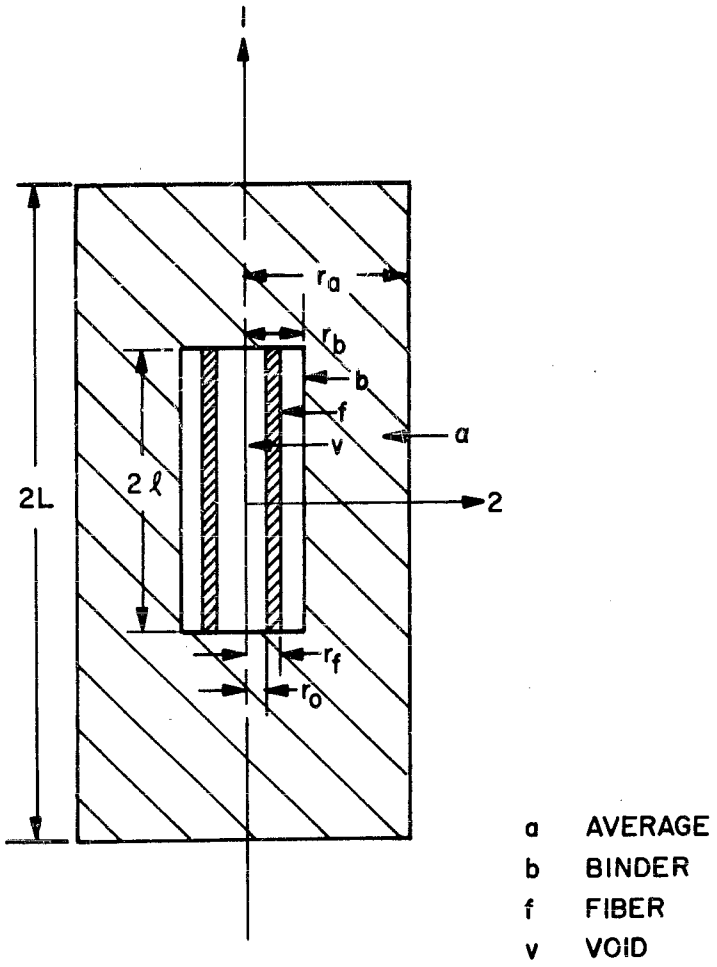

COMPOSITE MODEL

Figure 4. Model for Analysis of Internal Stresses in a Fibrous Composite

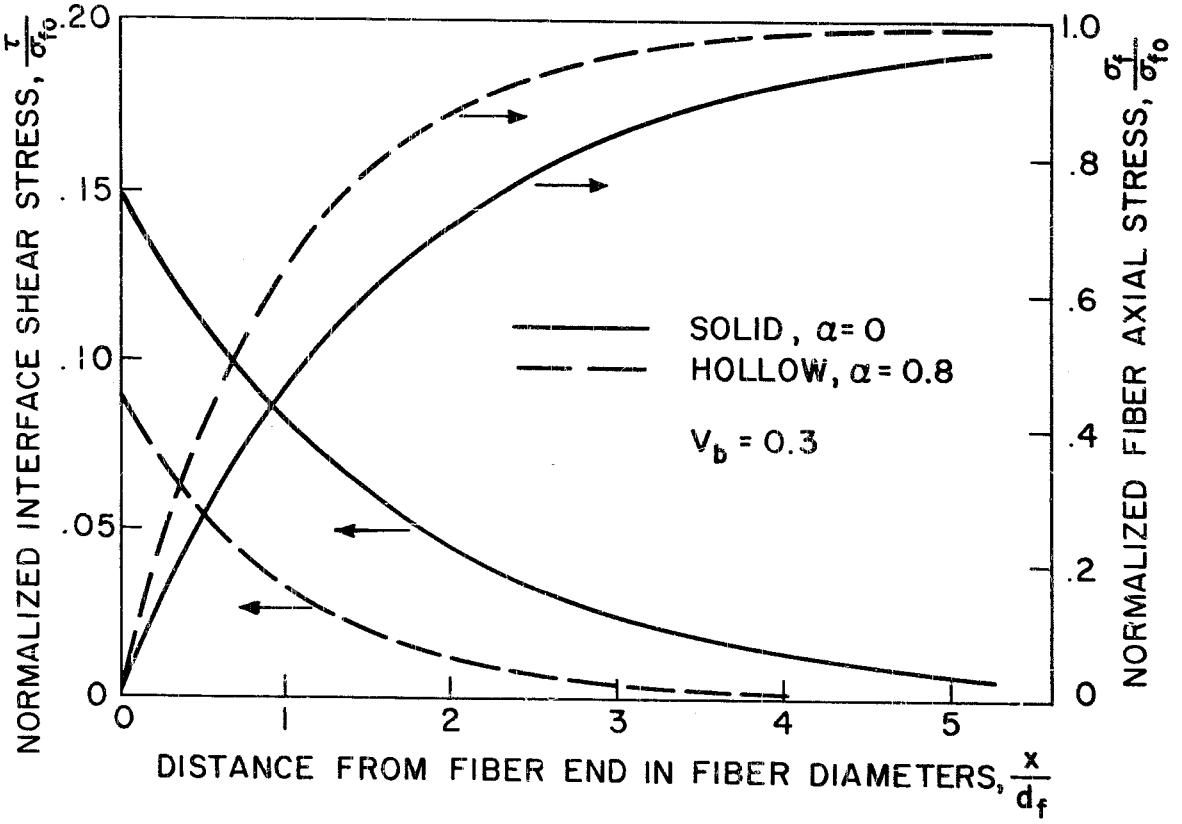

Figure 5. Interface Shear Stress and Fiber Axial Stress in the Vicinity of an Internal Fiber Break

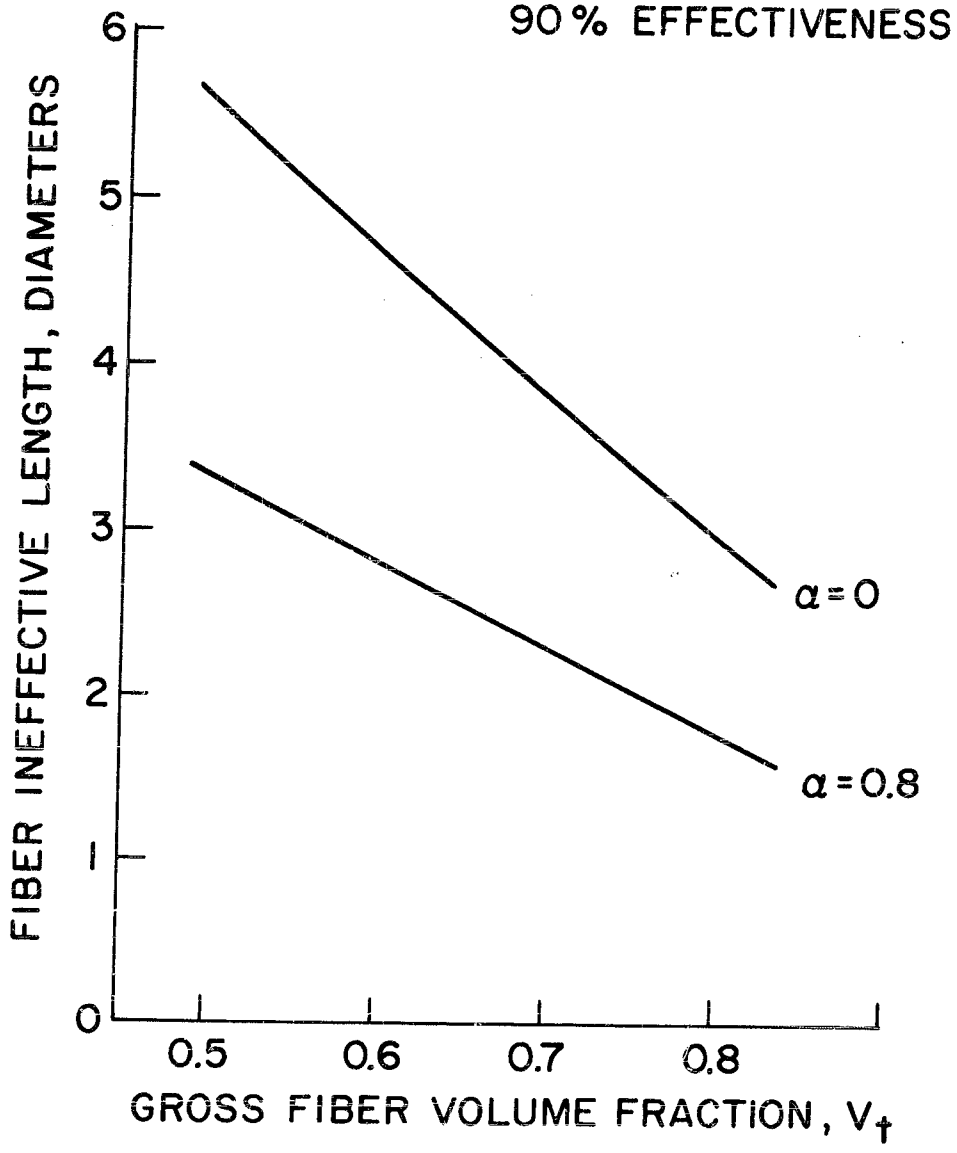

Figure 6. Fiber Ineffective Length in a Glass-Epoxy Composite

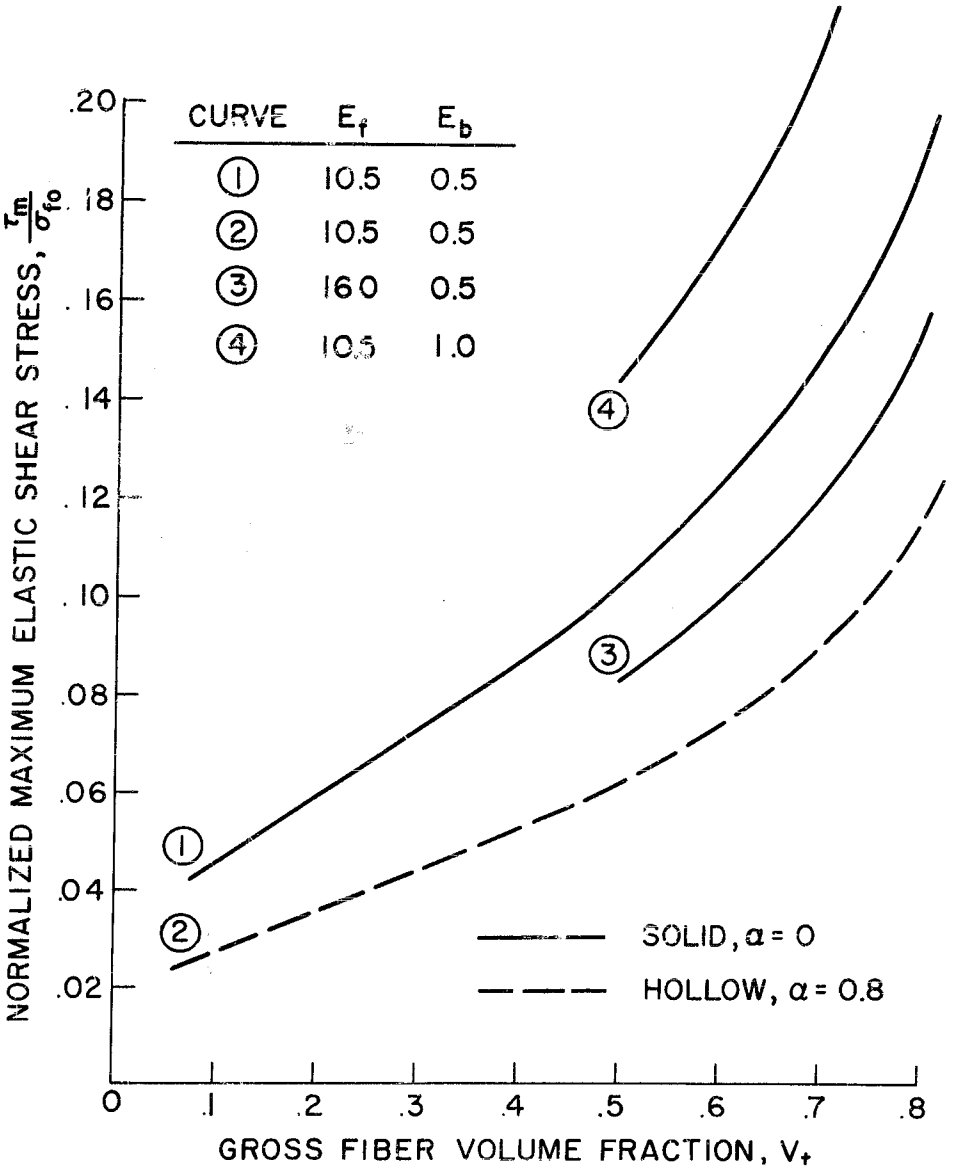

Figure 7. Maximum Elastic Interface Shear Stress in a Glass-Epoxy Composite

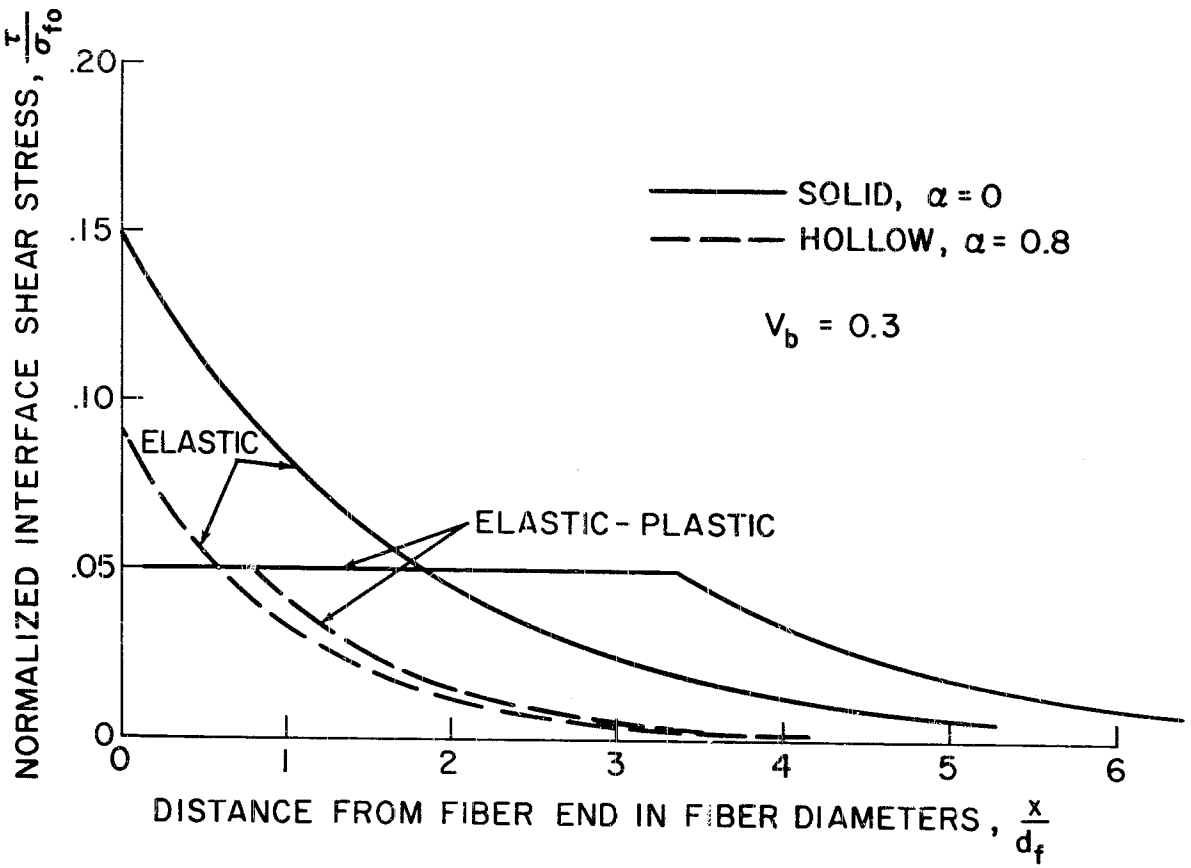

Figure 8. Effect of Elastic-Plastic Binder Material on Shear Stress Distribution

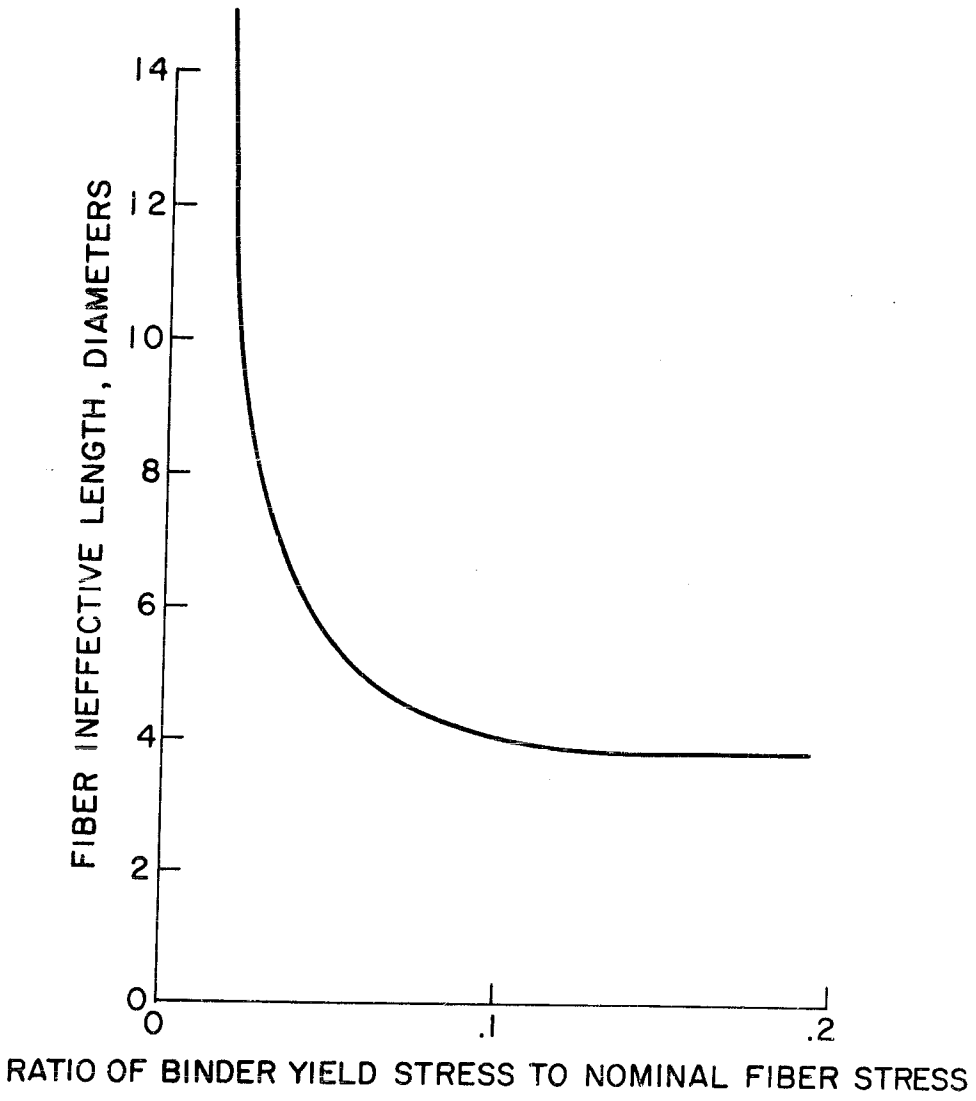

Figure 9. Effect of Yield Stress of an Elastic-Plastic Binder Material upon the Fiber Ineffective Length

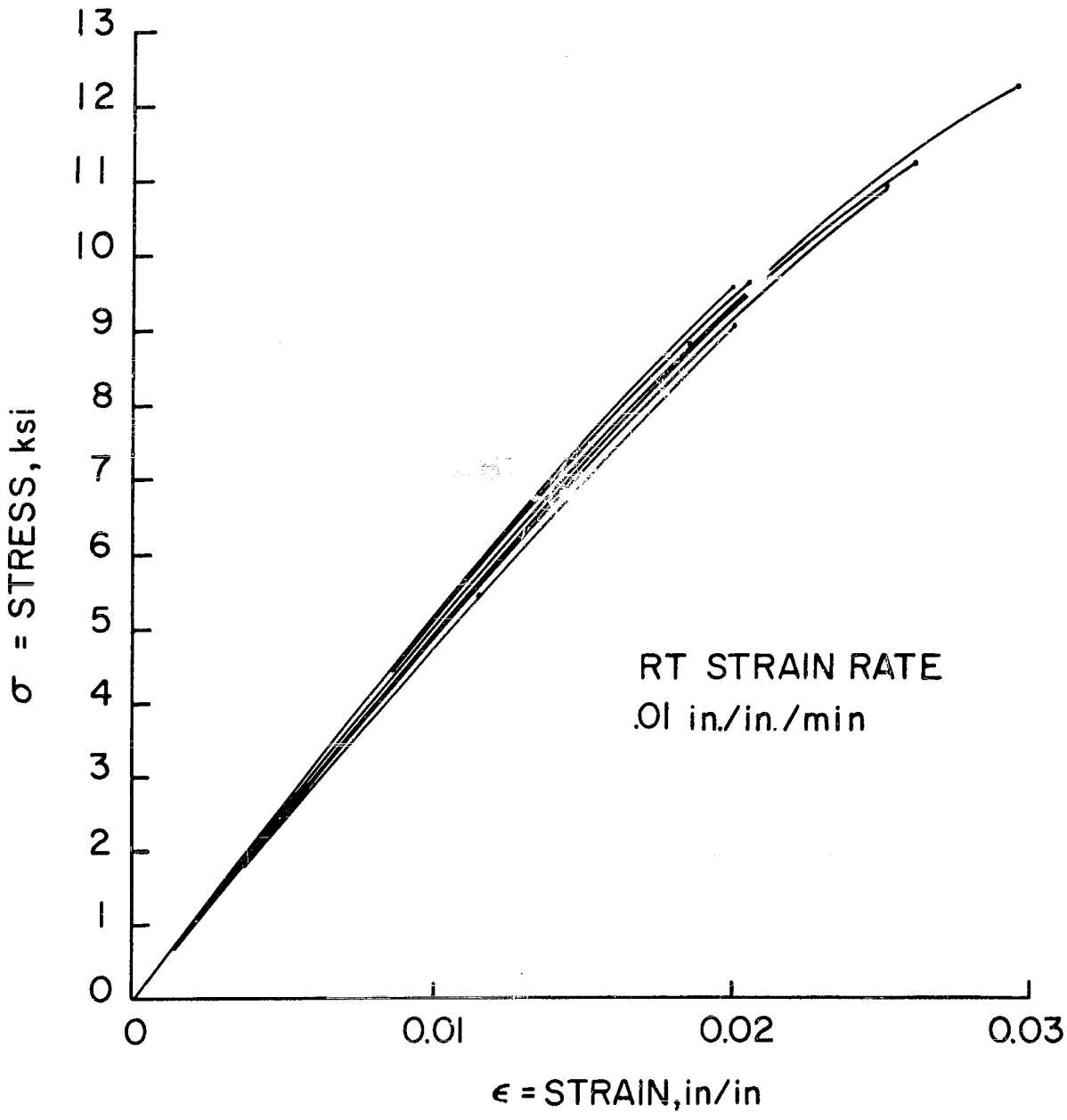

Fig. 10. Stress-Strain Curve of Reference Epoxy System

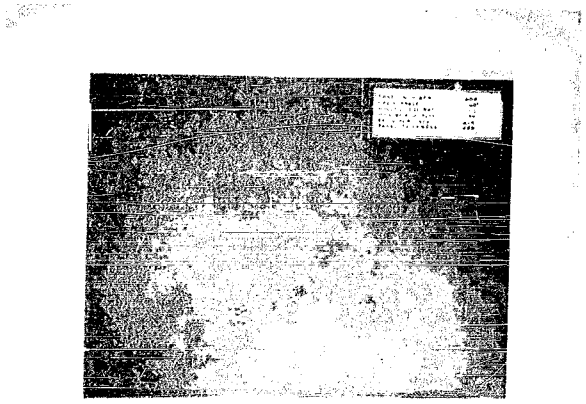

Figure 11. Laminated Flat Plates Made by 3M's Company

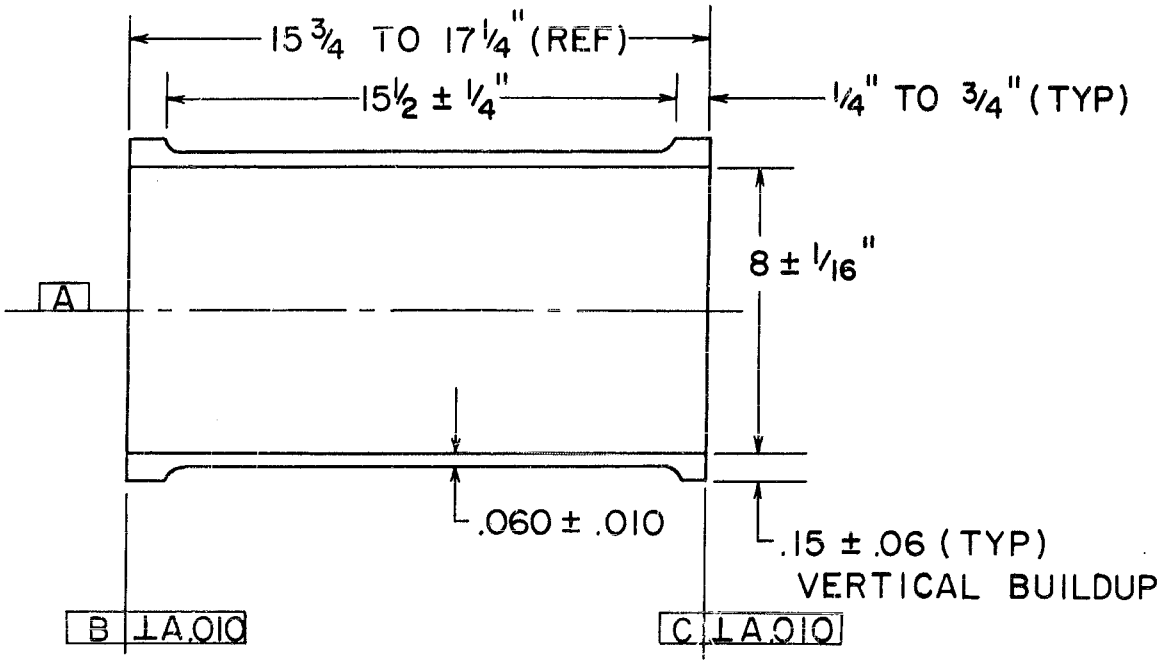

Figure 12. Geometry of 8" D x 16" L Thin Wall Shells

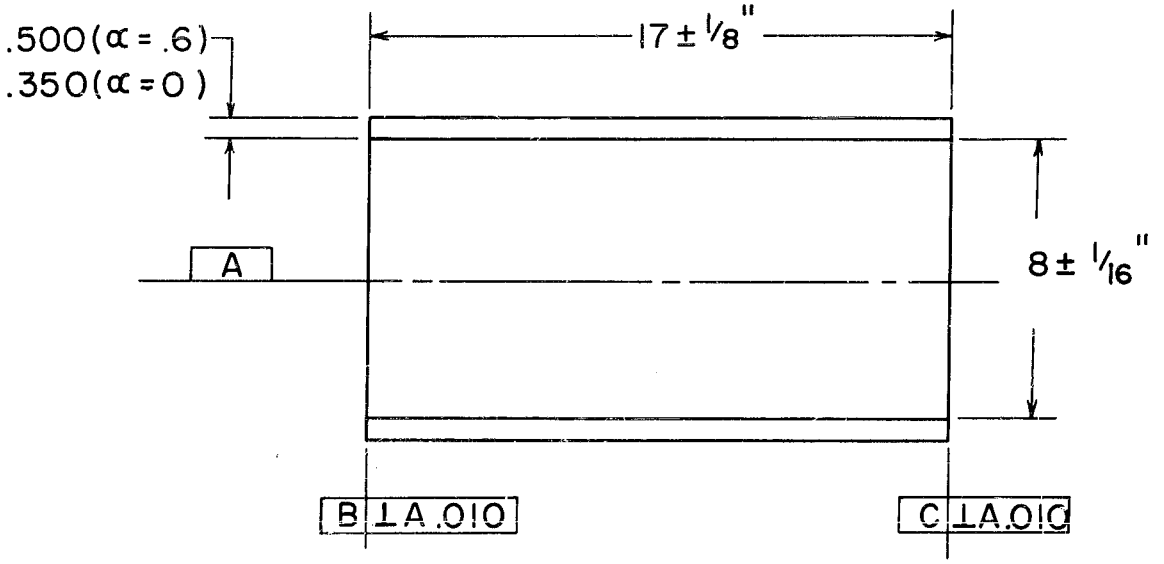

Figure 13. Geometry of 8" D x 16" L Thick Wall Shells

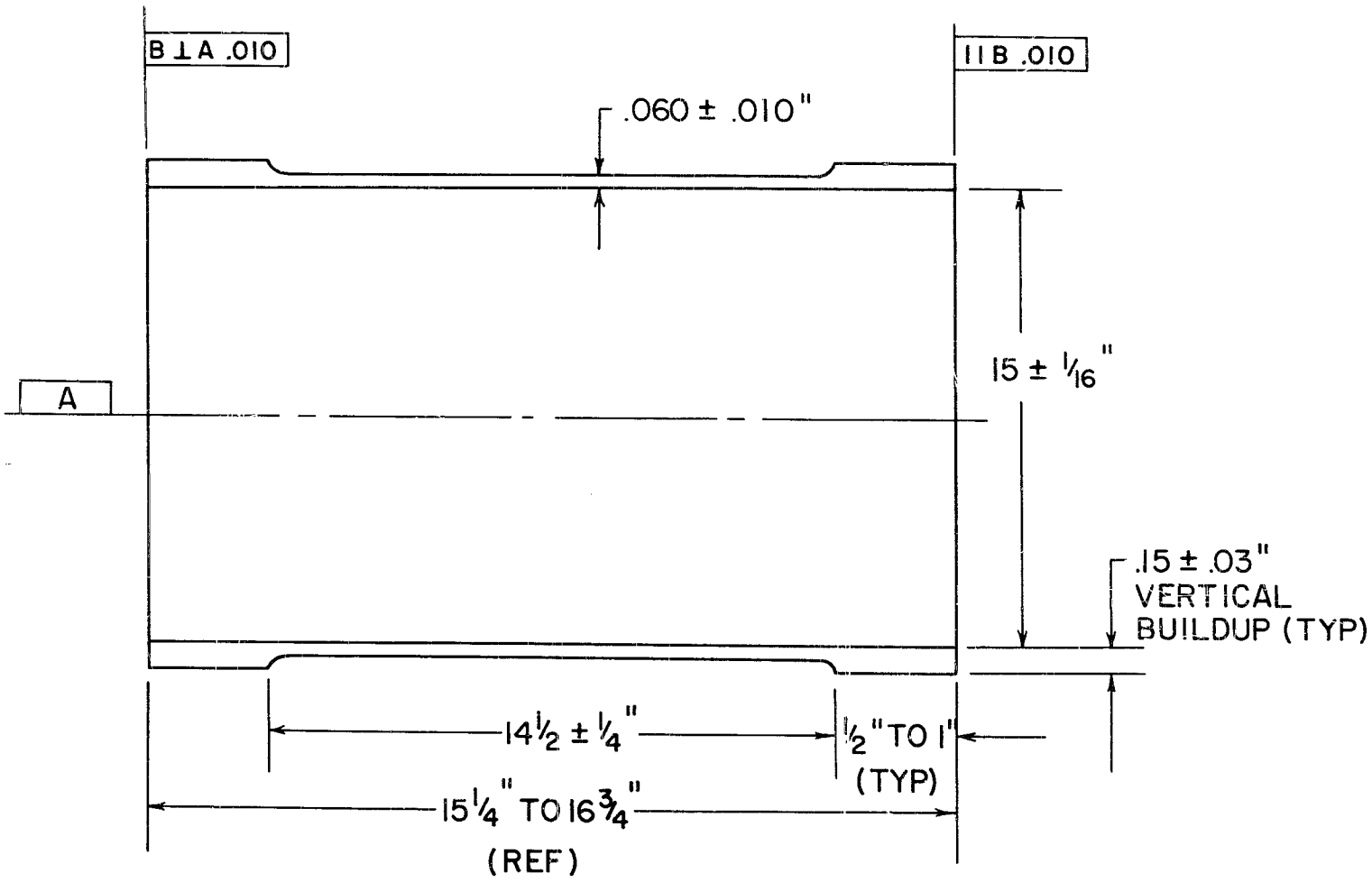

Figure 14. Geometry of 15" D x 15" L Shells

	1 LONGITUDINAL UNIDIRECTIONAL HOLLOW FIBERS	2 TRANSVERSE UNIDIRECTIONAL HOLLOW FIBERS	3 TRANSVERSE UNIDIRECTIONAL SOLID FIBERS	4 TRANSVERSE BIDIRECTIONAL HOLLOW FIBERS	5 TRANSVERSE BIDIRECTIONAL SOLID FIBERS
L BAND 1221 MC	#1 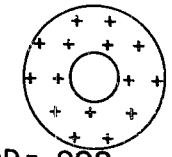 OD = .998 ID = .435 t = .25	#6 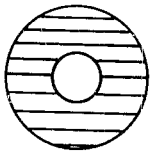	#9 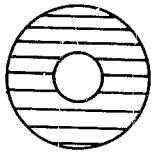	#12 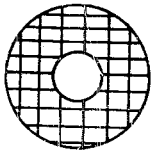	#15 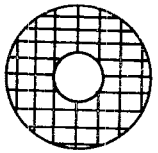
C BAND 5525 MC	#2 & #3 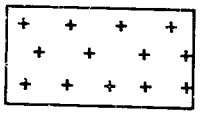 L = 1.862 W = .869 t = .25	#7 	#10 	#13 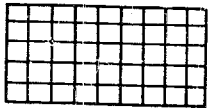	#16 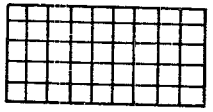
X BAND 9270 MC	#4 & #5 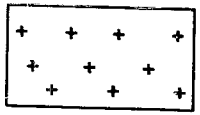 L = .893 W = .400 t = .25	#8 	#11 	#14 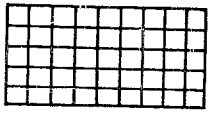	#17 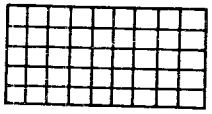

Figure 15. Electrical Property Test Specimen Configurations

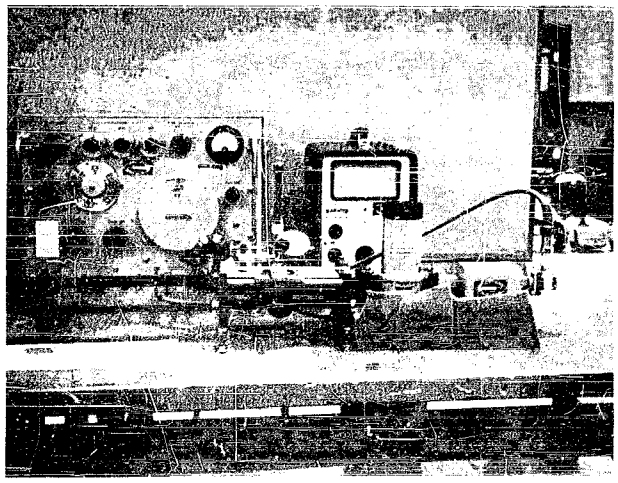

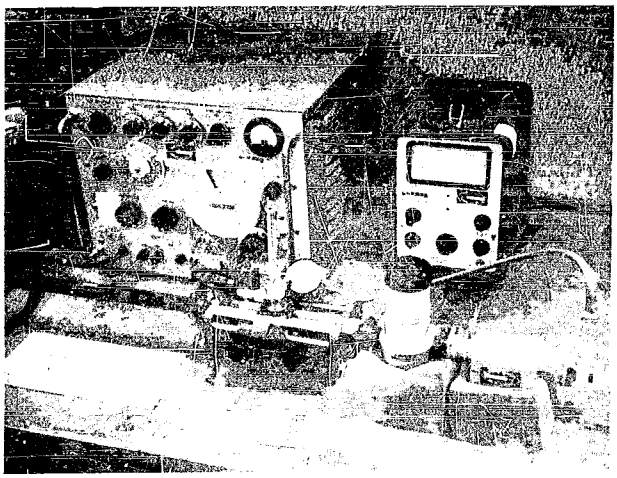

Figure 16. C-Band and X-Band Test Setup with Specimens

Figure 17. L-Band Test Setup with Specimens

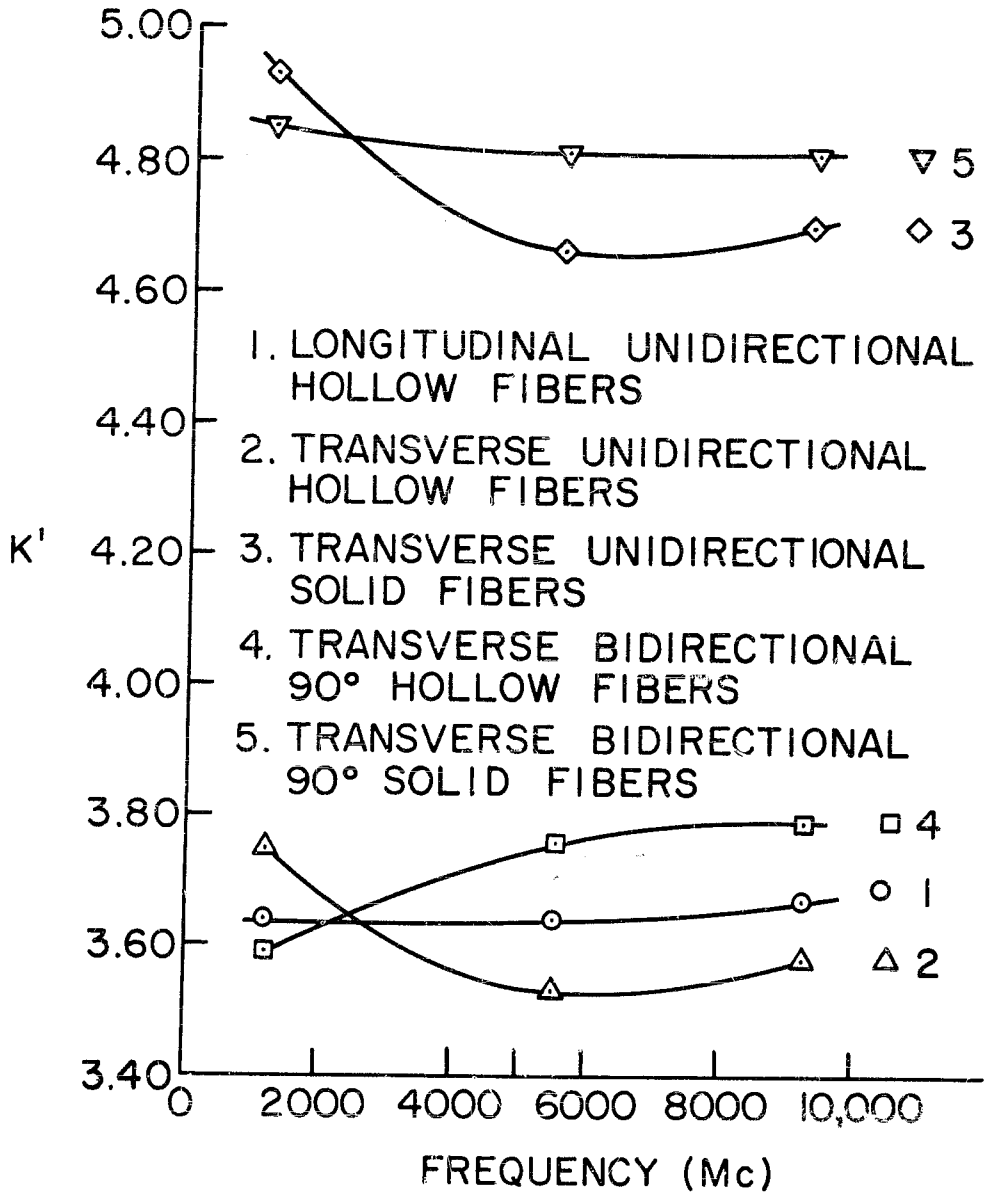

Figure 18. Variation of Dielectric Constant with Frequency

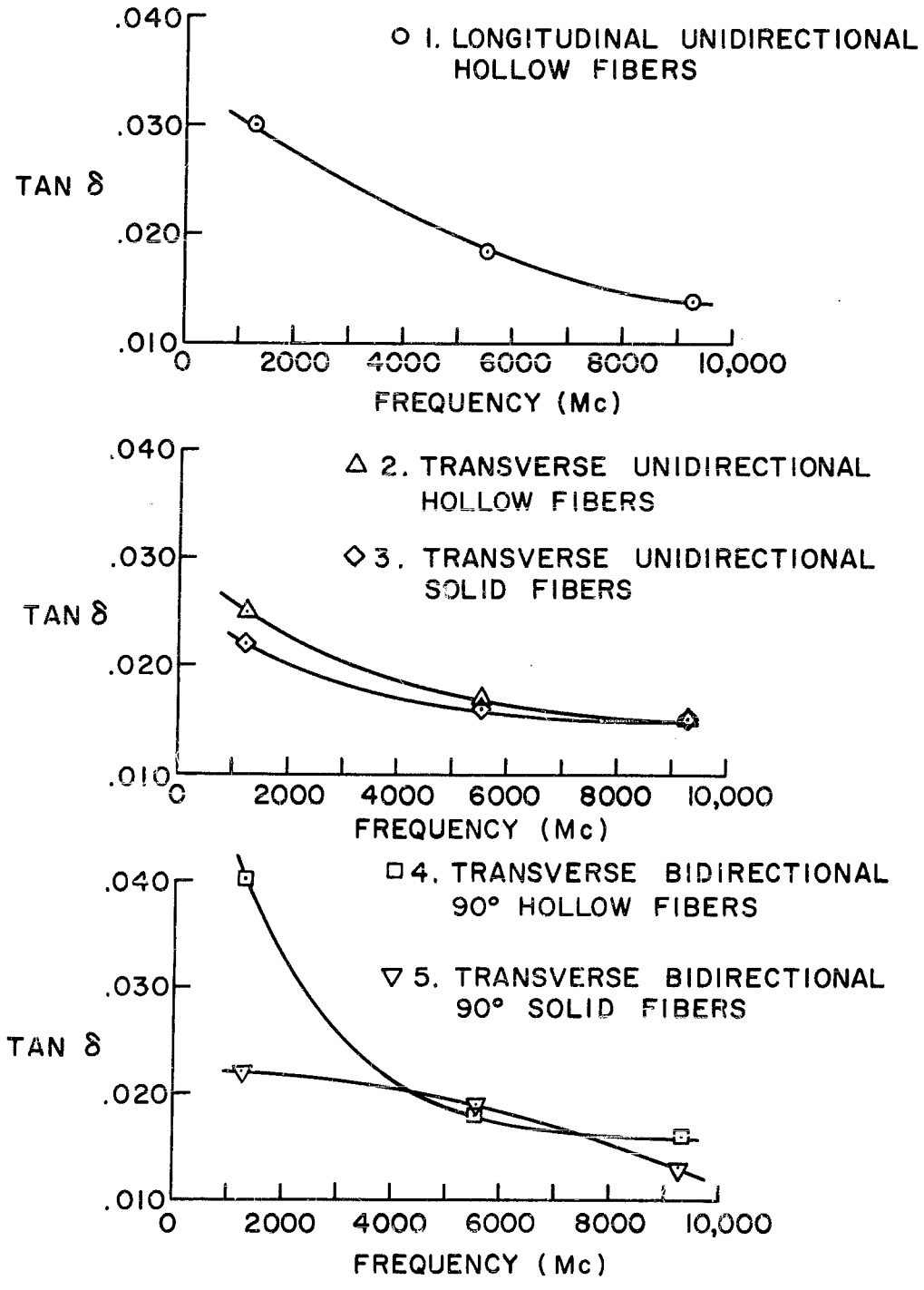

Figure 19. Variation of Loss Tangent with Frequency

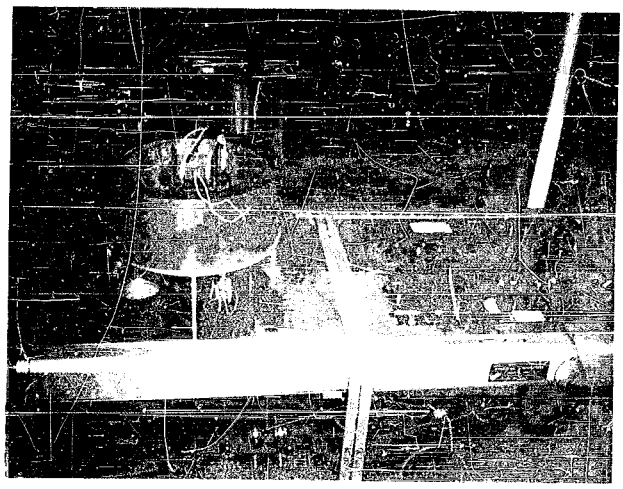

Figure 20. Thermal Conductivity Test Apparatus

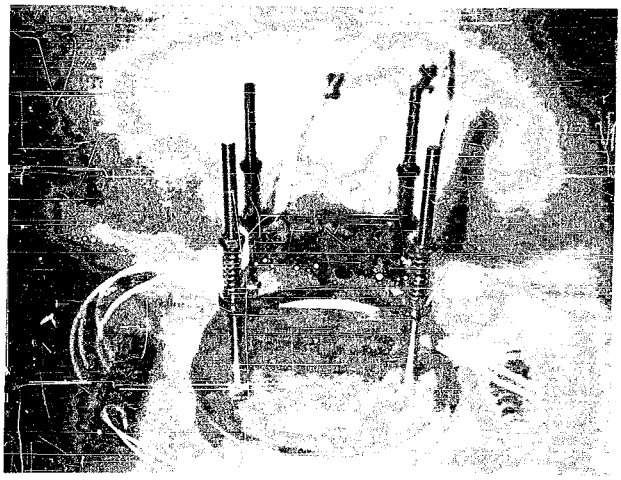

Figure 21. Thermal Conductivity Test Stack

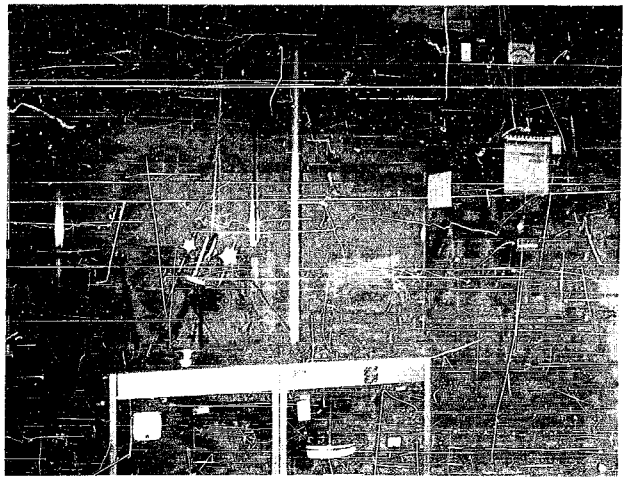

Figure 22. Thermal Specific Heat Test Apparatus

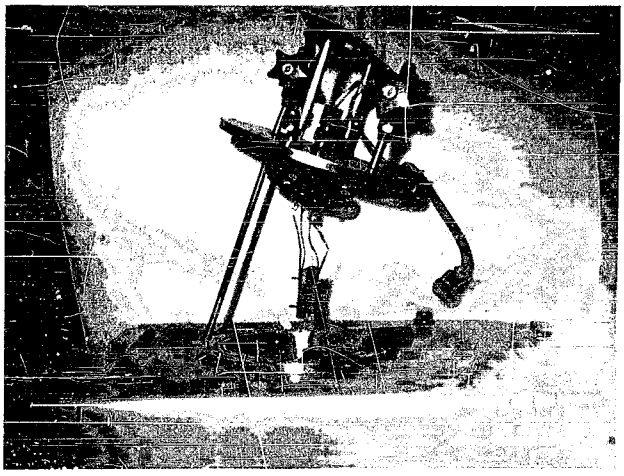

Figure 23. Specific Heat Test Stack

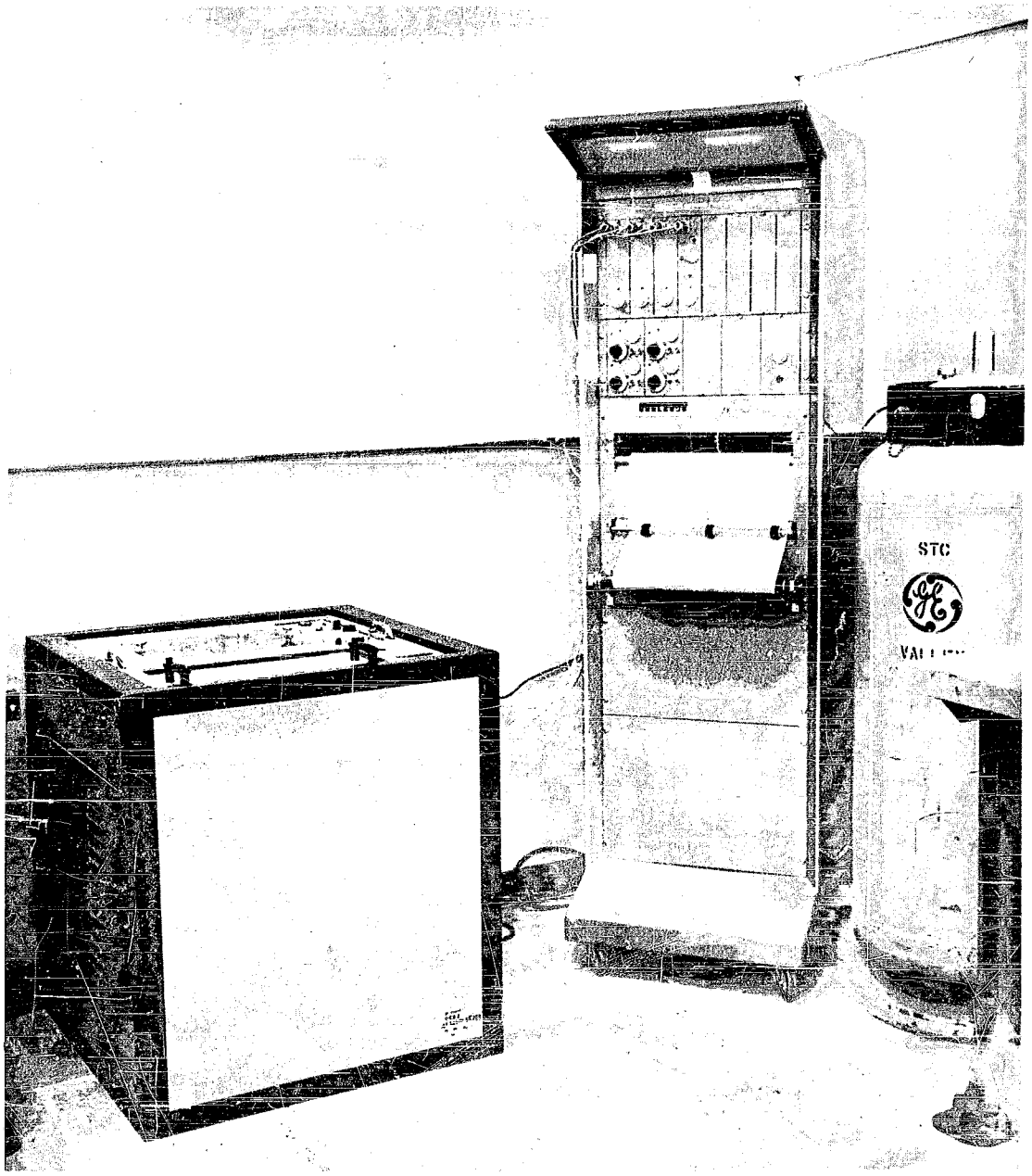

Figure 24. Thermal Expansion Test Equipment

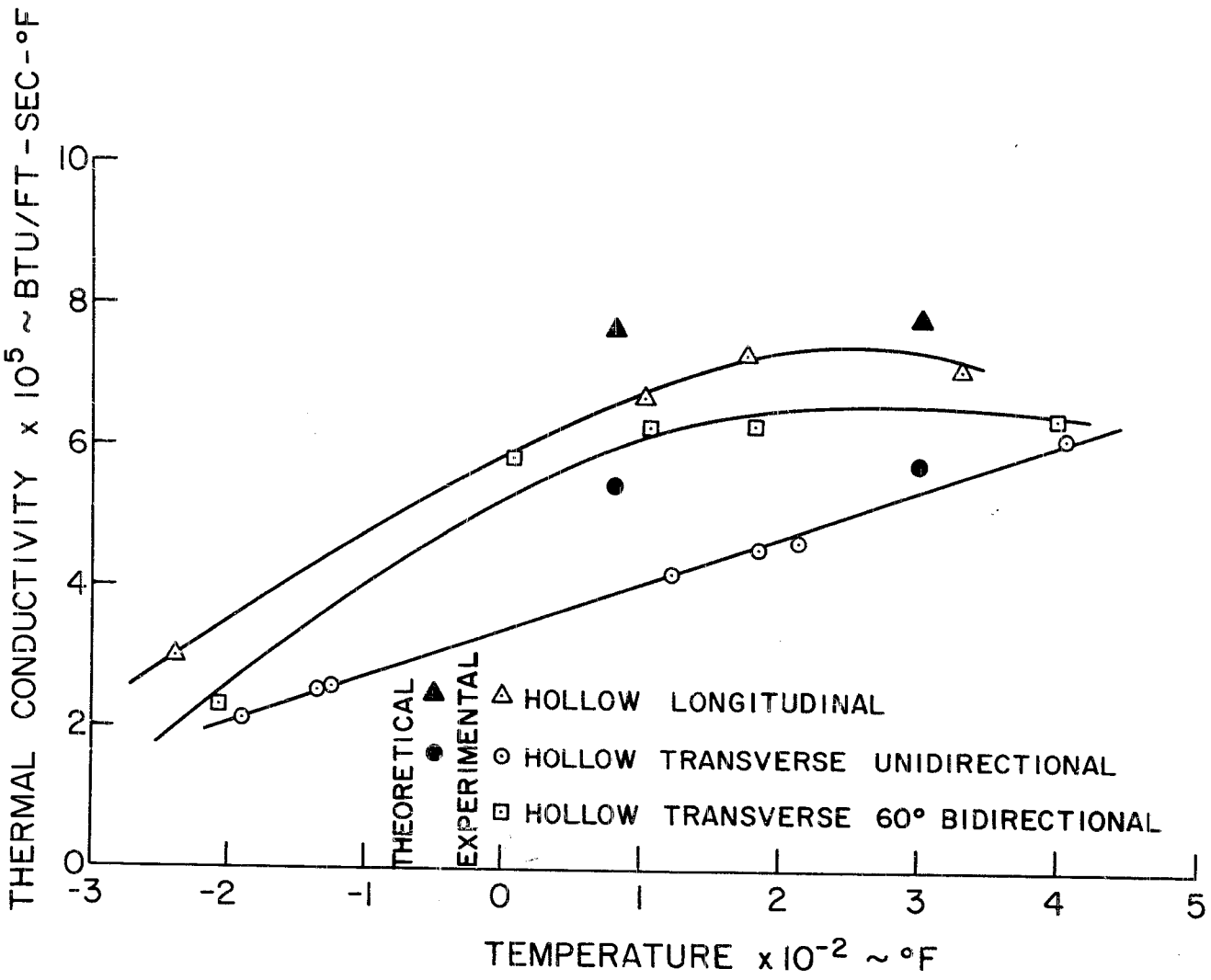

Figure 25. Thermal Conductivity of Hollow Glass Epon 828 Composite

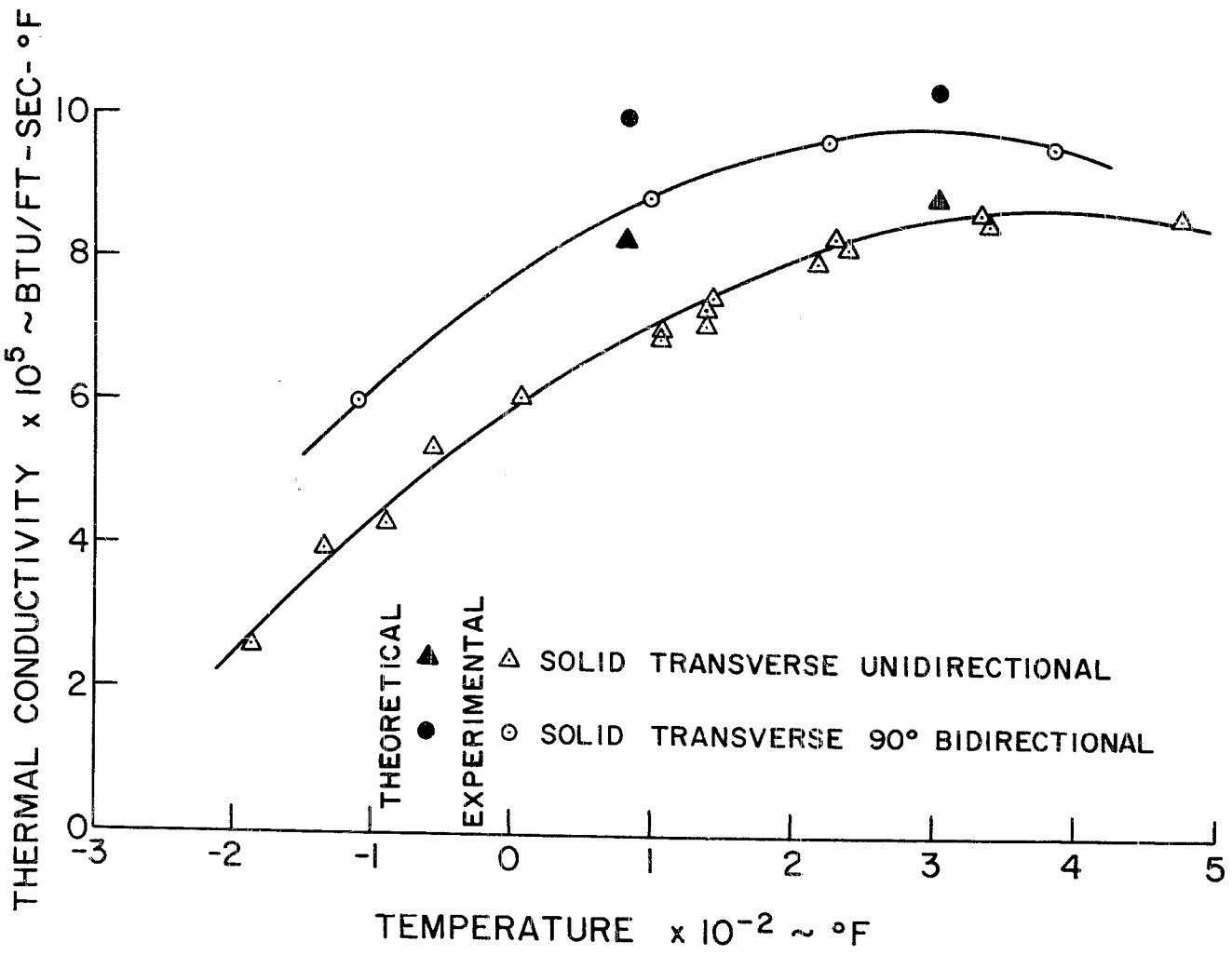

Figure 26. Thermal Conductivity of Solid Glass Epon 828 Composite

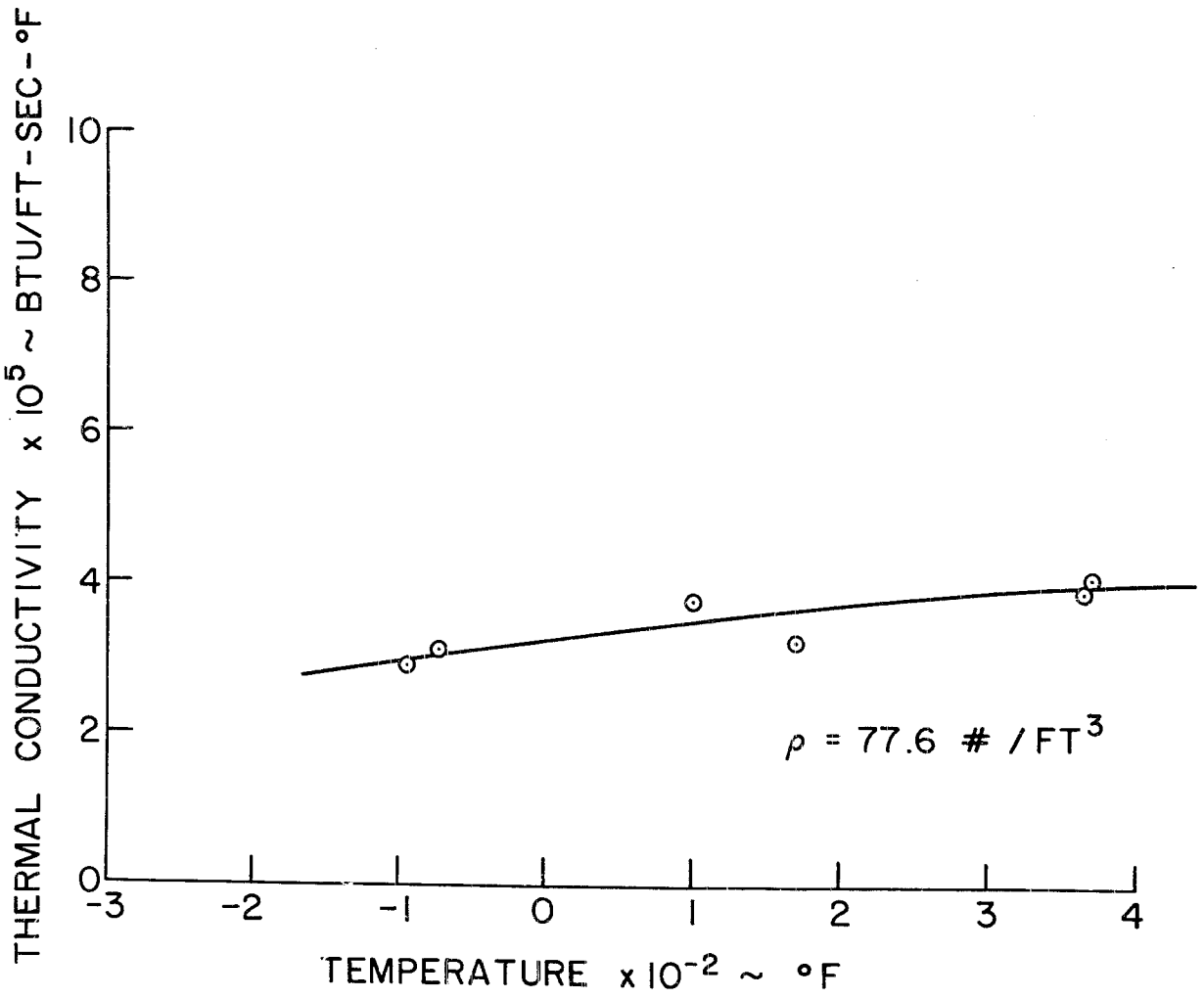

Figure 27. Thermal Conductivity of Shell Epon 828

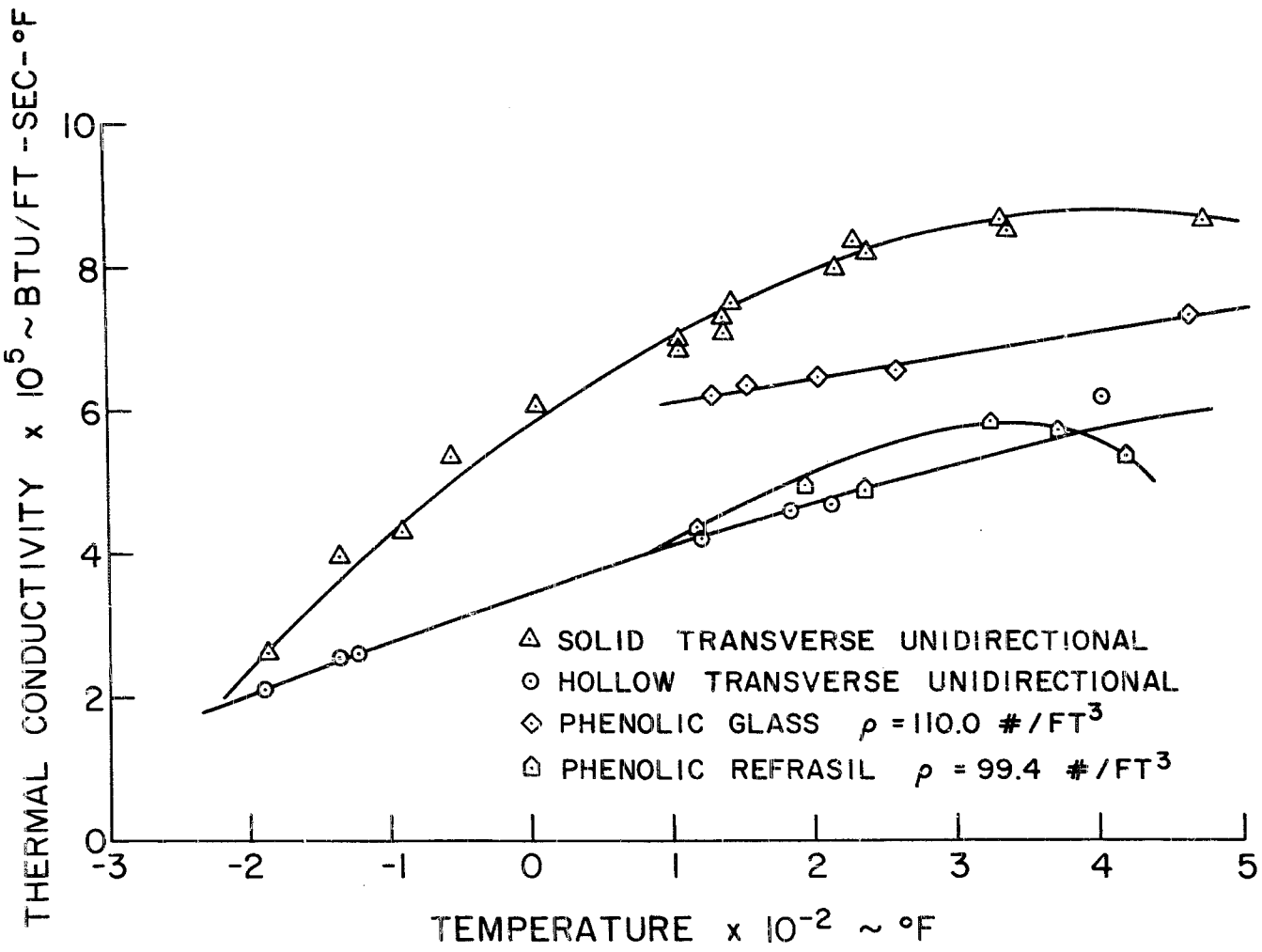

Figure 28. Comparative Thermal Conductivity

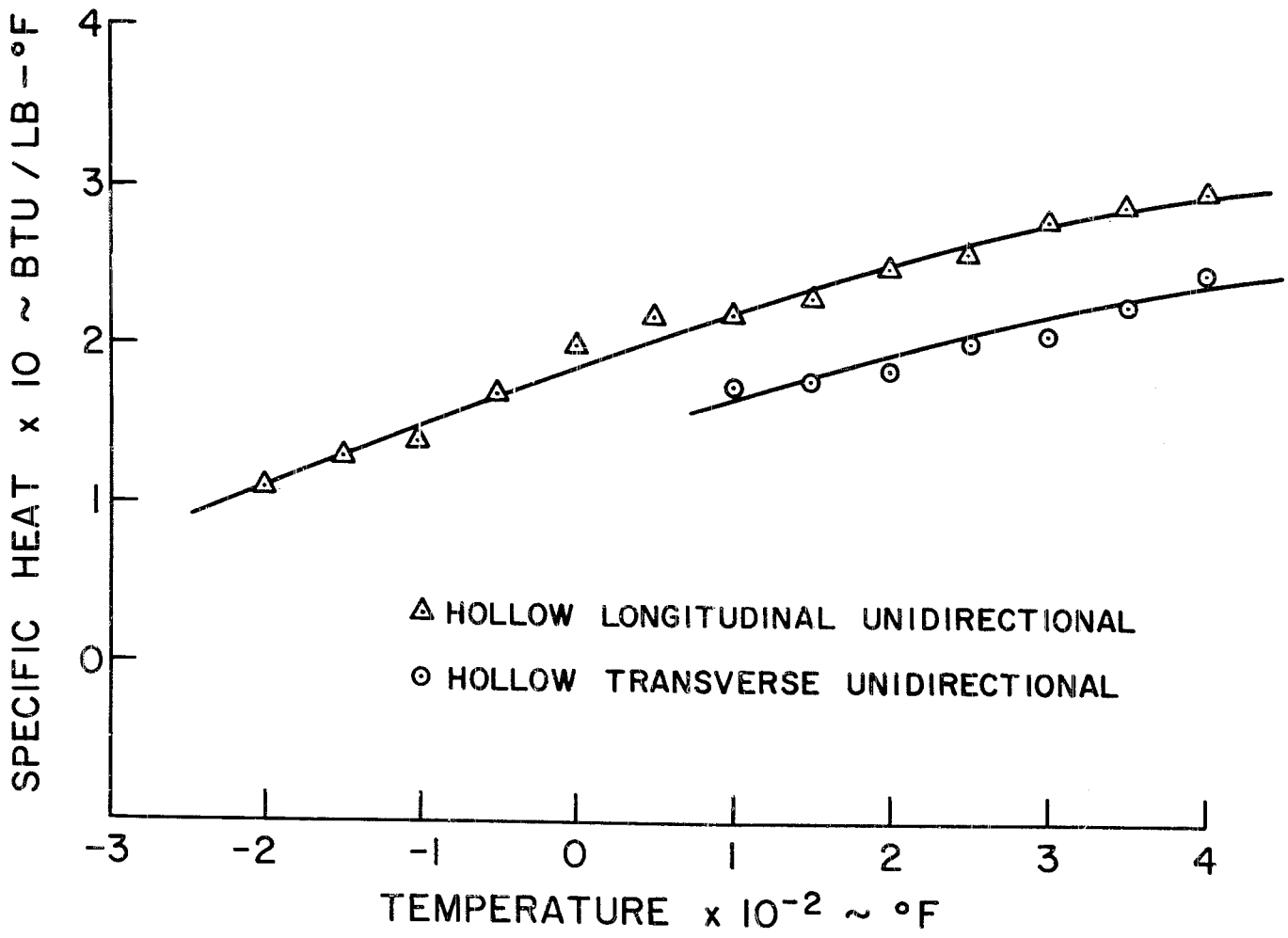

Figure 29. Specific Heat of Hollow Glass Epon 828 Composite

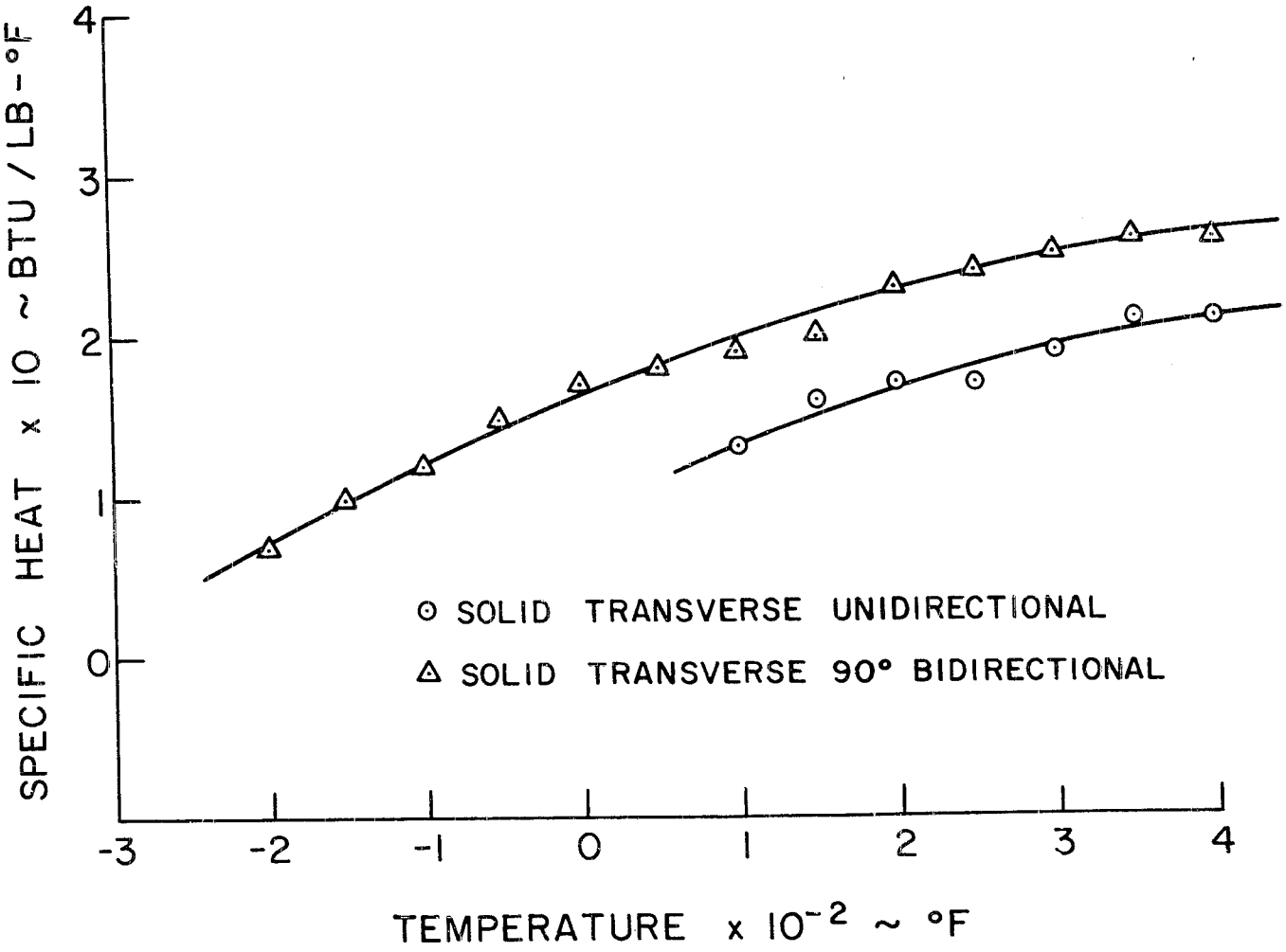

Figure 30. Specific Heat of Solid Glass Epon 828 Composite

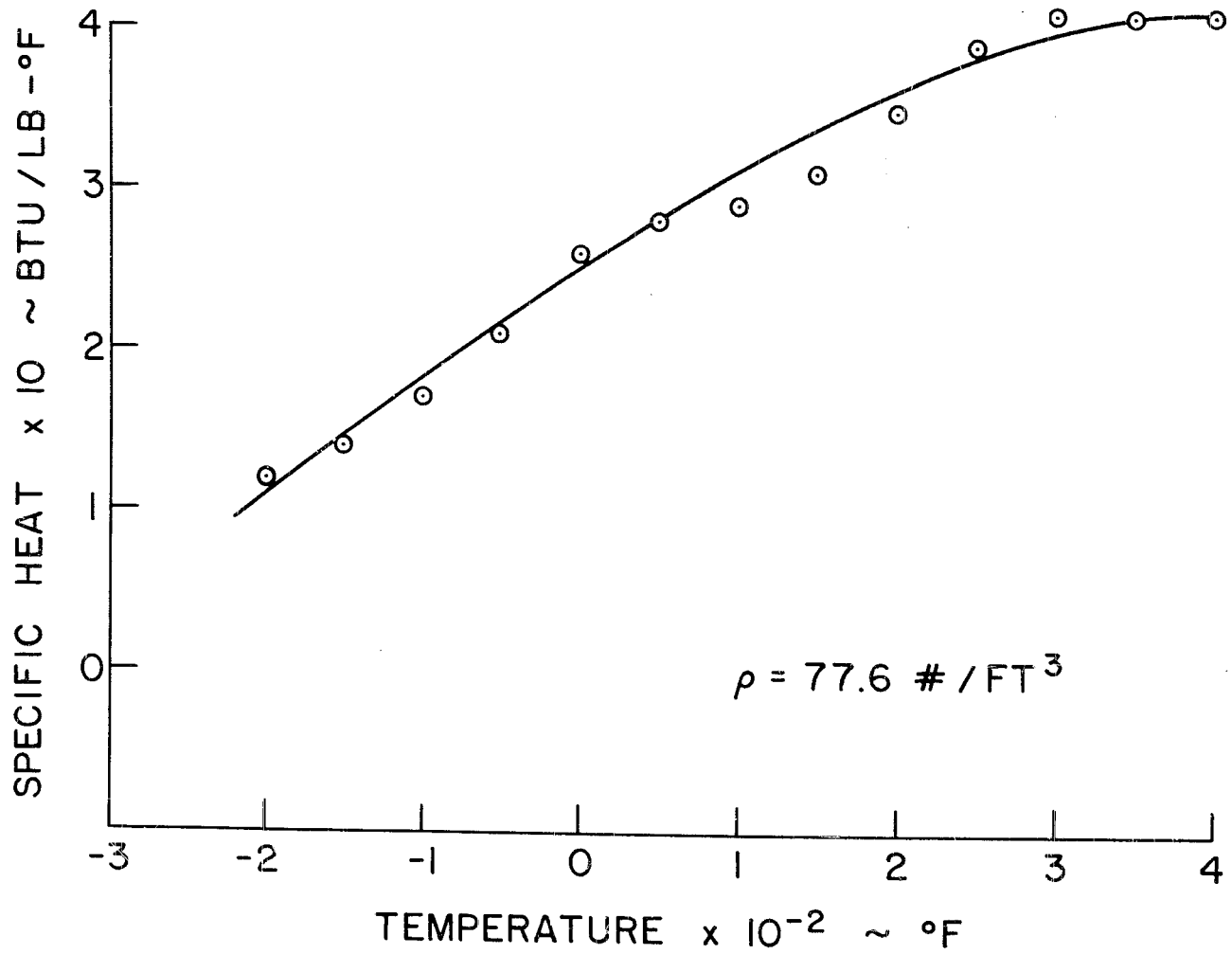

Figure 31. Specific Heat of Shell Epon 828

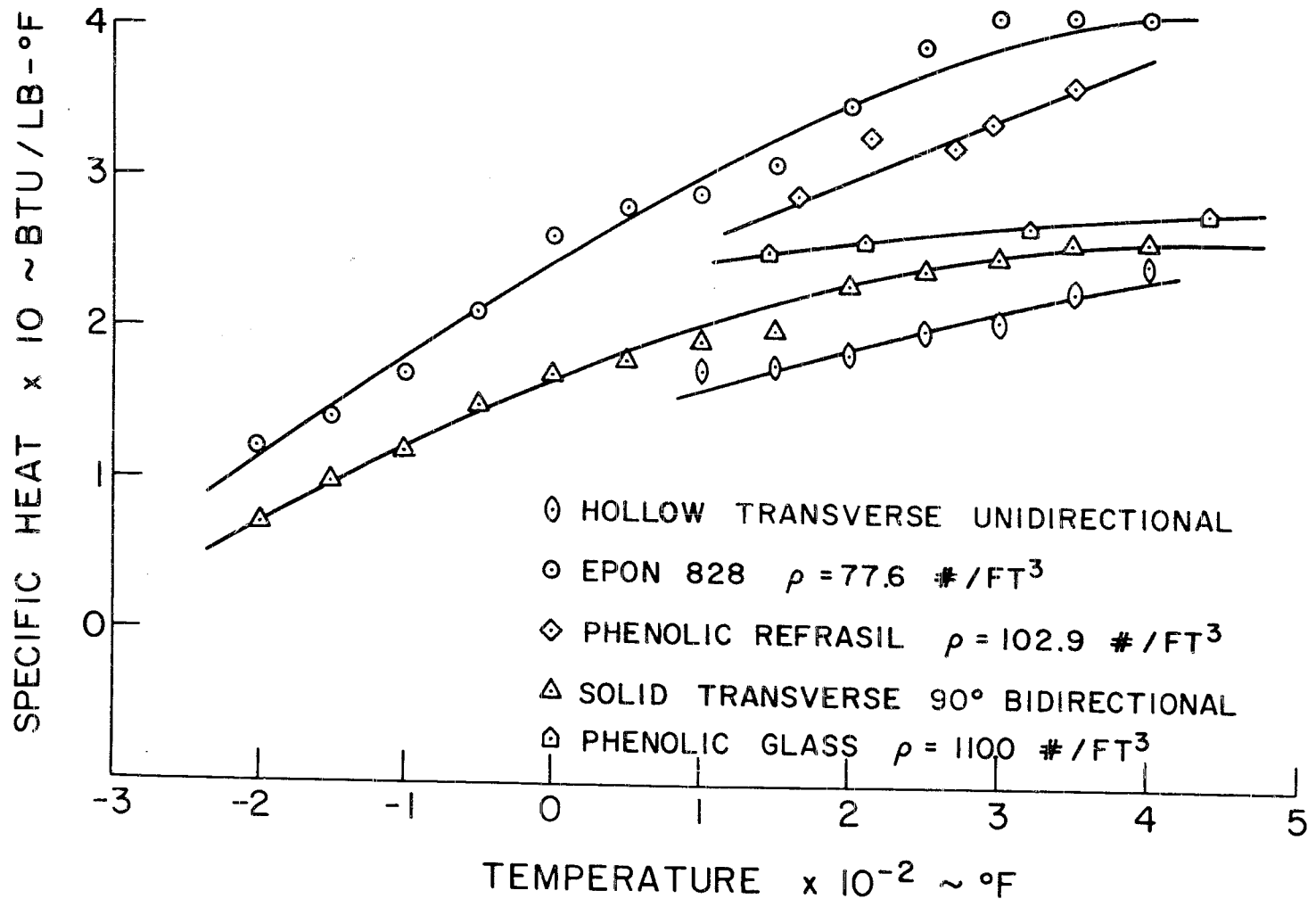

Figure 32. Comparative Specific Heat

	TRANSVERSE UNIDIRECTIONAL	TRANSVERSE 60°/90° BIDIRECTIONAL	LONGITUDINAL
HOLLOW FIBERS	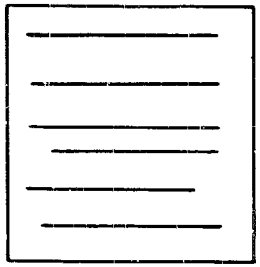 RESIN CONTENT = 35.3%	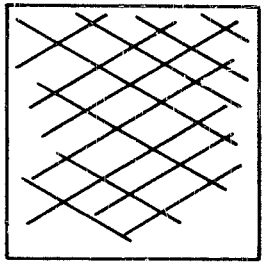 RESIN CONTENT = 37.4%	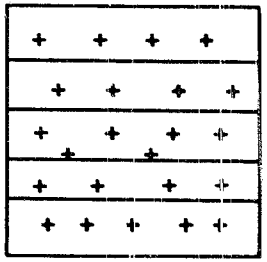 RESIN CONTENT = 35.3%
SOLID FIBERS	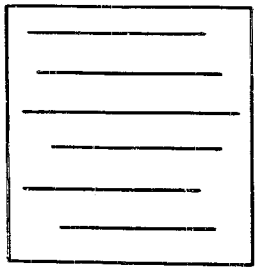 RESIN CONTENT = 22.4%	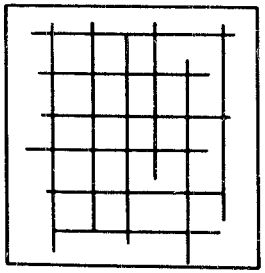 RESIN CONTENT = 23.4%	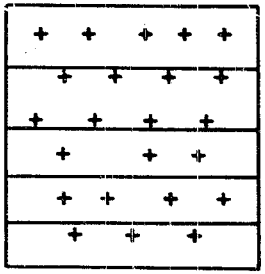 RESIN CONTENT = 22.4%

Figure 33. Thermal Conductivity and Expansion Test Specimen Configurations

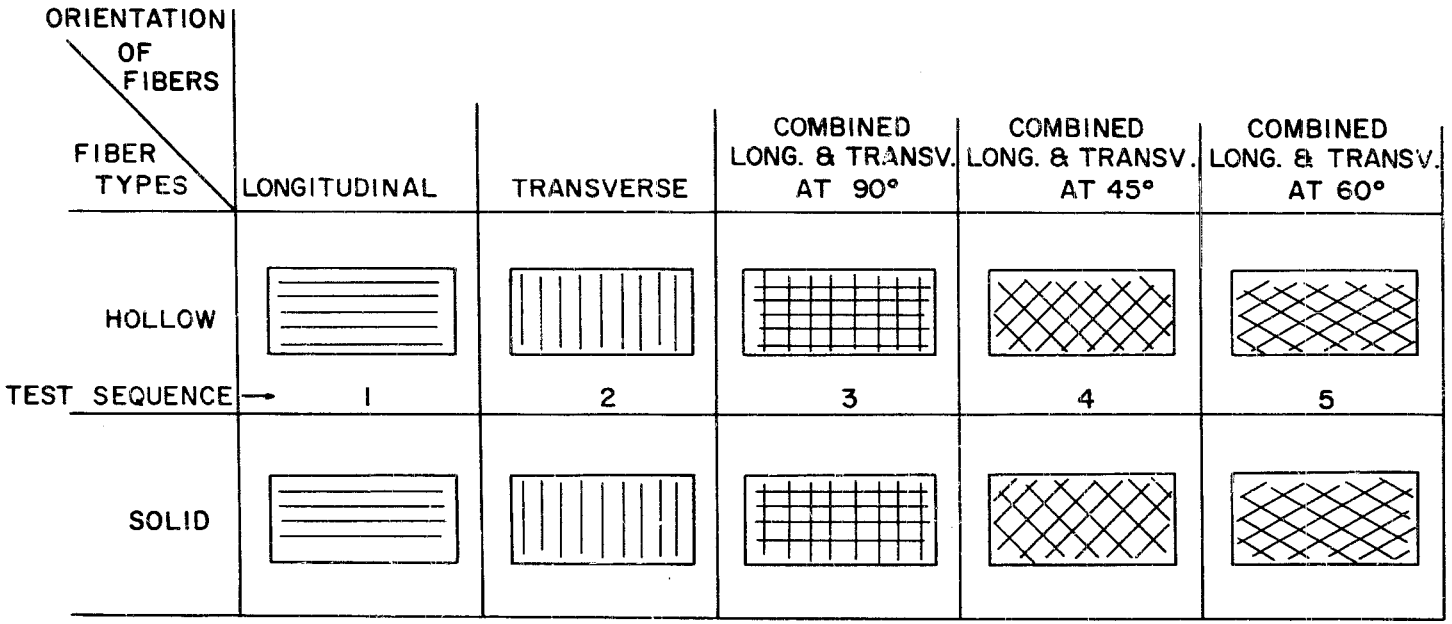

Figure 34. Thermal Expansion Test Specimen Configurations

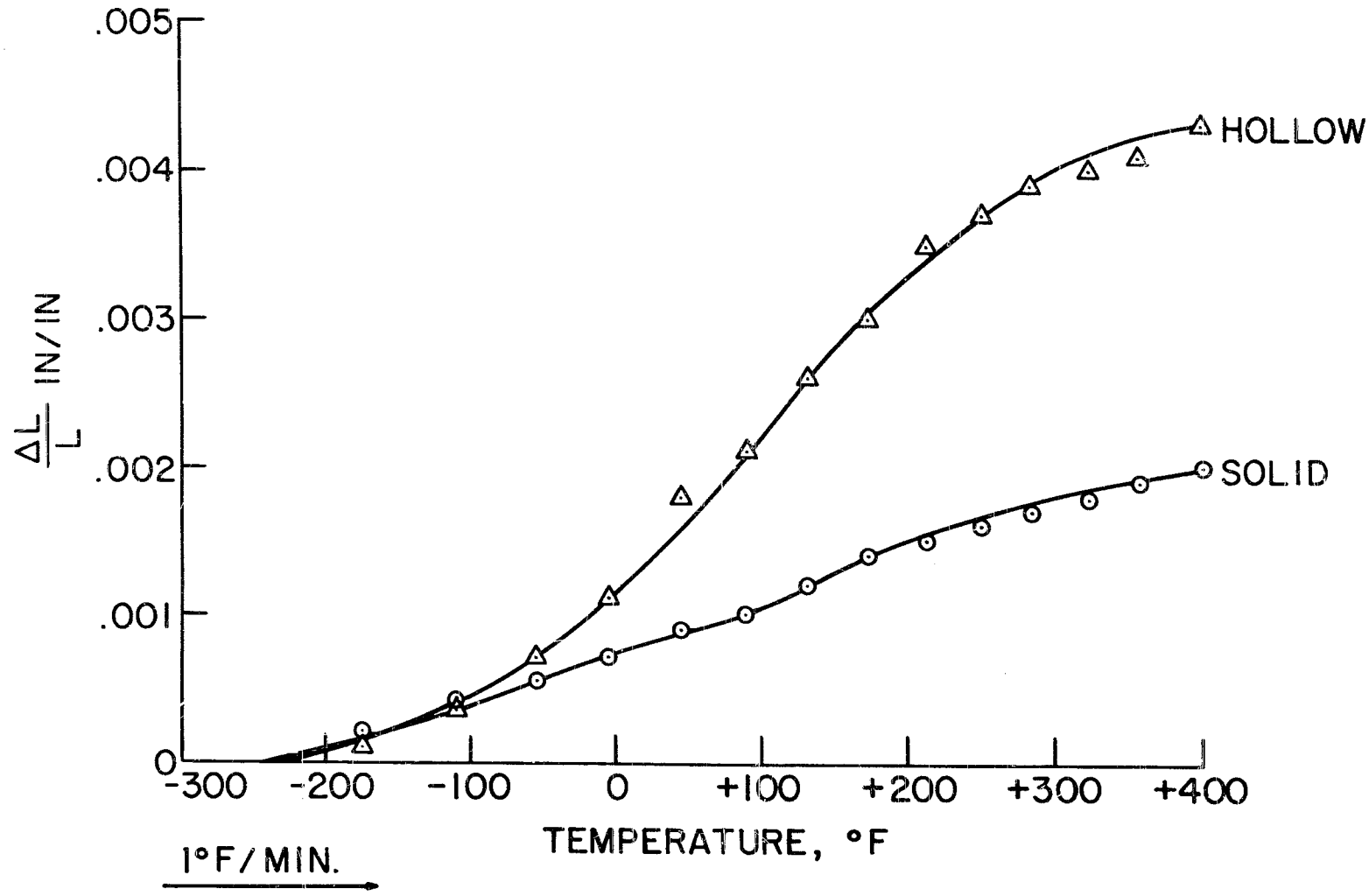

Figure 35. Thermal Expansion of Longitudinal Specimens

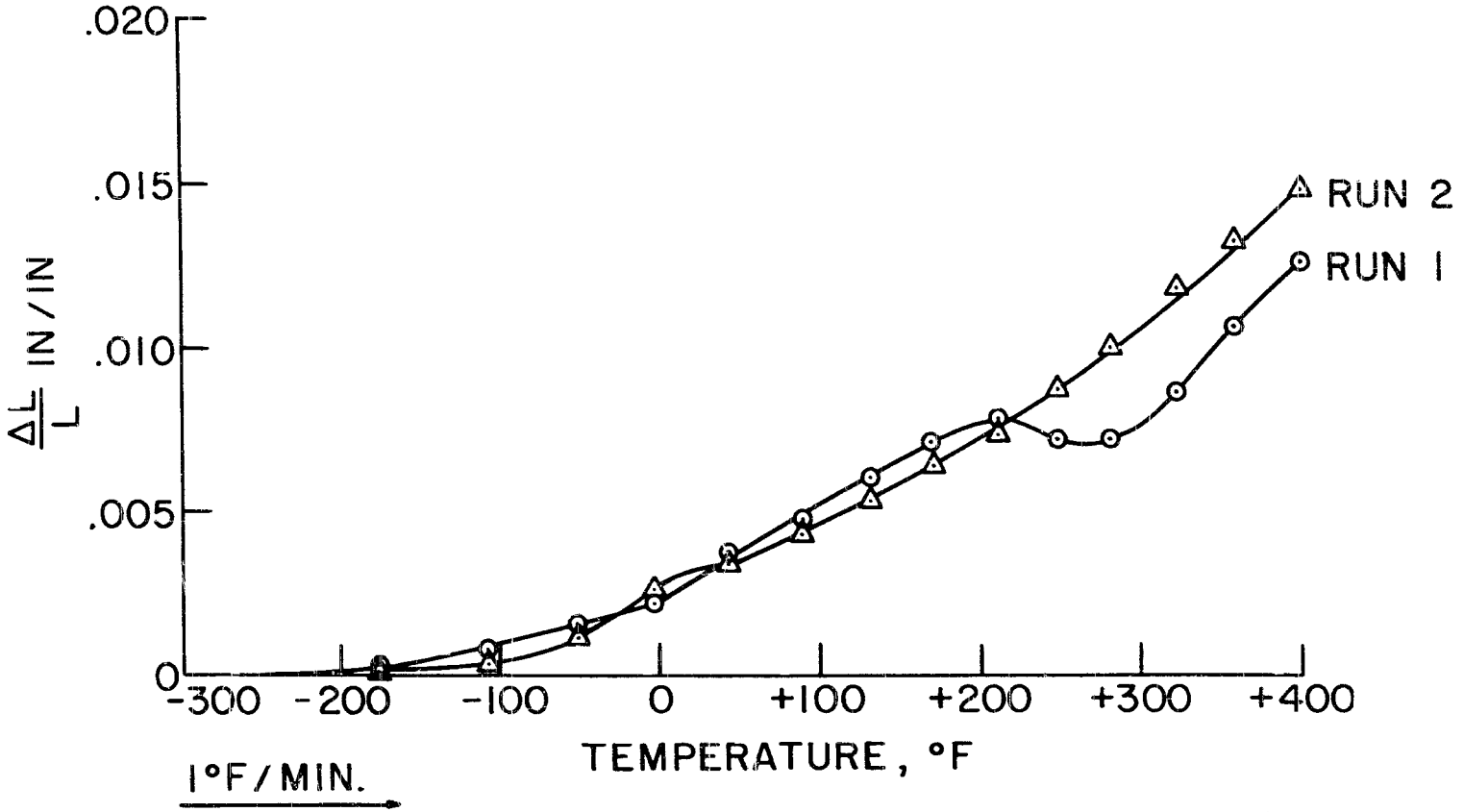

Figure 36. Thermal Expansion of Transverse Hollow Specimens

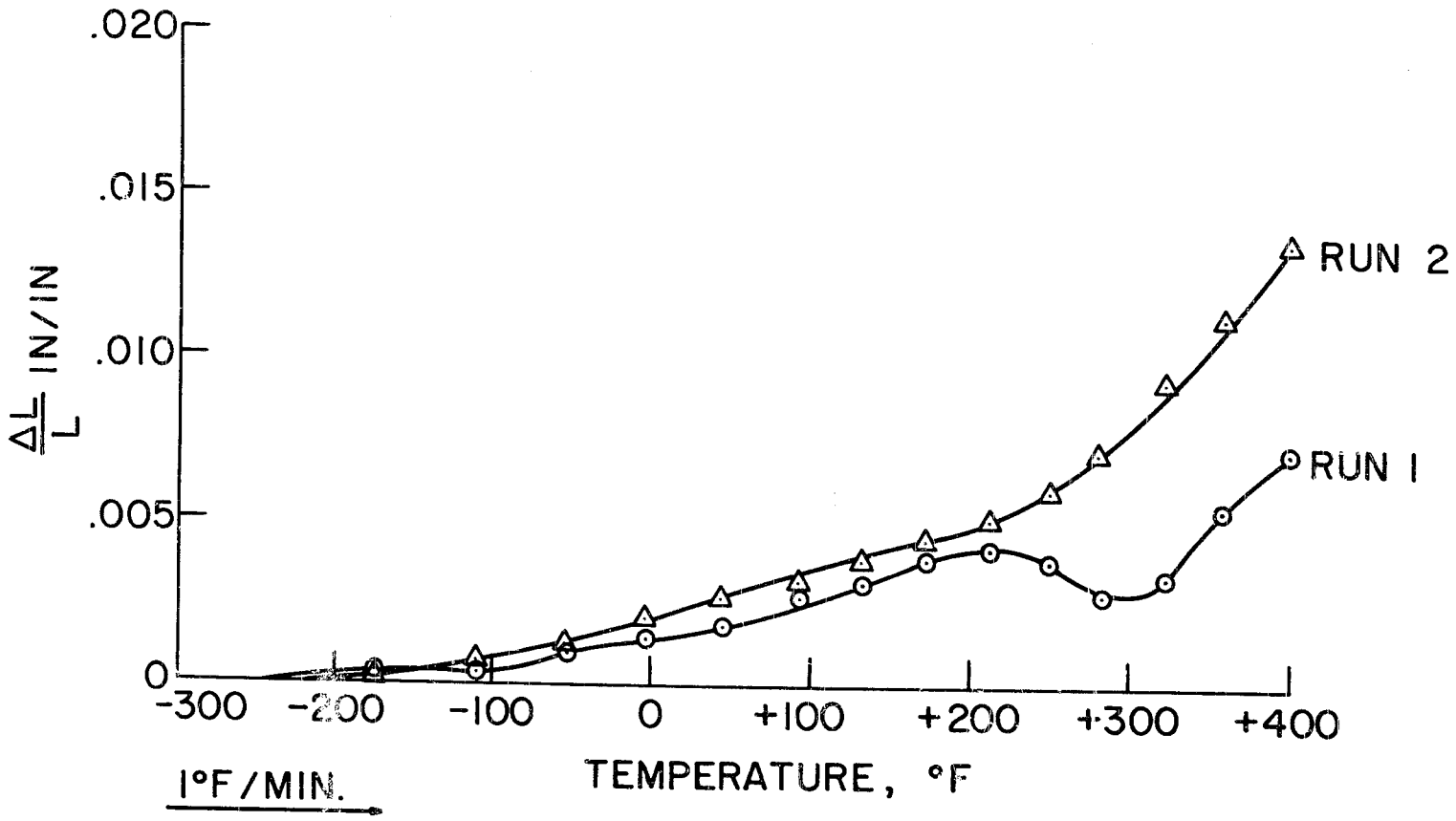

Figure 37. Thermal Expansion of Transverse Solid Specimens

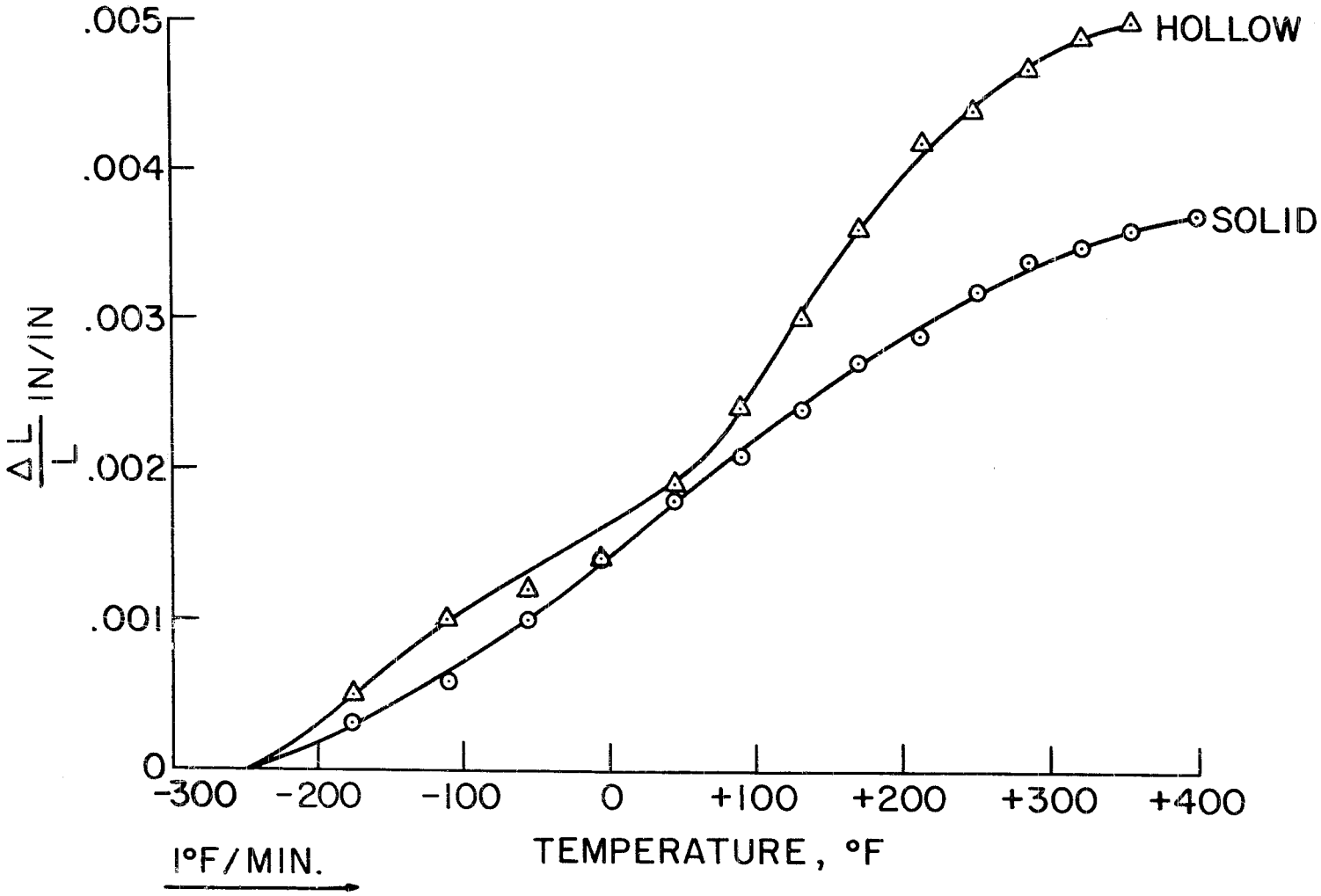

Figure 38. Thermal Expansion of 90° Combination Specimen

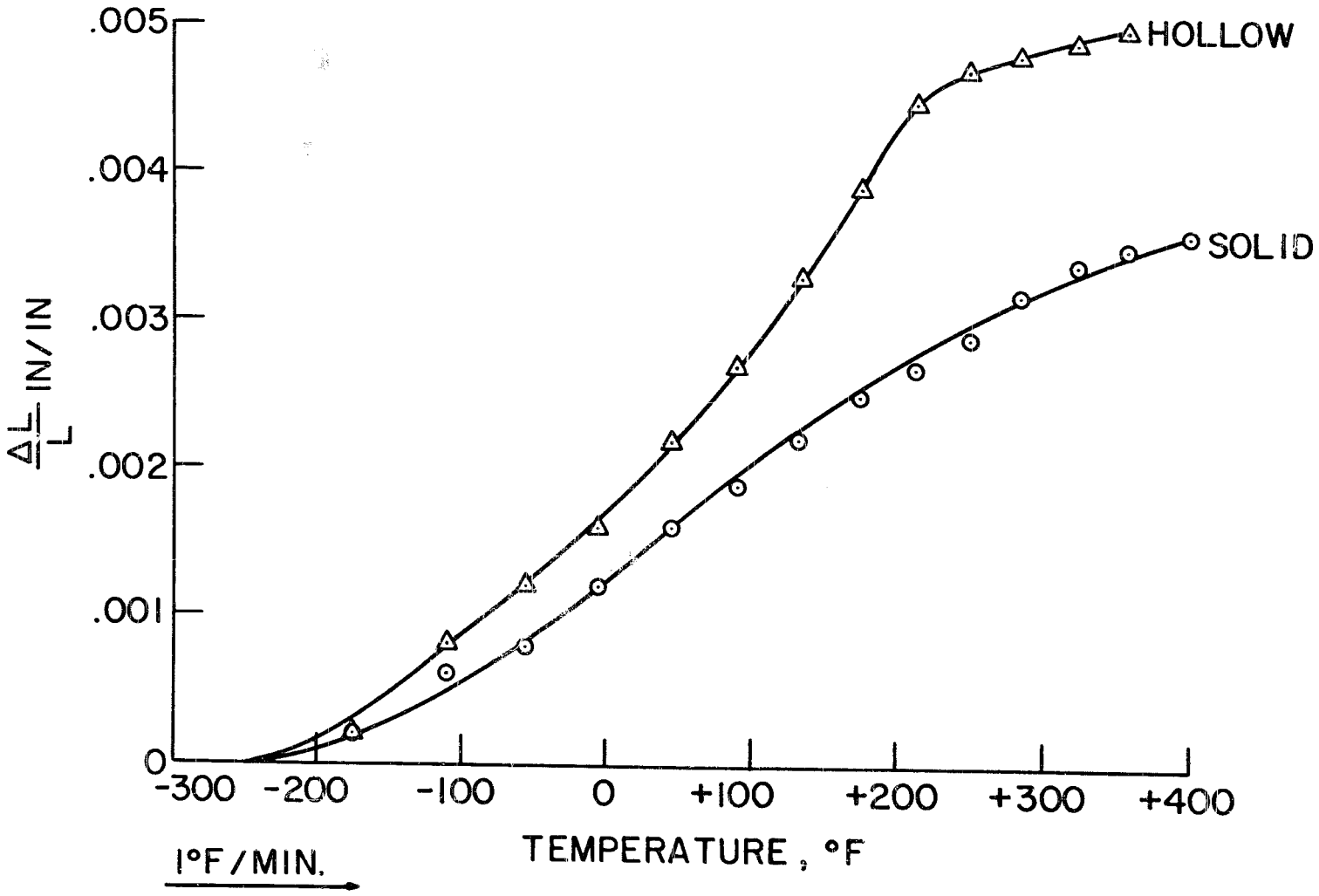

Figure 39. Thermal Expansion of 45° Combination Material

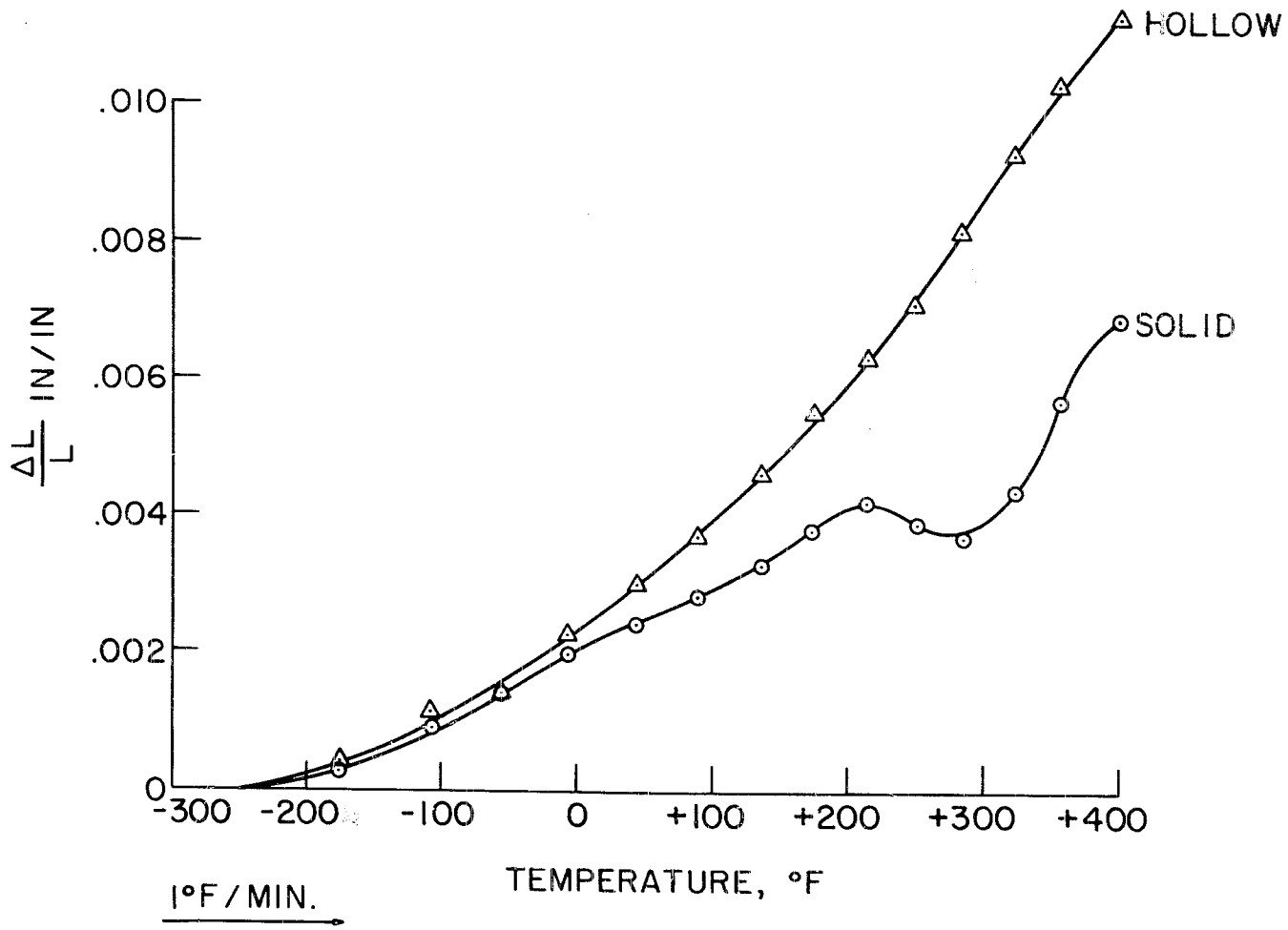

Figure 40. Thermal Expansion of 60° Combination Specimen

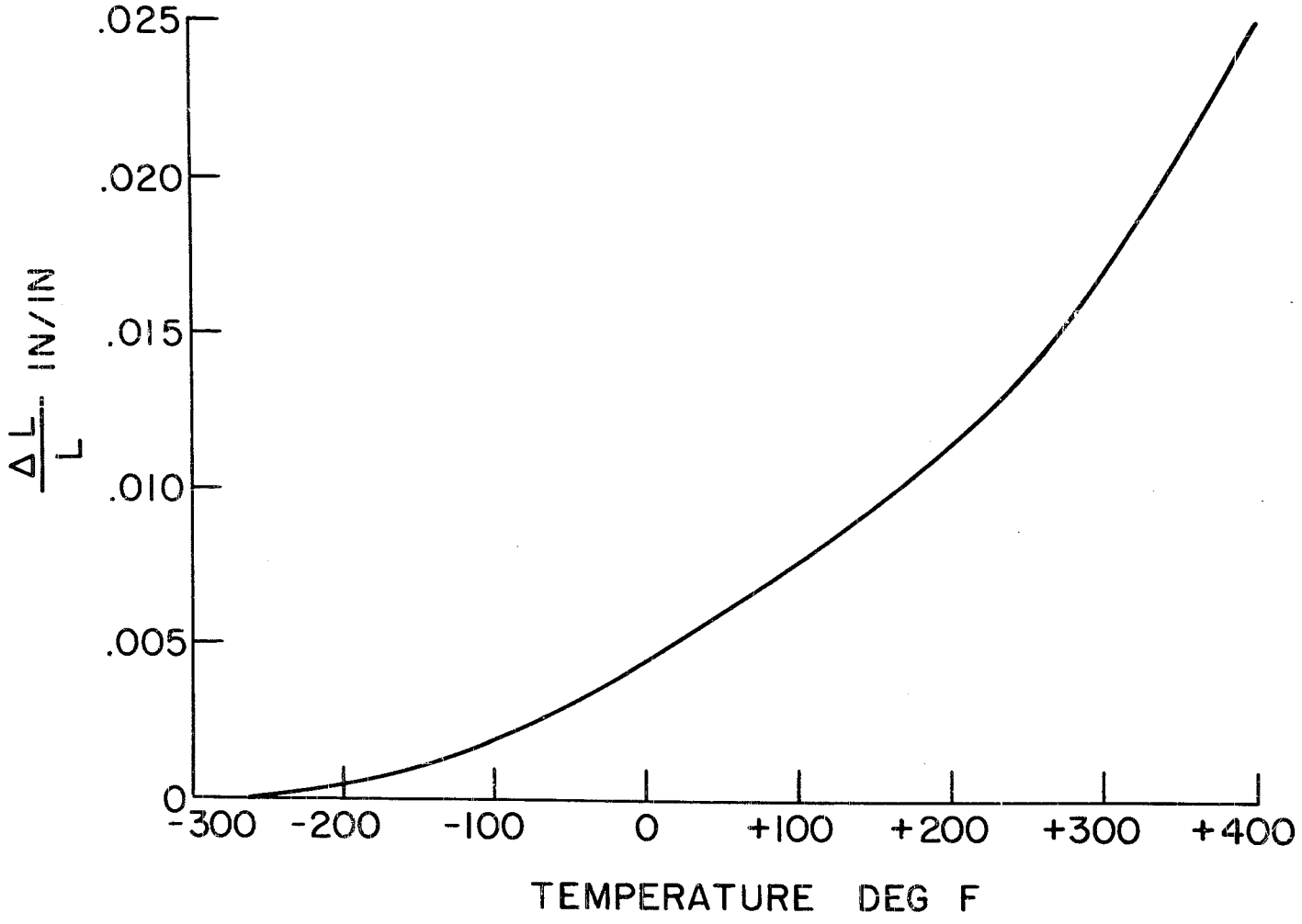

Figure 41. Thermal Expansion of Epon 828 System

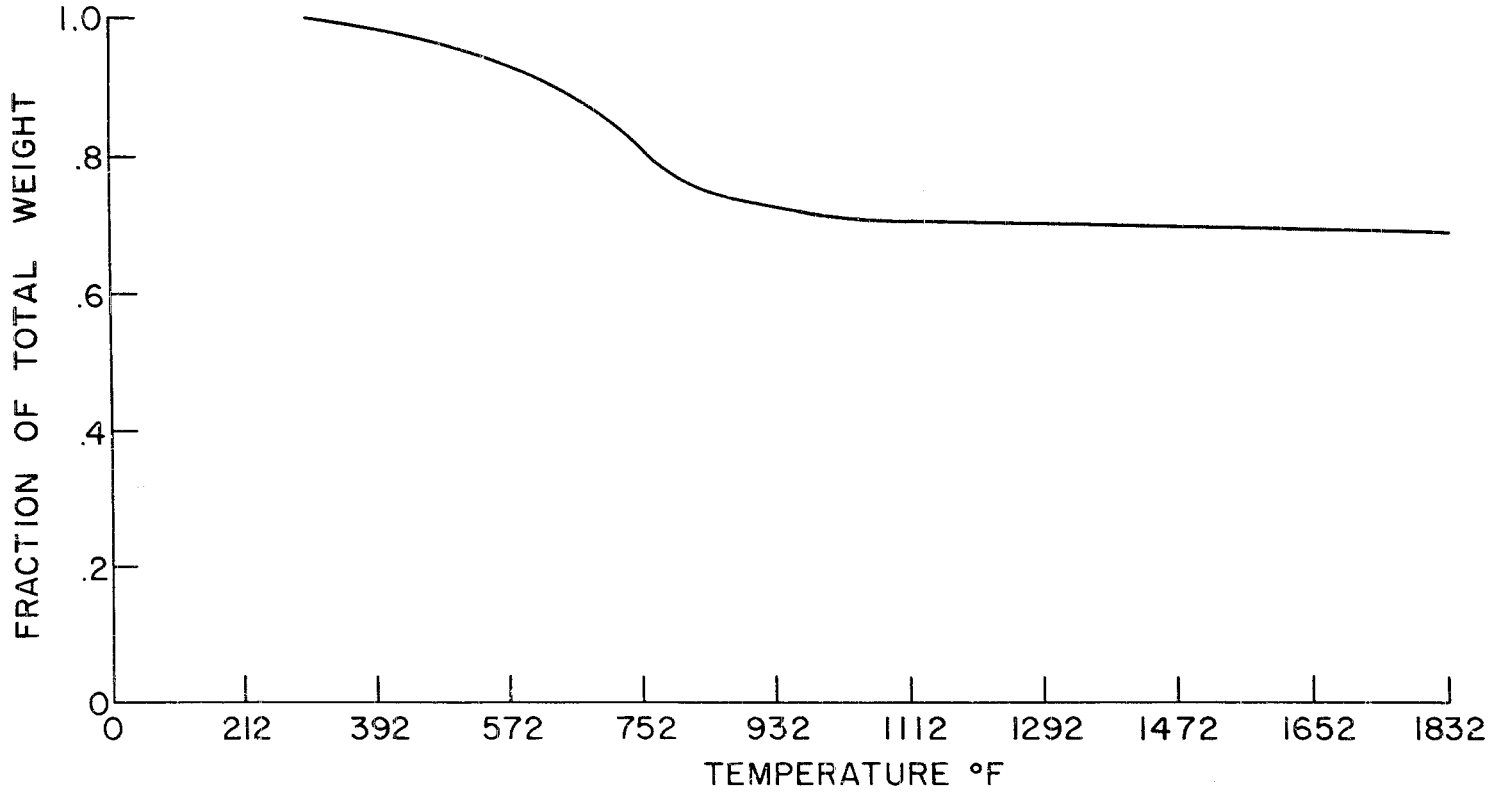

Figure 42. Thermo-Gravimetric Analysis Results

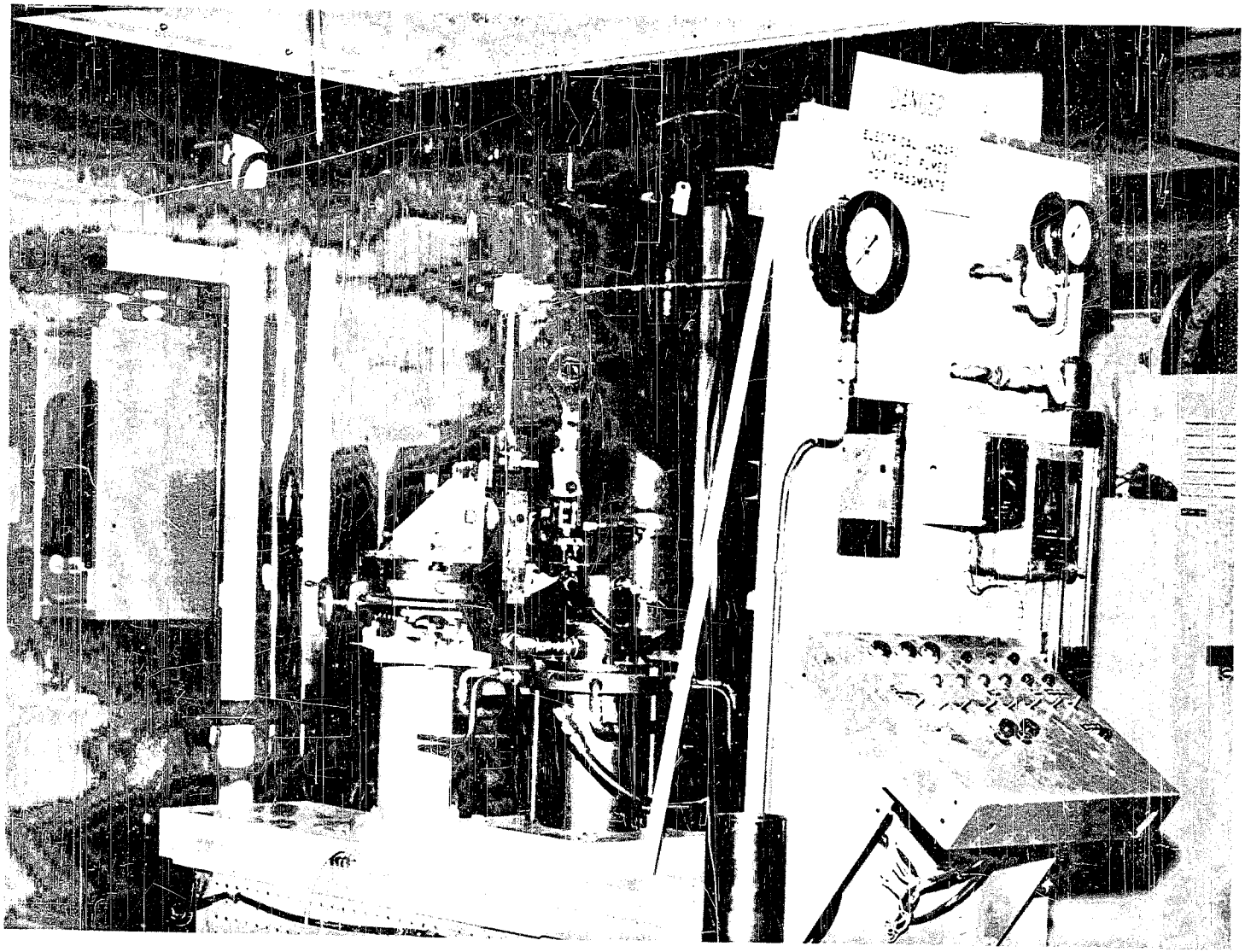

Figure 43. Shroud Nozzle Air Arc Facility

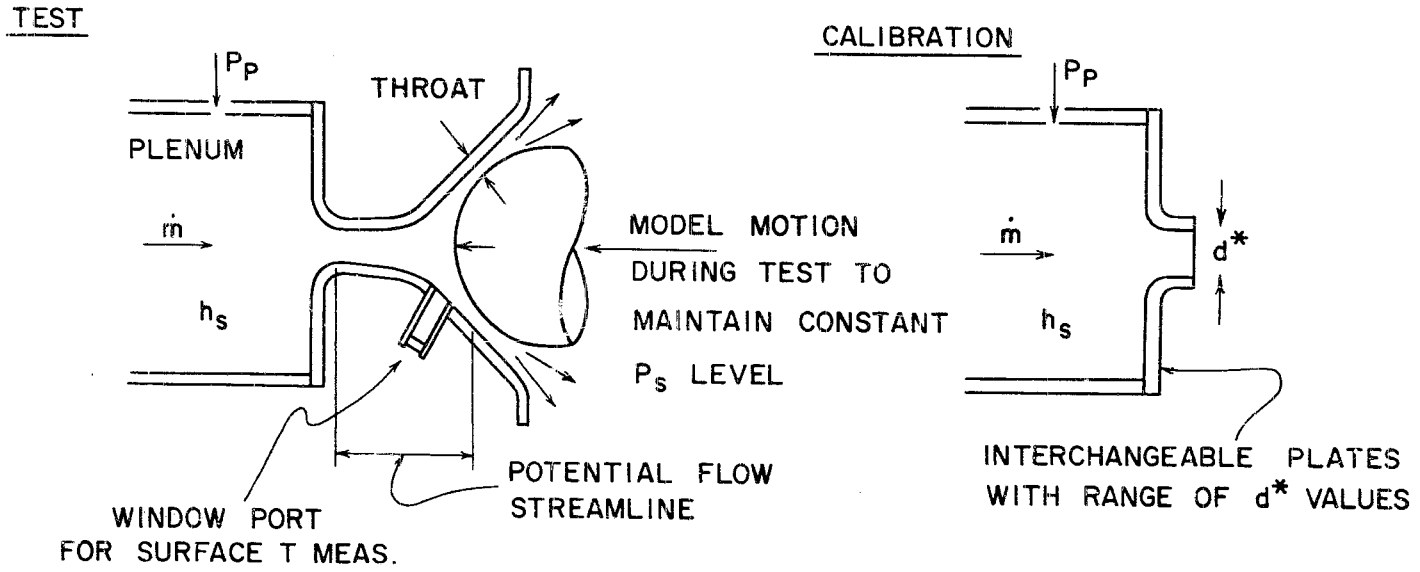

TYPICAL TEST MEASUREMENT

MODEL

1. SURFACE TEMPERATURE
2. SUB-SURFACE AND BACKWALL TEMPERATURE
3. SURFACE PRESSURE
4. SURFACE HEAT TRANSFER RATES - NON-ABLATING
5. ABLATION RATE-LOCAL AND TOTAL

FACILTY AND CALIBRATION

1. VOLTAGE
2. CURRENT
3. ELECTRODE EROSION RATE (IF APPROPRIATE)
4. AIR MASS FLOW RATE
5. PLENUM PRESSURE
6. GAS TEMPERATURE - THROAT
7. GAS TEMPERATURE - PLENUM

Figure 44. Characteristics of Shroud Nozzle Air Arc Test Facility

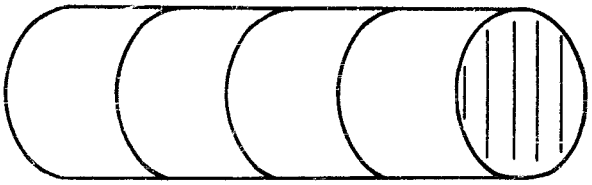

REINFORCING FIBER TYPE	SPECIMEN NUMBERS
SOLID	3 & 4
HOLLOW	7 & 8

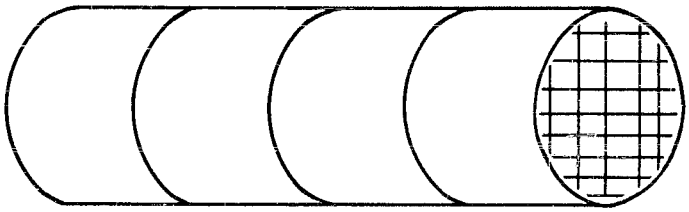

SOLID	5 & 6
HOLLOW	1 & 2

Figure 45. Ablation Specimens

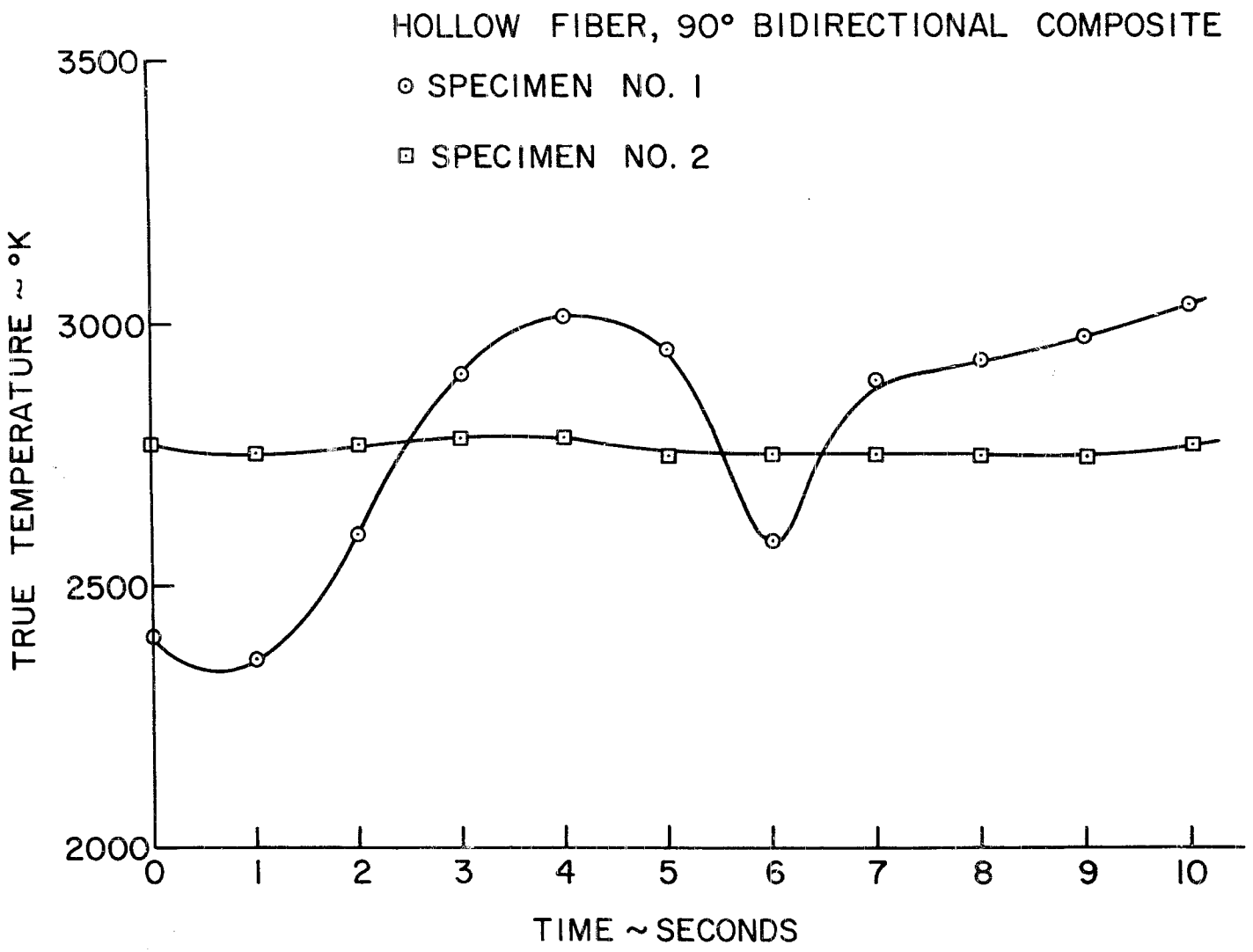

Figure 46. Ablation Specimen Surface Temperature - Hollow Fiber, 90° Bidirectional Composite

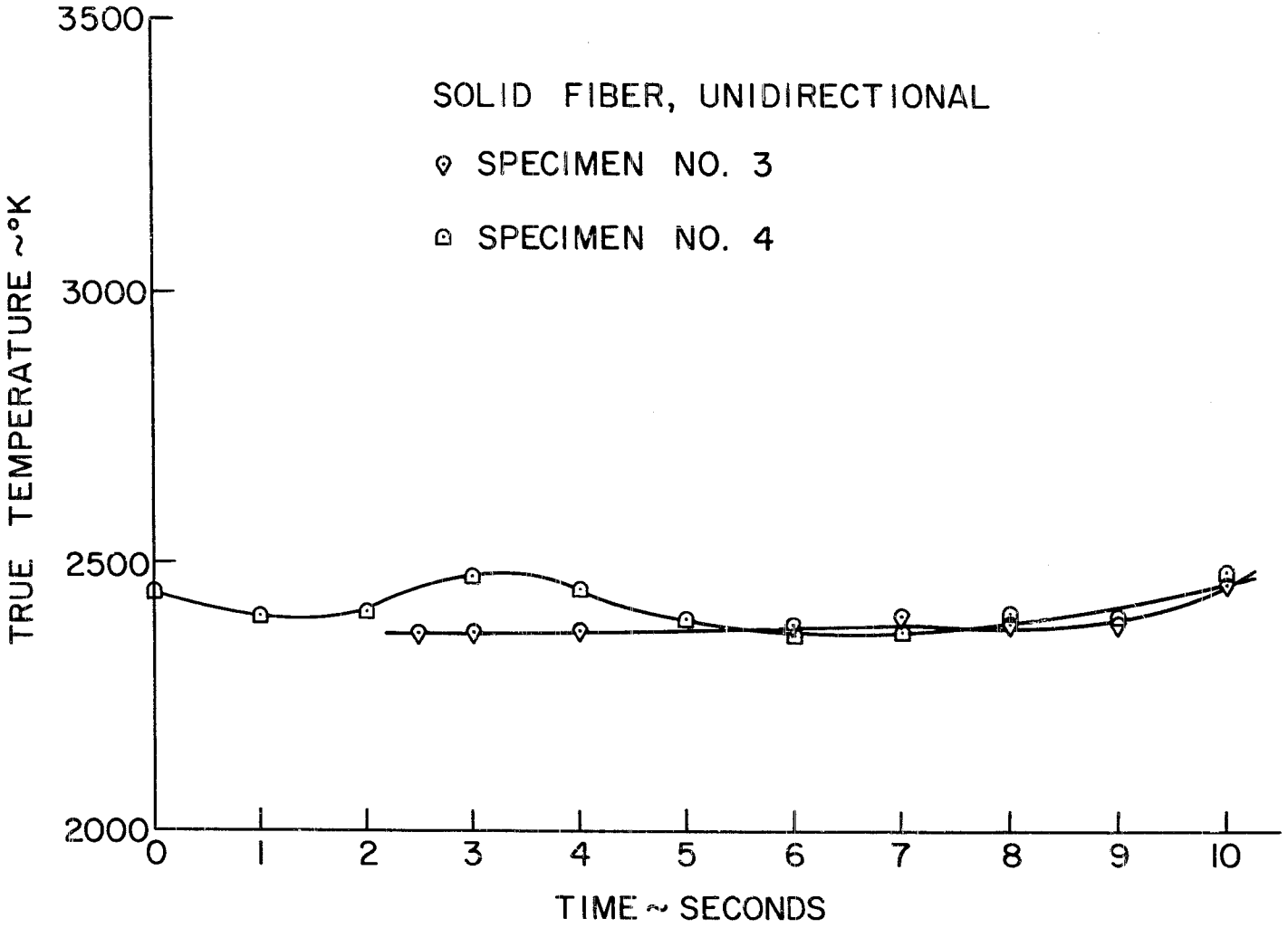

Figure 47. Ablation Specimen Surface Temperature - Solid Fiber, Unidirectional

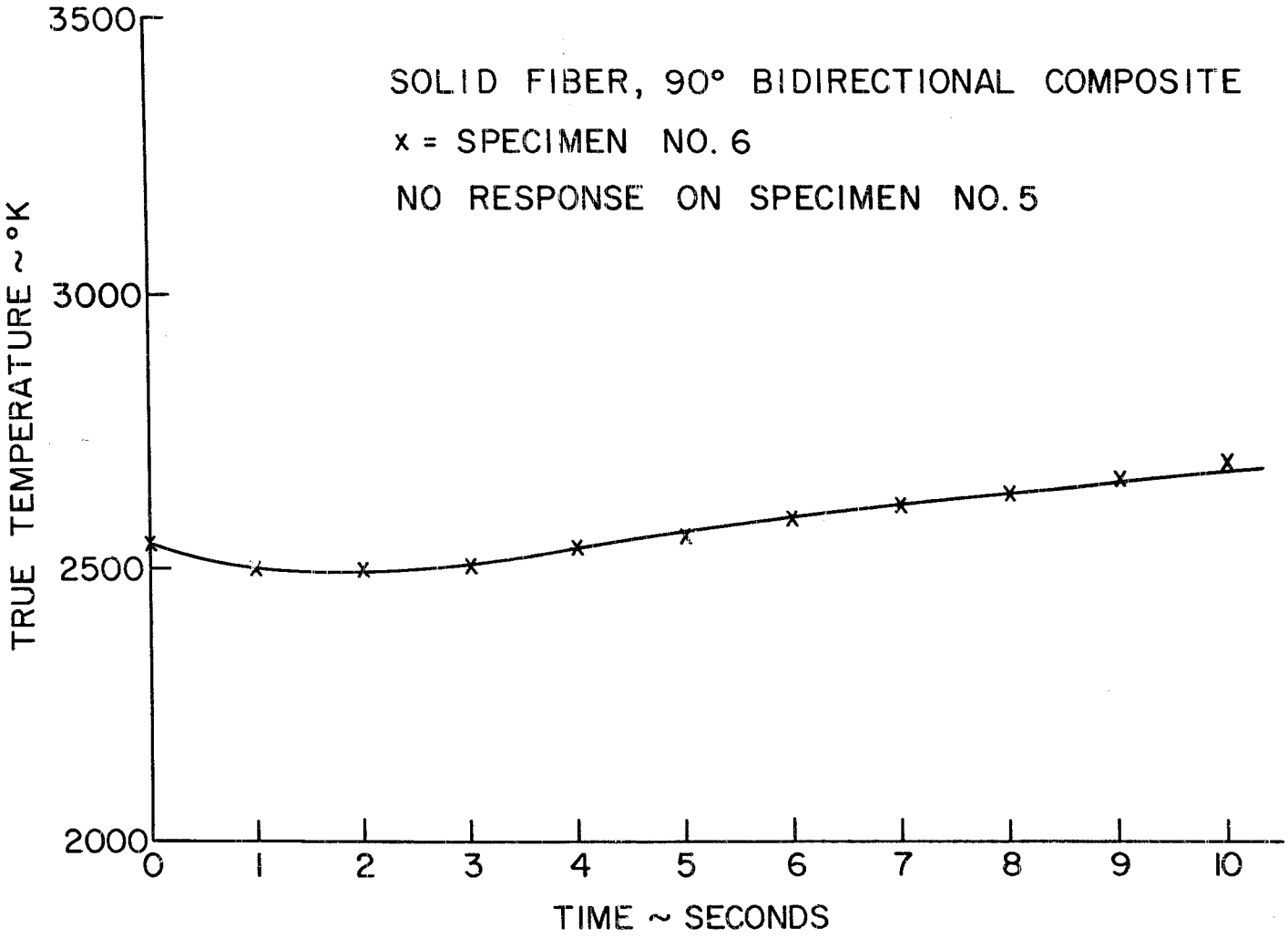

Figure 48. Ablation Specimen Surface Temperature - Solid Fiber, 90° Bidirectional Composite

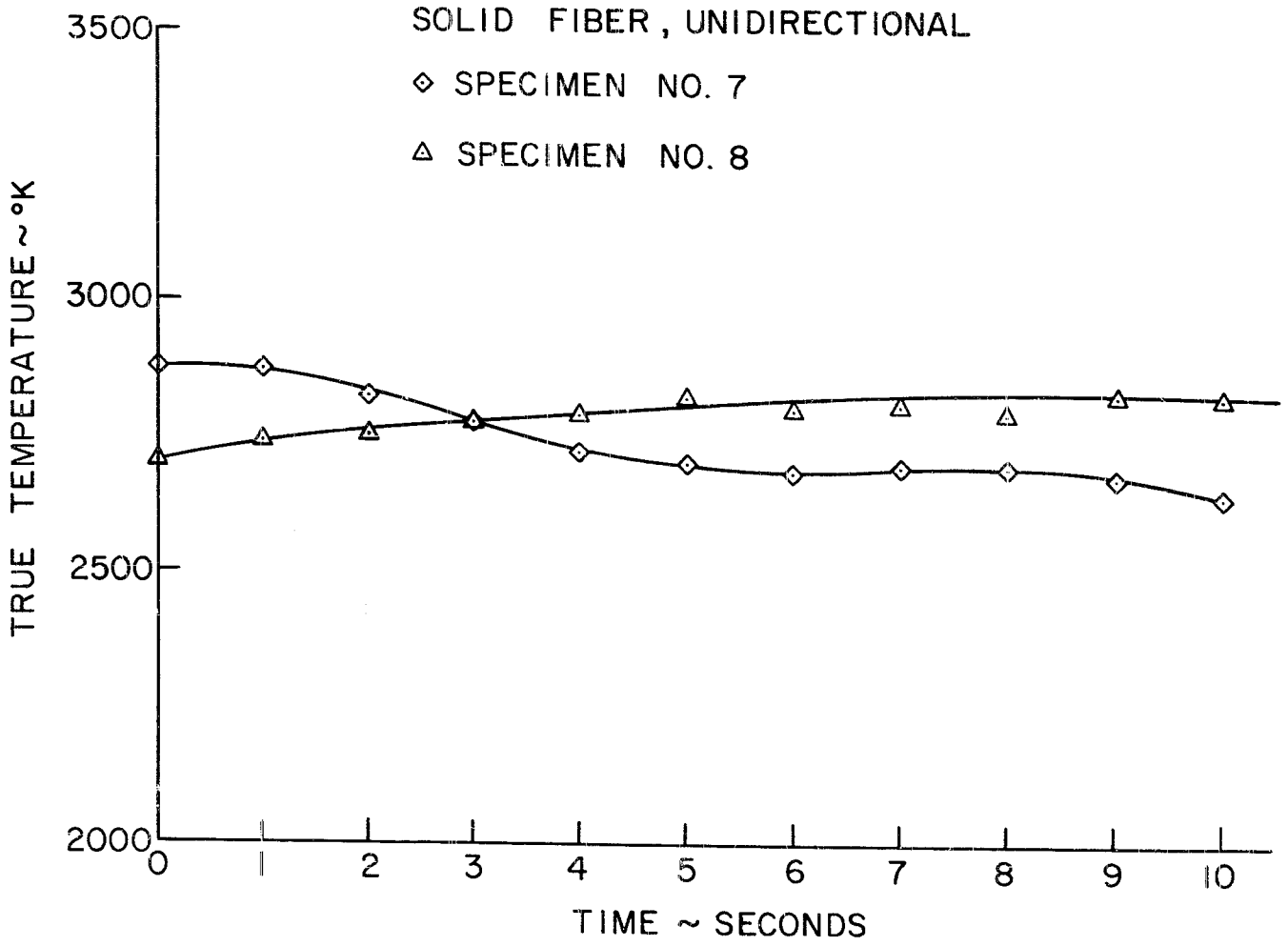

Figure 49. Ablation Specimen Surface Temperature - Solid Fiber, Unidirectional

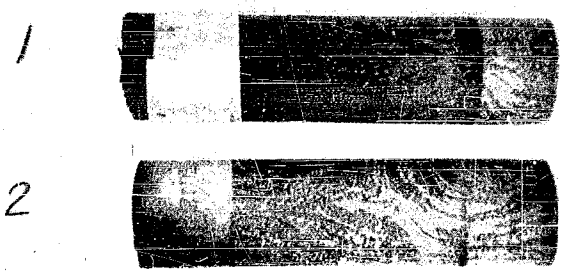

After Exposure

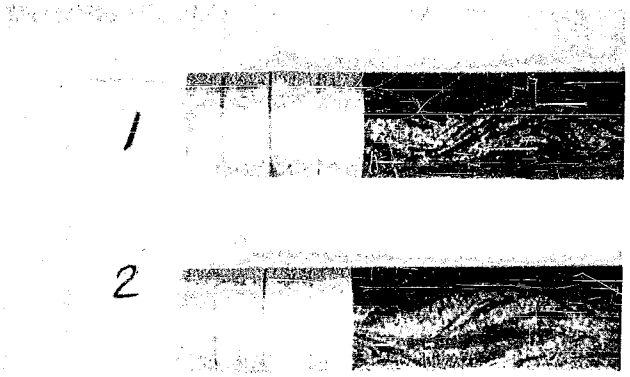

Before Exposure

Figure 50. Ablation Test Specimen - Hollow Fiber, 90° Transverse Composite

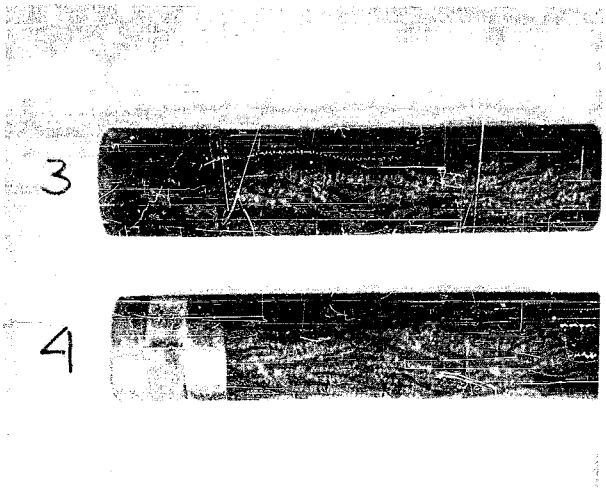

Before Exposure

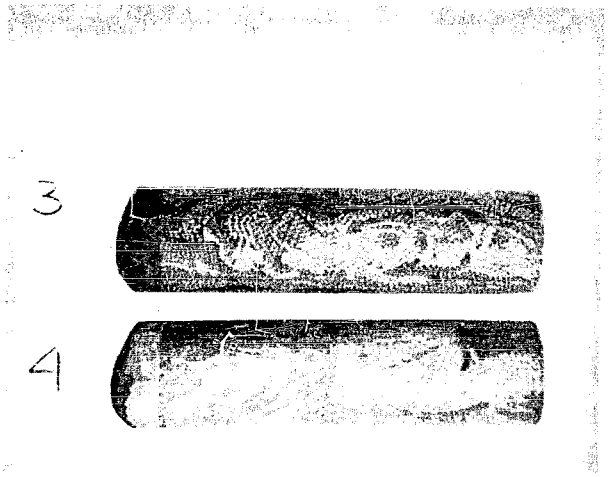

After Exposure

Figure 51. Ablation Test Specimen - Solid Fiber, Undirectional

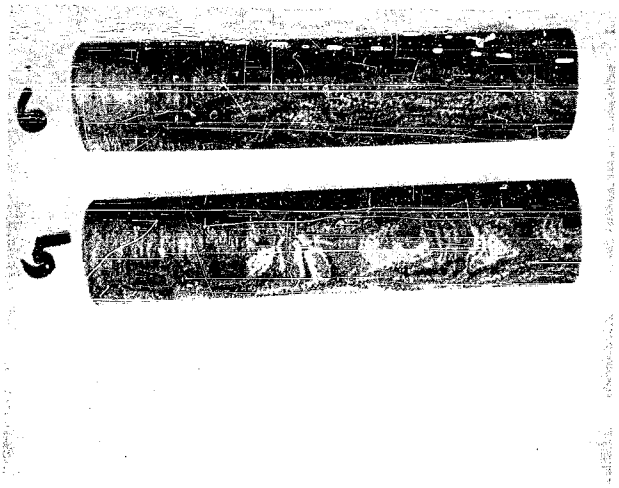

Before Exposure

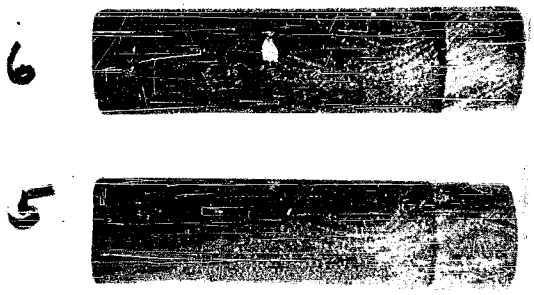

After Exposure

Figure 52. Ablation Test Specimen - Solid Fiber, 90° Transverse Composite

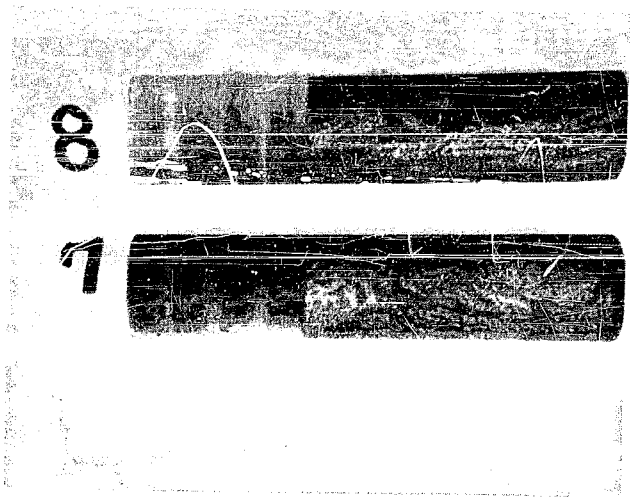

Before Exposure

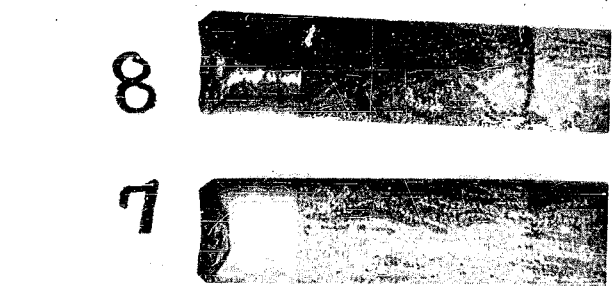

After Exposure

Figure 53. Ablation Test Specimen - Hollow Fiber, Undirectional

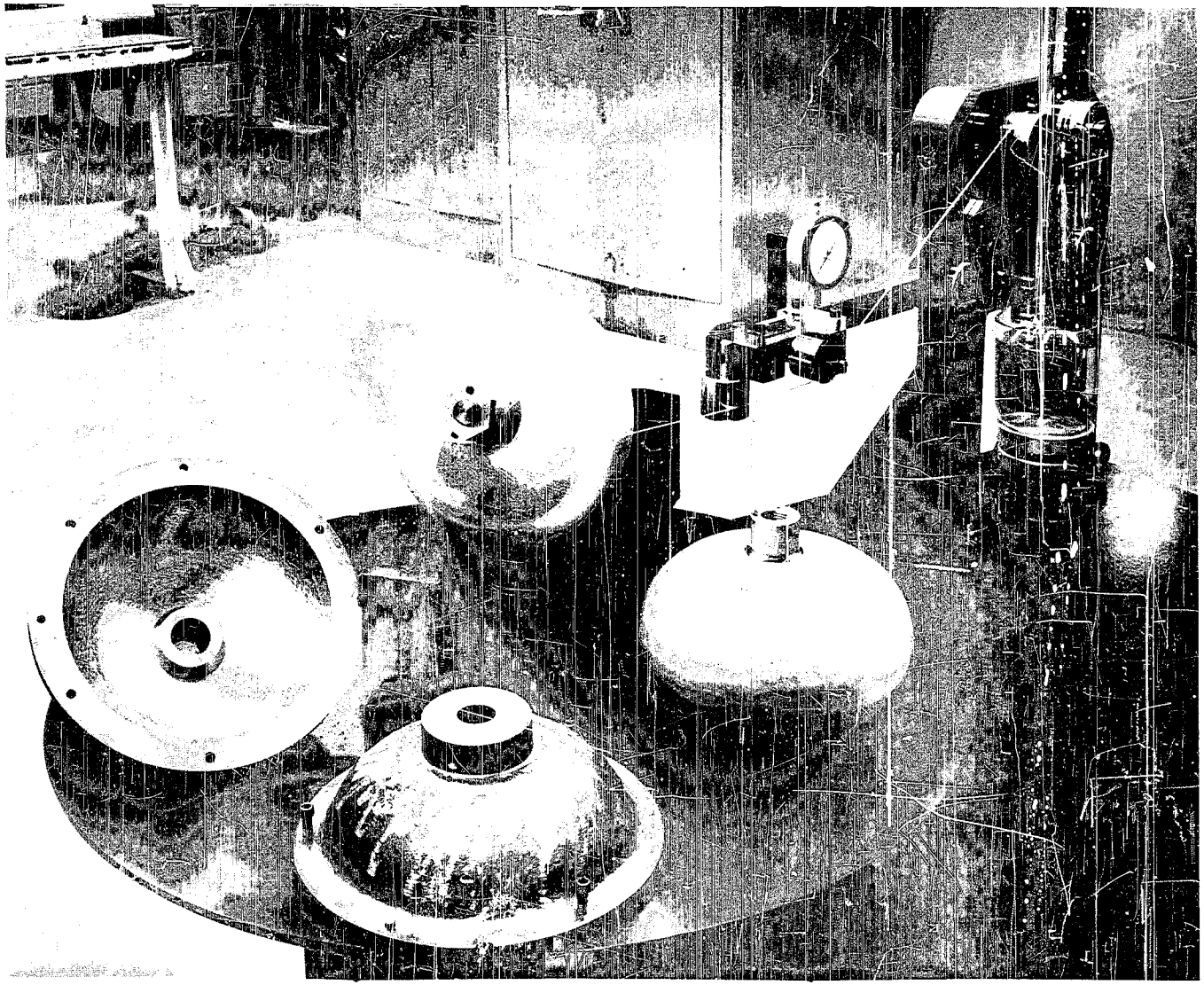

Figure 54. Isotensoid Pressure Vessel Winding Apparatus

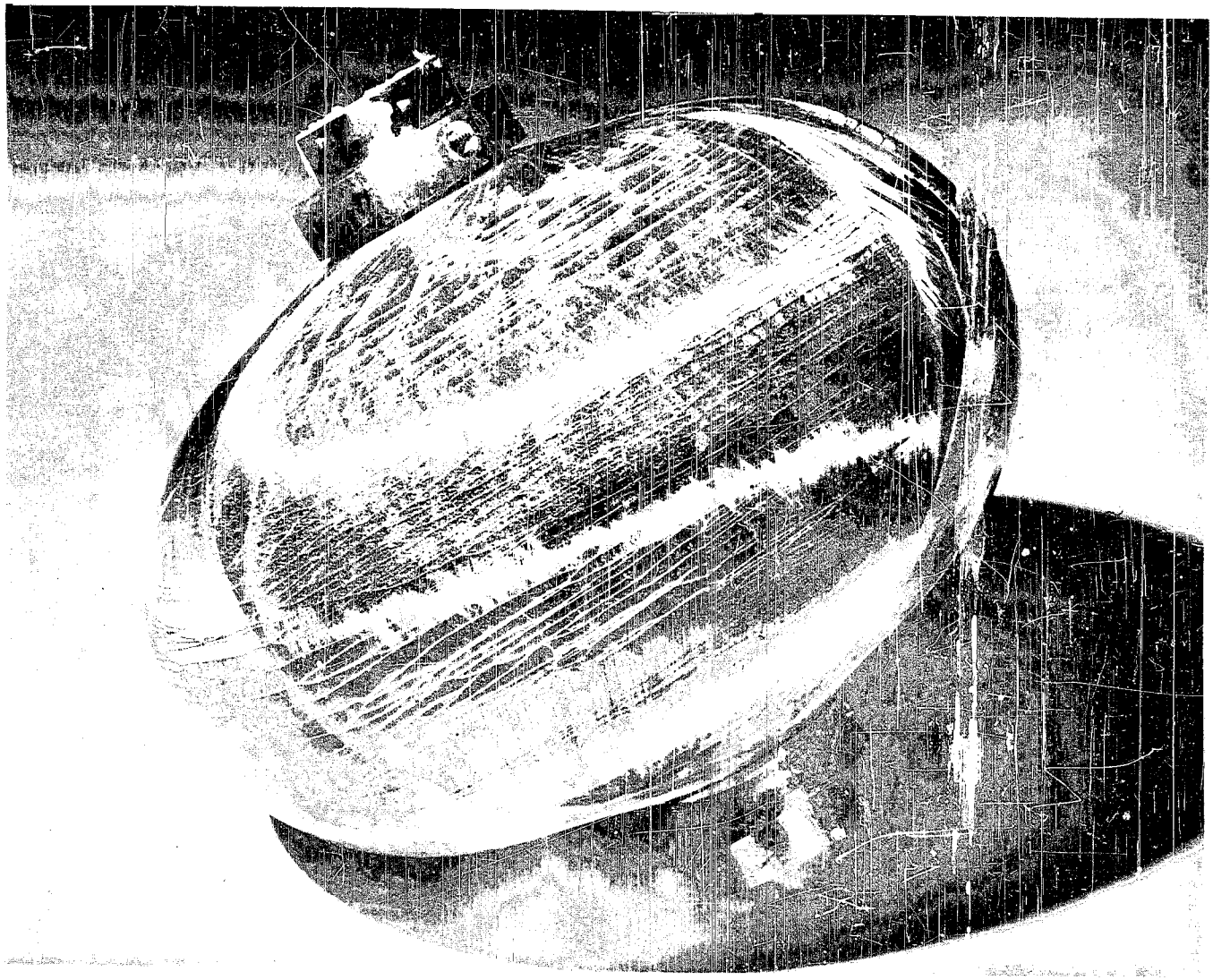

Figure 55. Isotensoid Internal Pressure Vessel After Failure

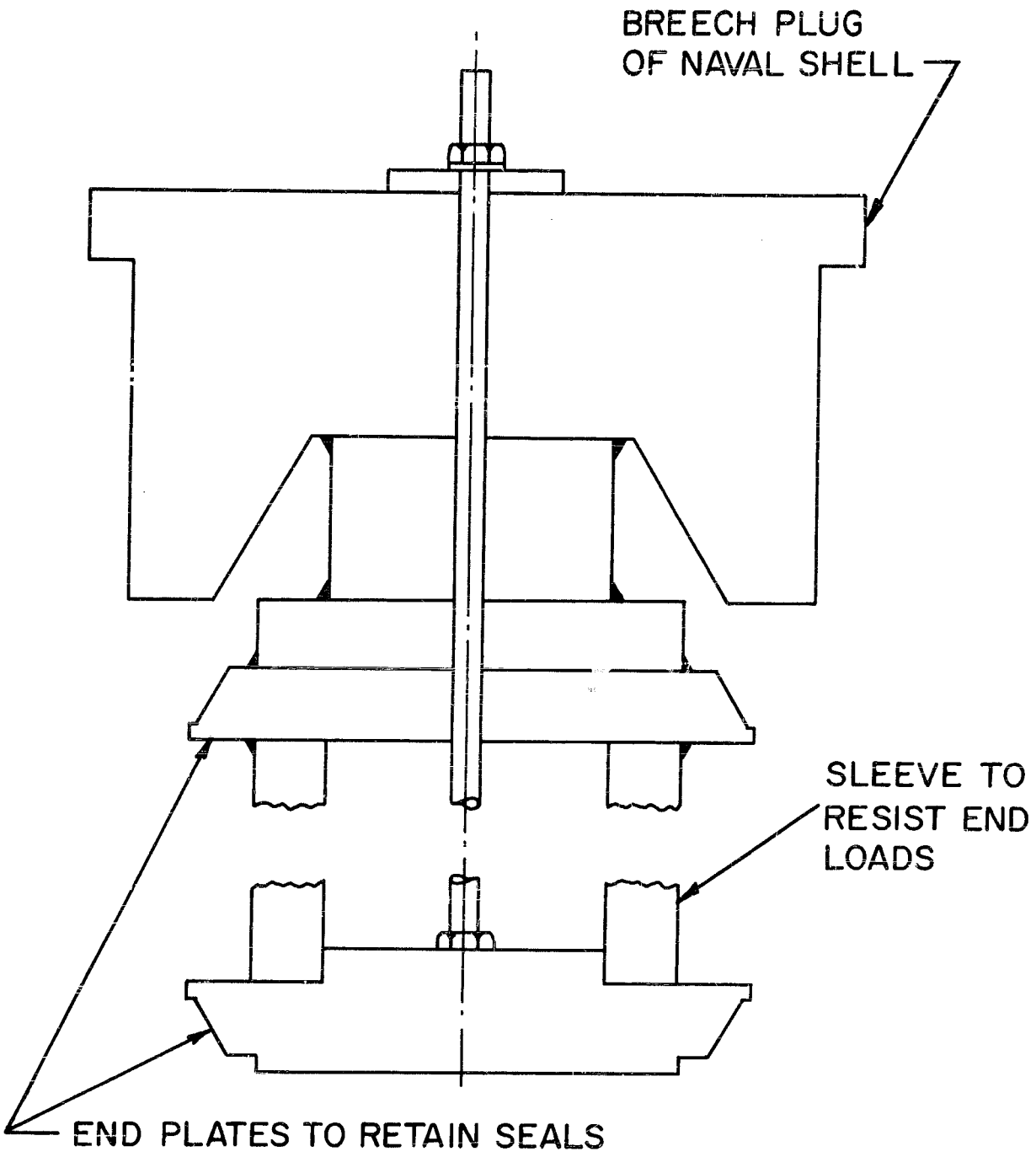

Fig. 56. Hydrostatic Test Fixture

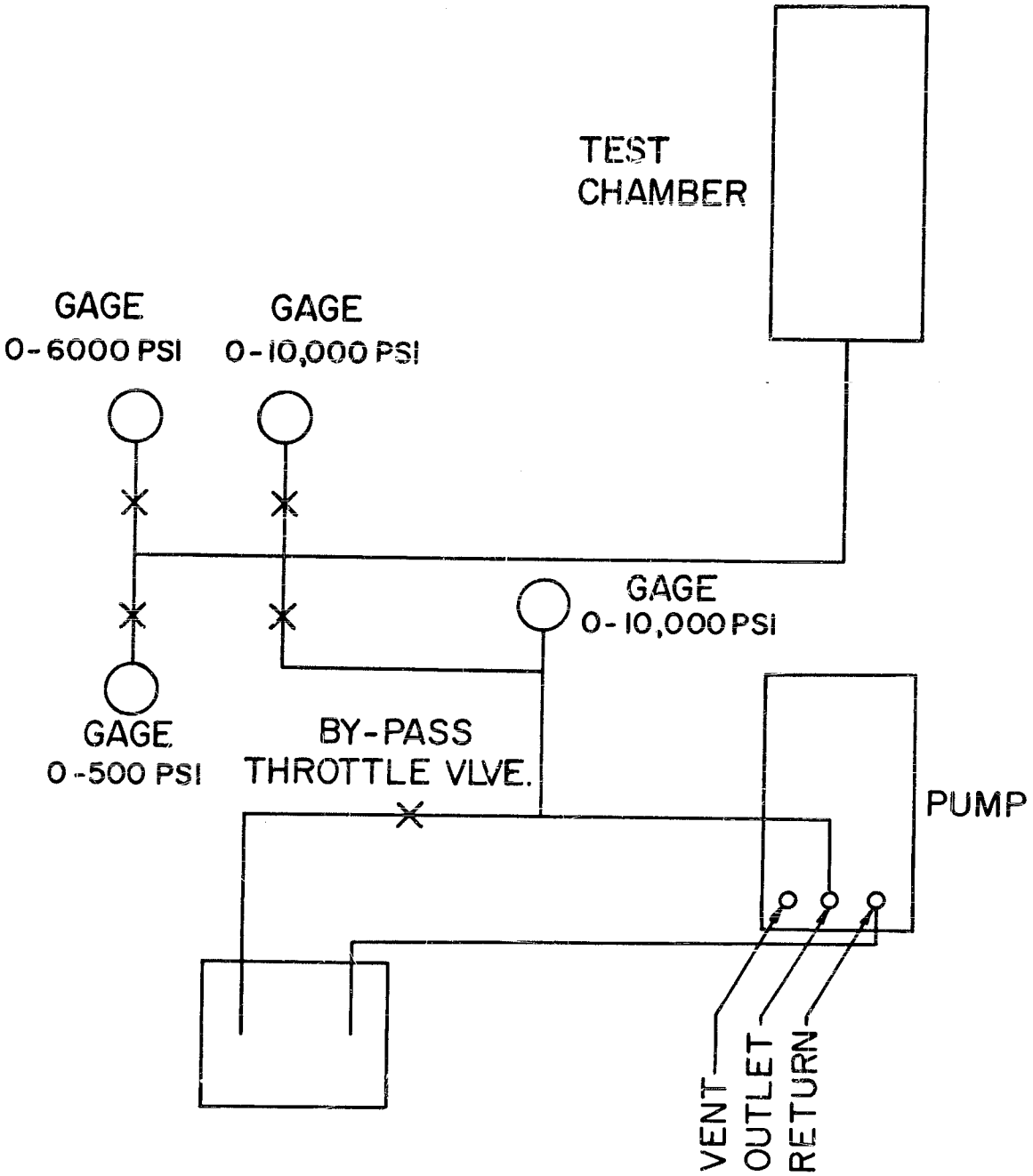

Fig. 57. Schematic of Pressure System

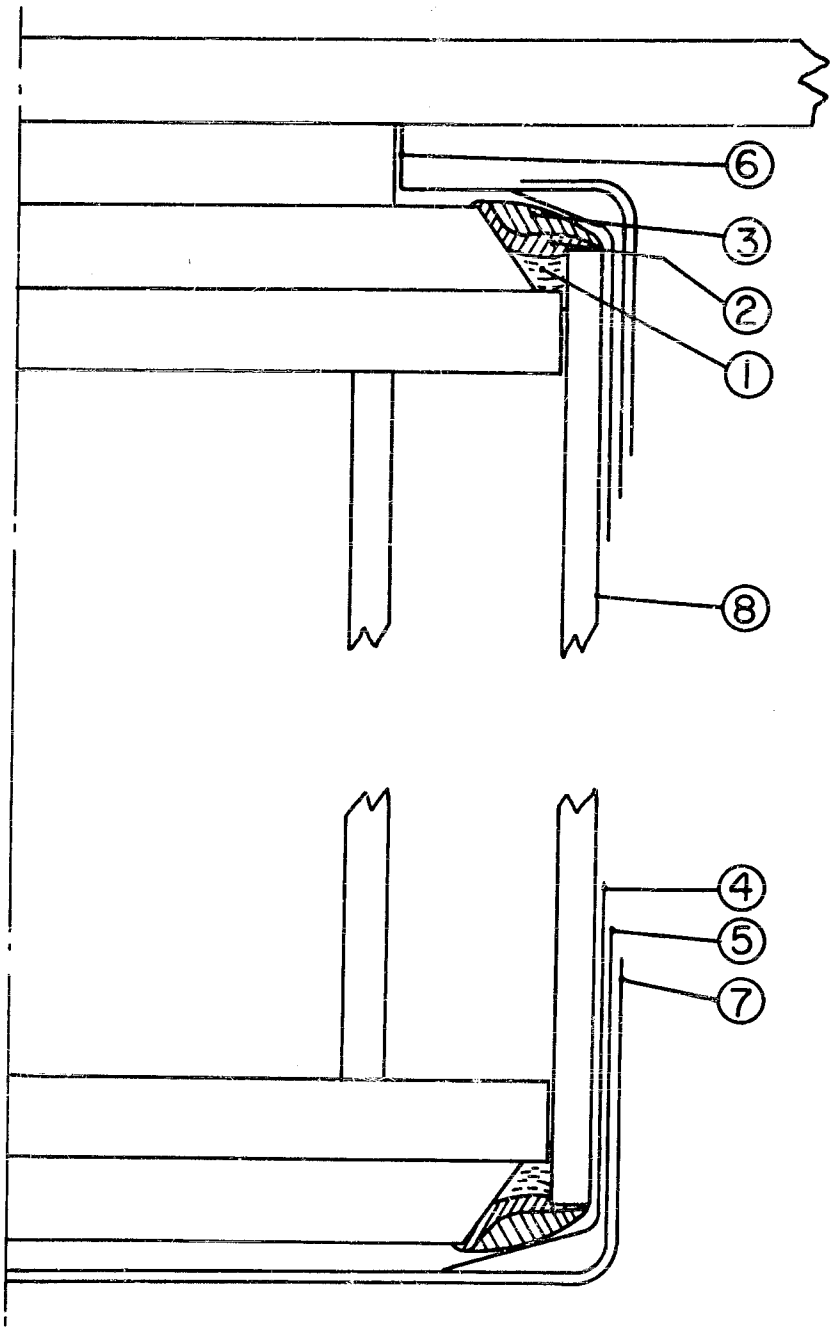

Fig. 58. Seal Systems for Thick-Wall Shells (see table 13)

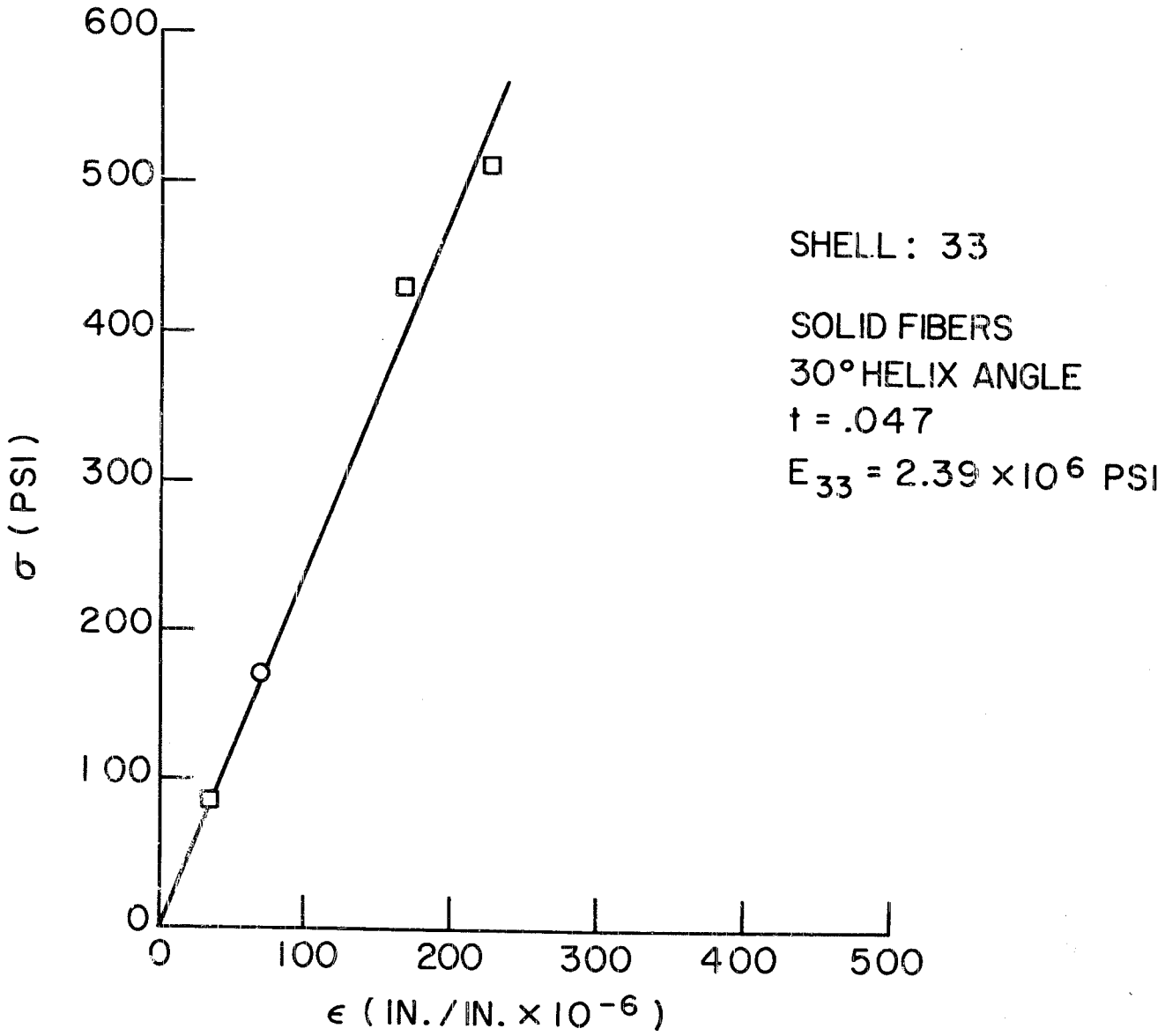

Fig. 59. Circumferential Stress-Strain Data for Hydrostatic Pressure Test.

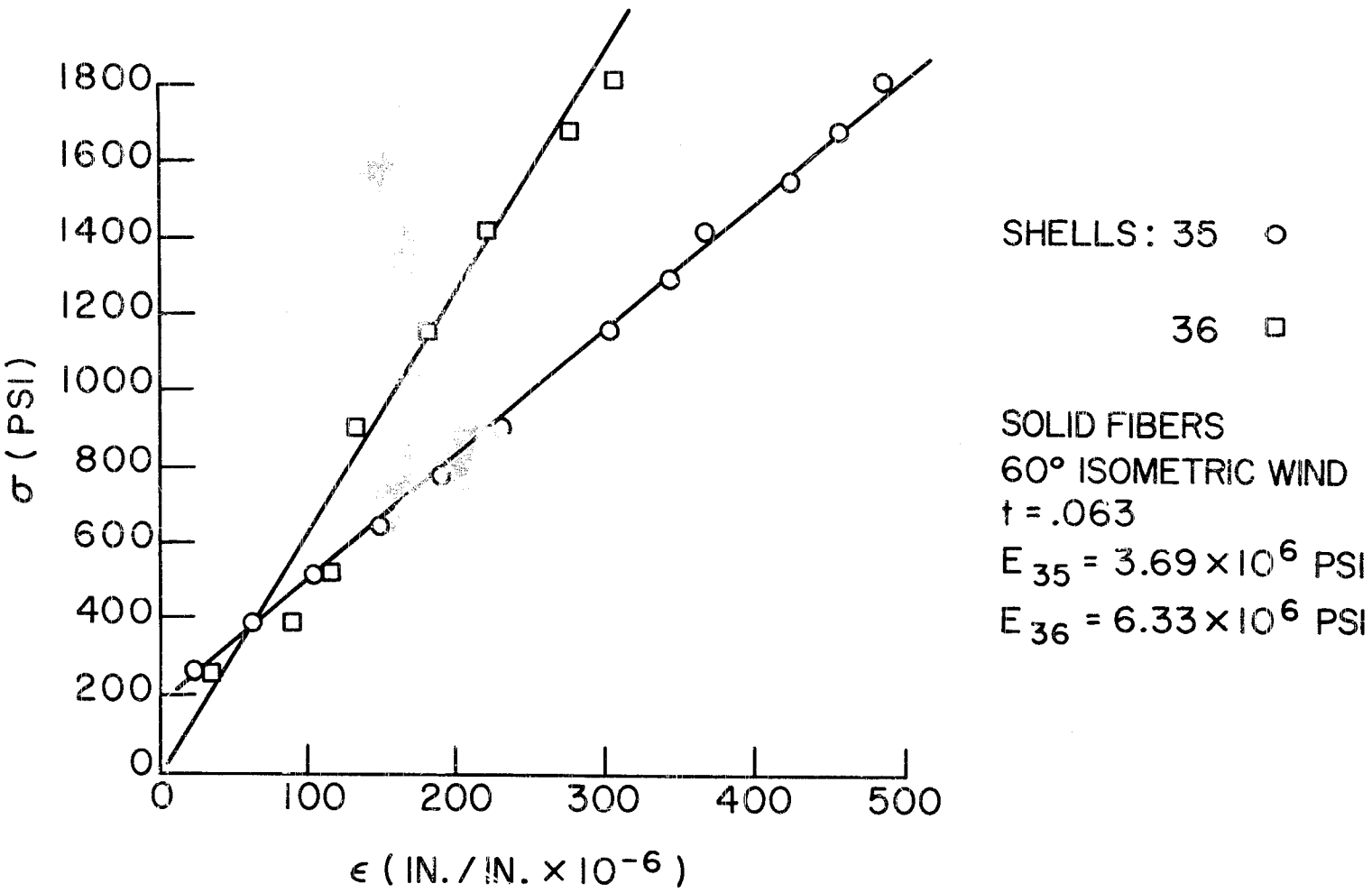

Fig. 60. Circumferential Stress-Strain Data for Hydrostatic Pressure Test. Shell No. 35 & 36

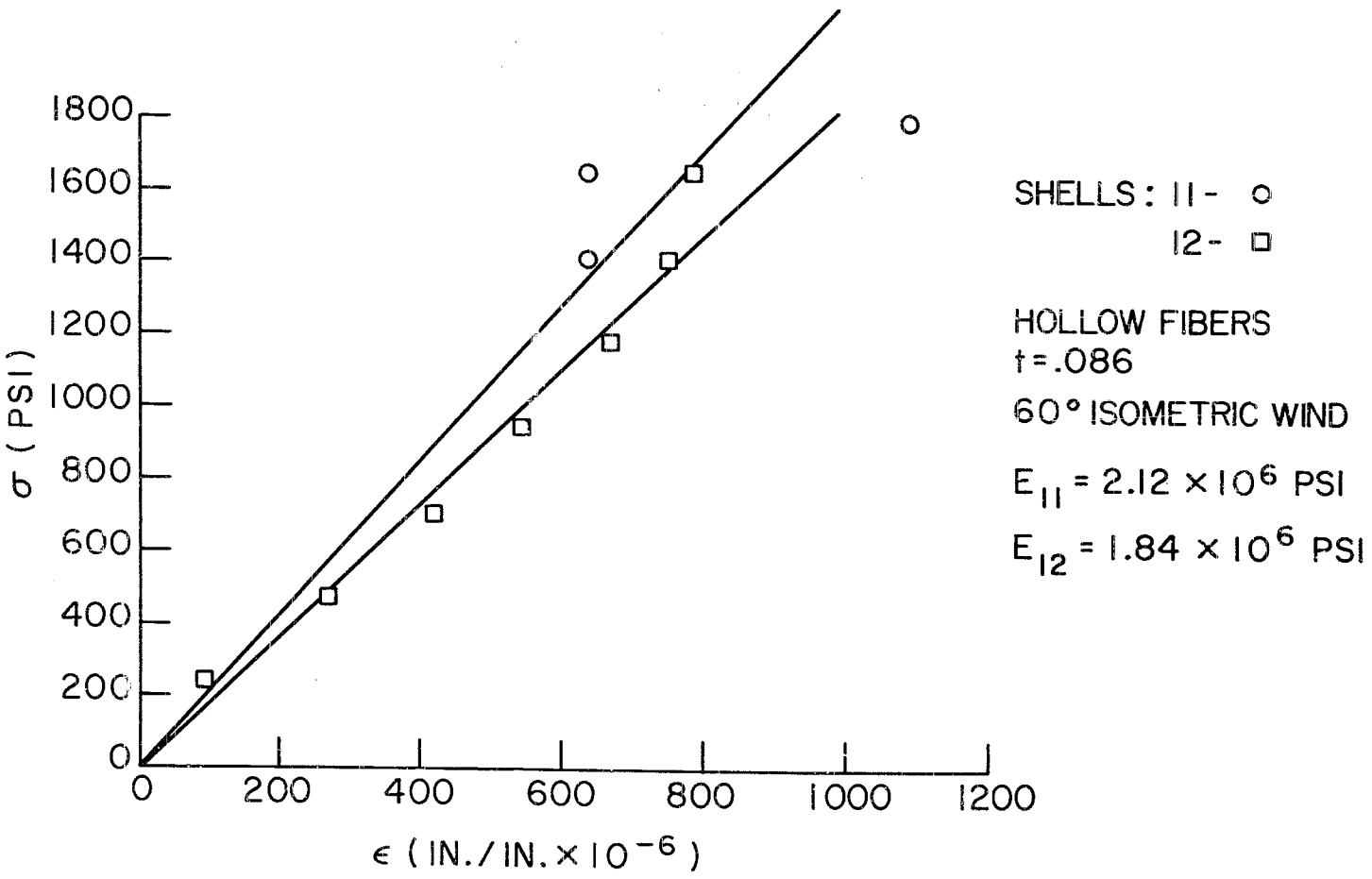

Fig. 61. Circumferential Stress-Strain Data for Hydrostatic Pressure Test. Shell No. 11 & 12

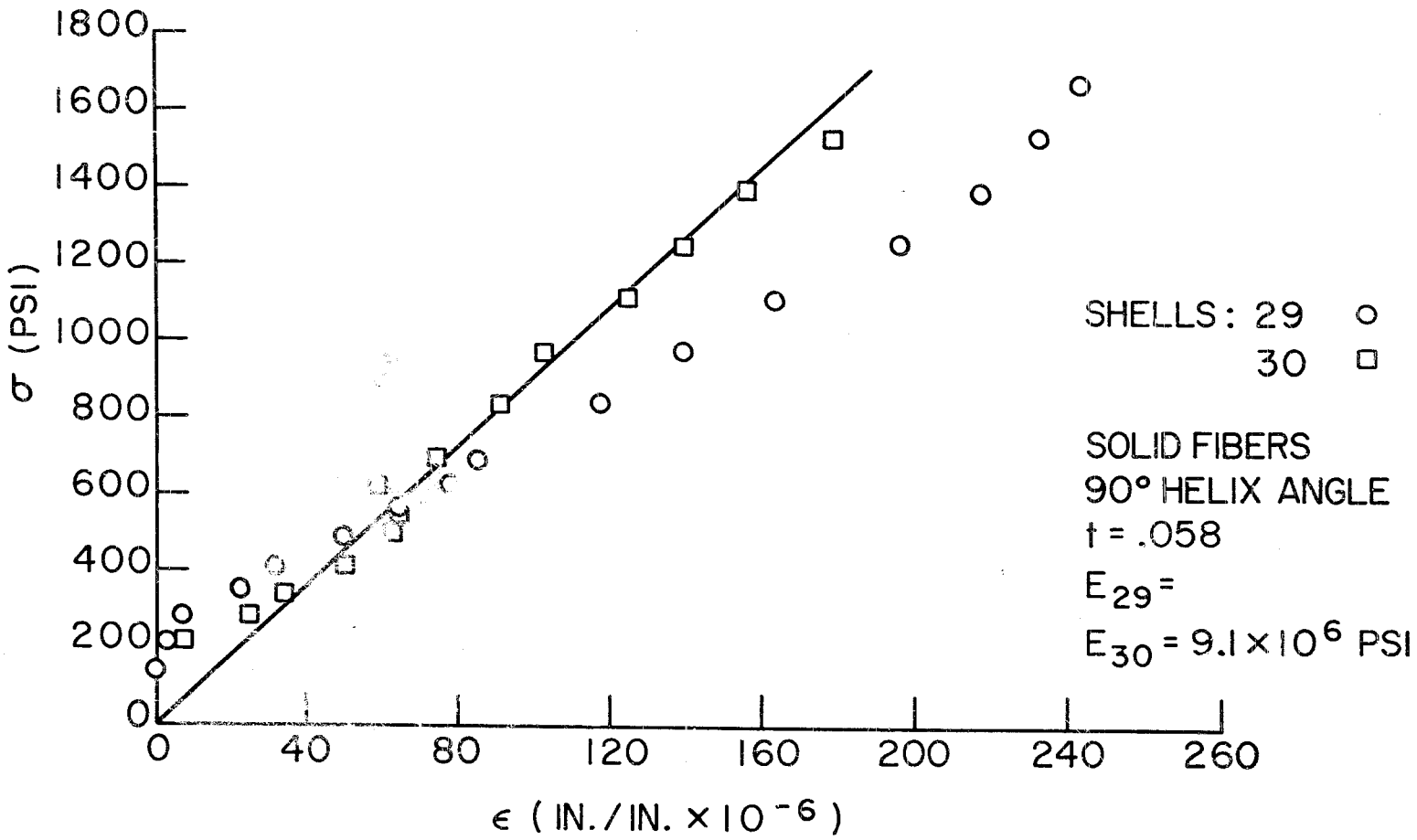

Fig. 62. Circumferential Stress-Strain Data for Hydrostatic Pressure Test. Shell No. 29 & 30

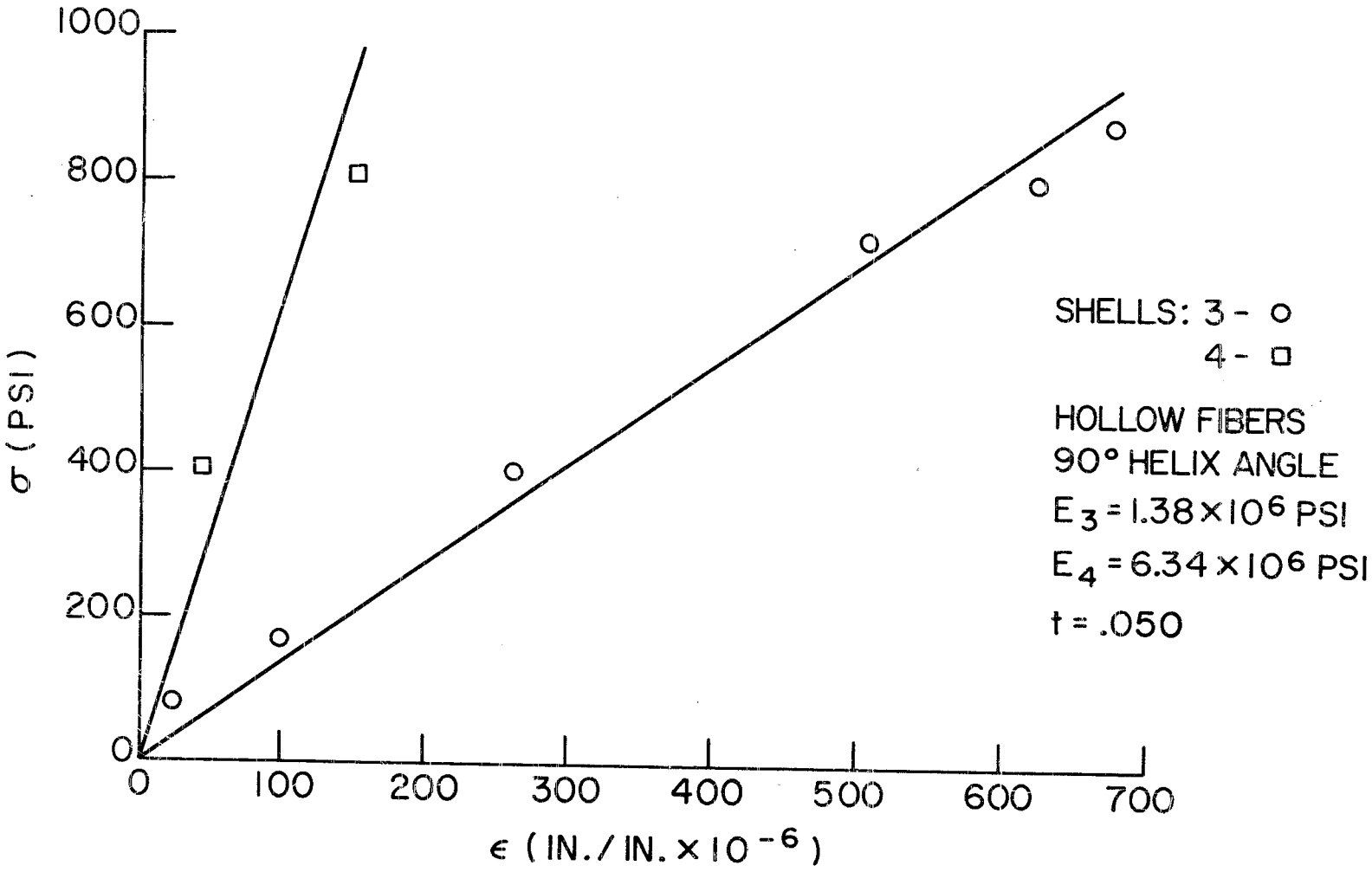

Fig. 63. Circumferential Stress-Strain Data for Hydrostatic Pressure Test. Shell No. 3 & 4

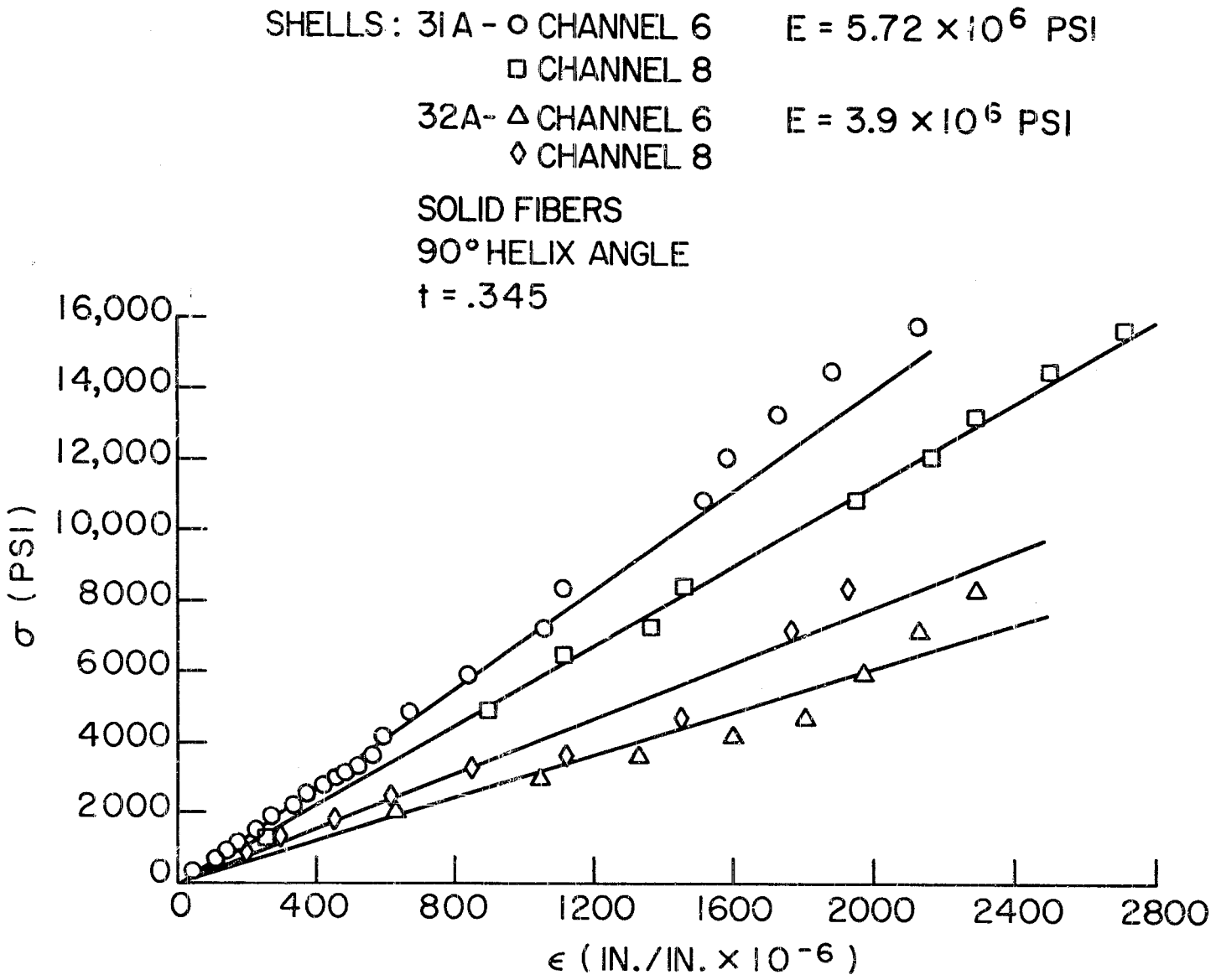

Fig. 64. Circumferential Stress-Strain Data for Hydrostatic Pressure Test. Shell No. 31A & 32A

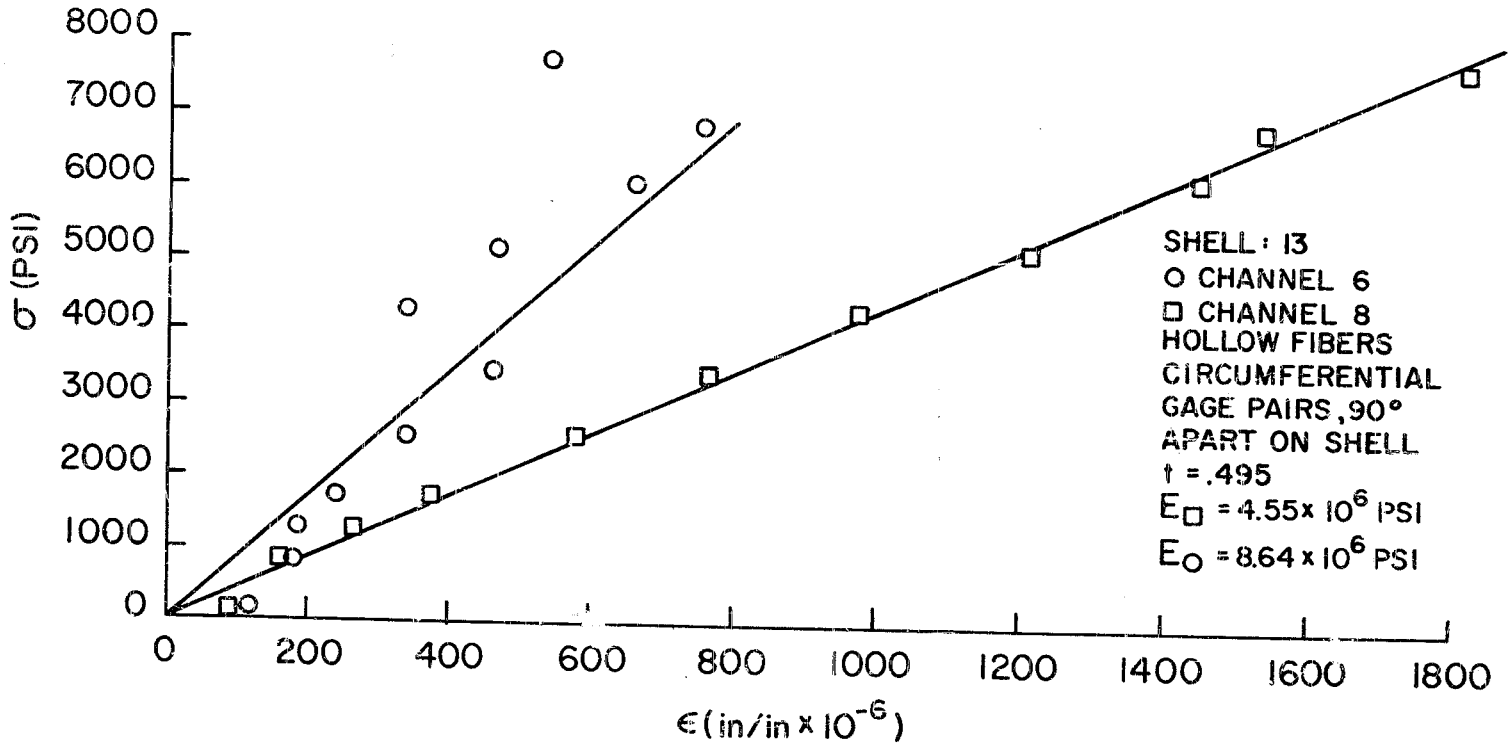

Fig. 65. Circumferential Stress-Strain Data for Hydrostatic Pressure Test. Shell No. 13

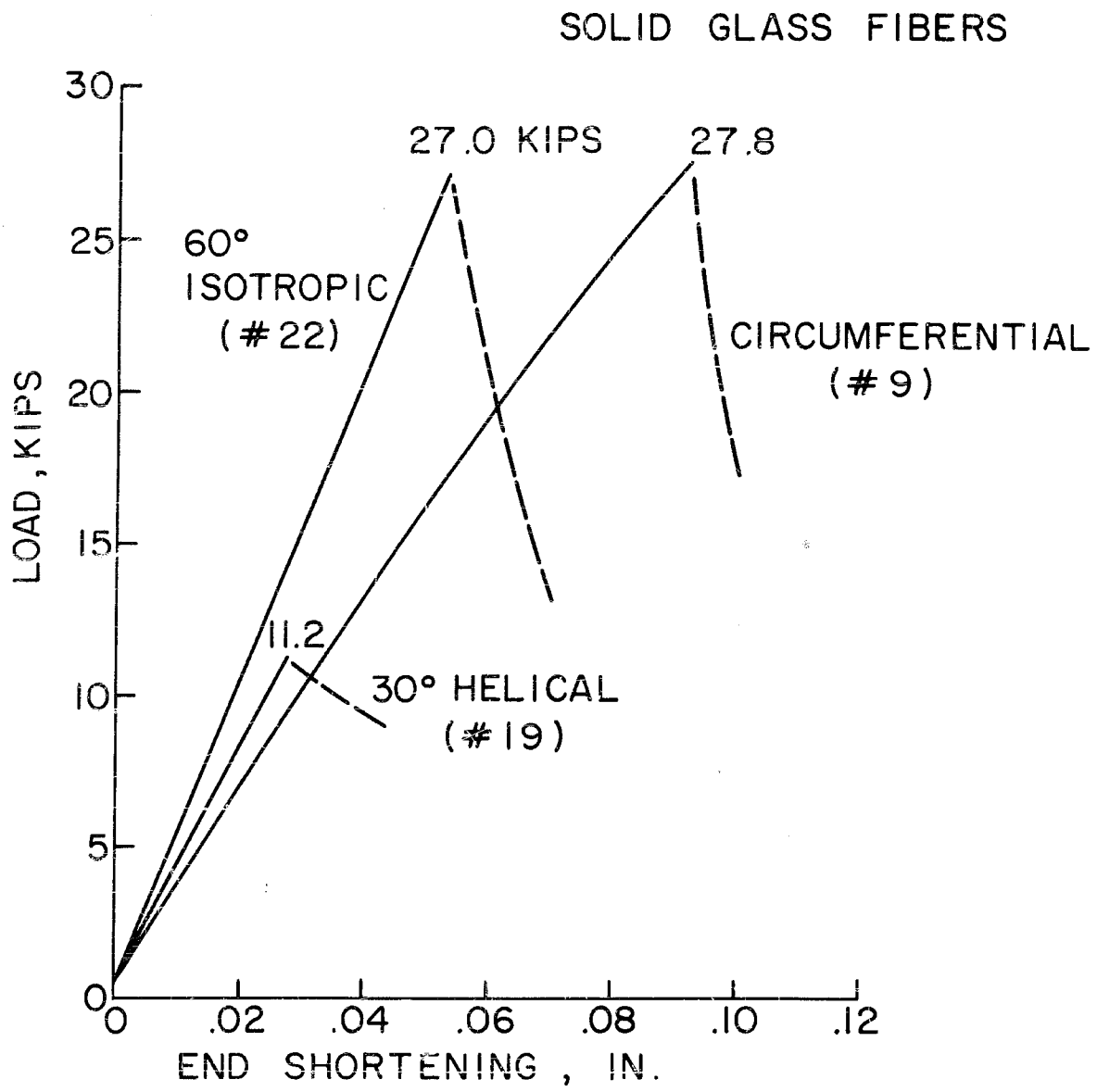

Figure 66. Longitudinal Stress-Strain Data for Axial Compression Tests
a. Solid Fiber Cylinders

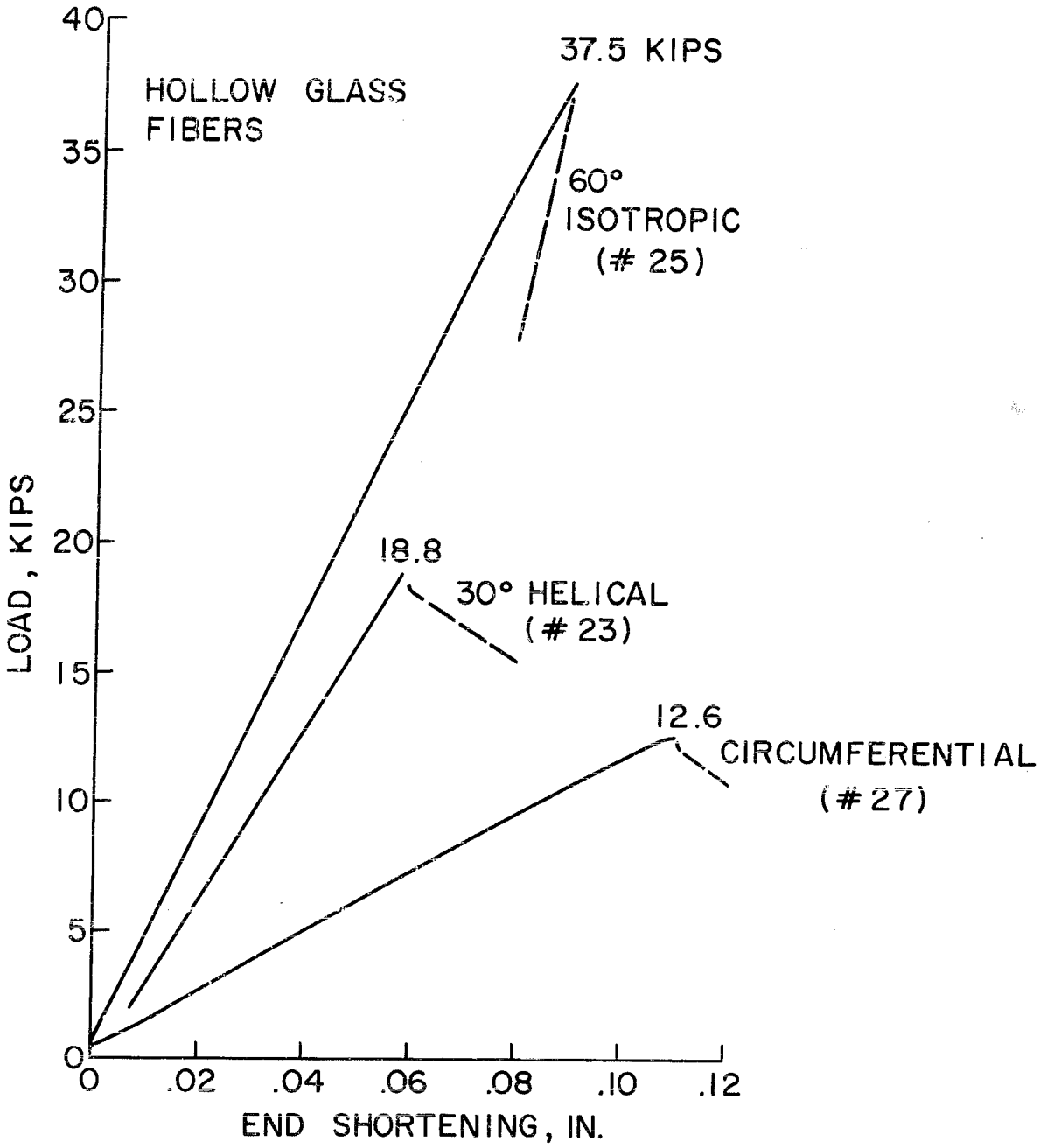

Figure 66. Longitudinal Stress-Strain Data for Axial Compression Tests
b. Hollow Fiber Cylinders

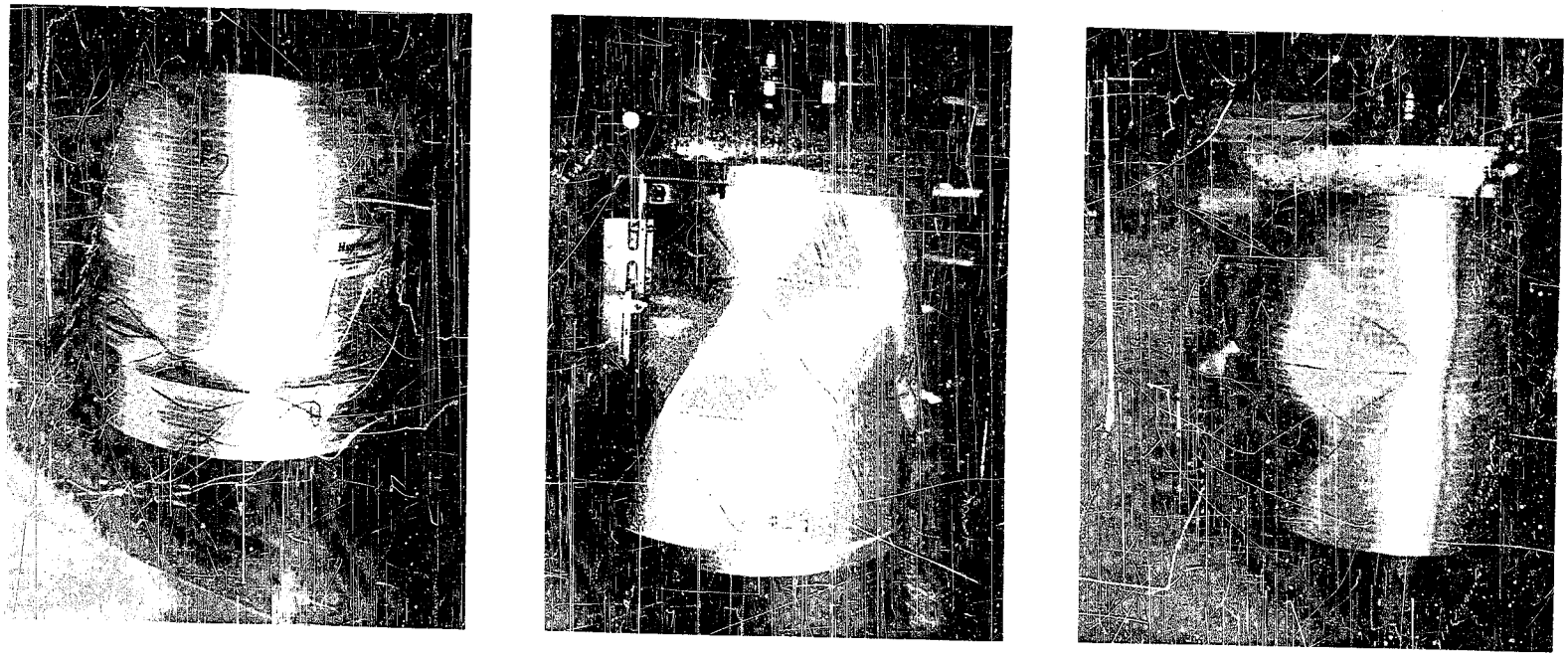

Circumferential

30° Helical

60° Isotropic

Figure 67. Test Specimens After Failure
a. Solid Fiber Cylinders

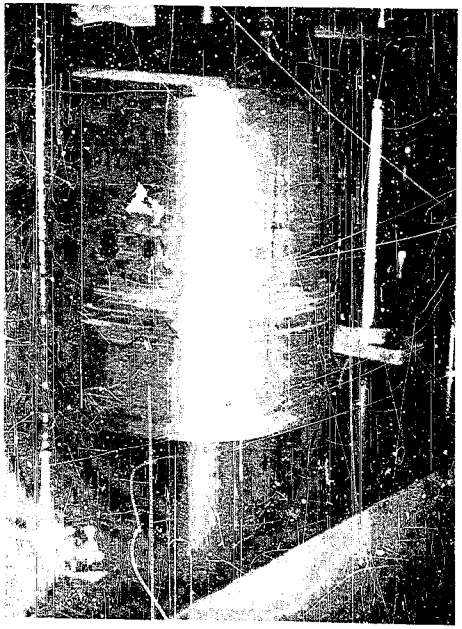

Circumferential

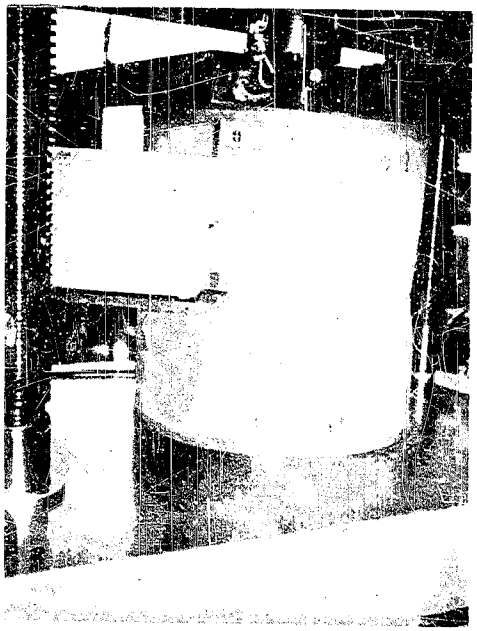

30° Helical

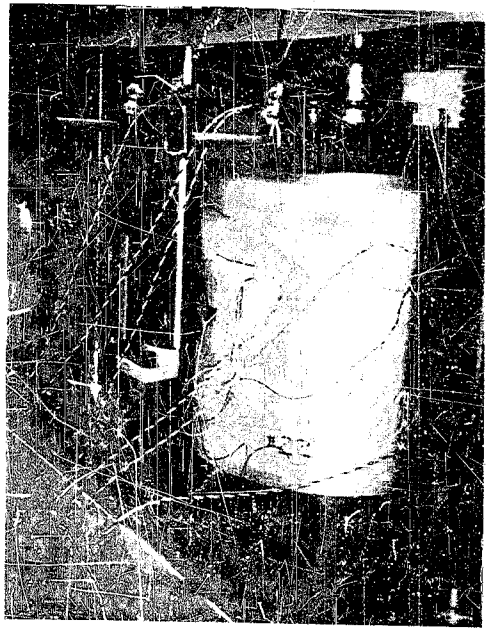

60° Isotropic

Figure 67. Test Specimens After Failure
b. Hollow Fiber Cylinders

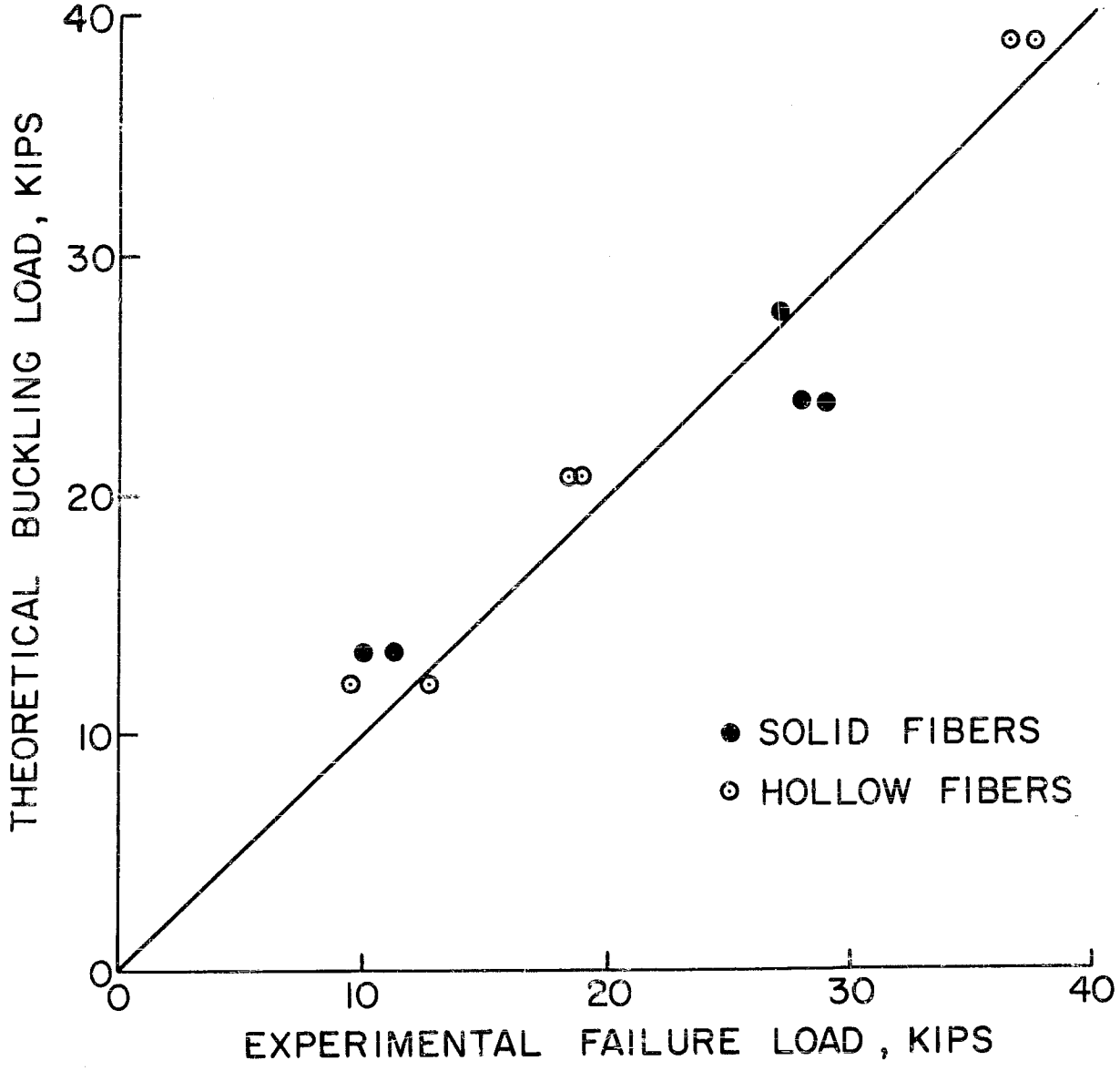

Figure 68. Comparison of Theoretical and Experimental Buckling Loads (45° Line Represents Perfect Agreement)

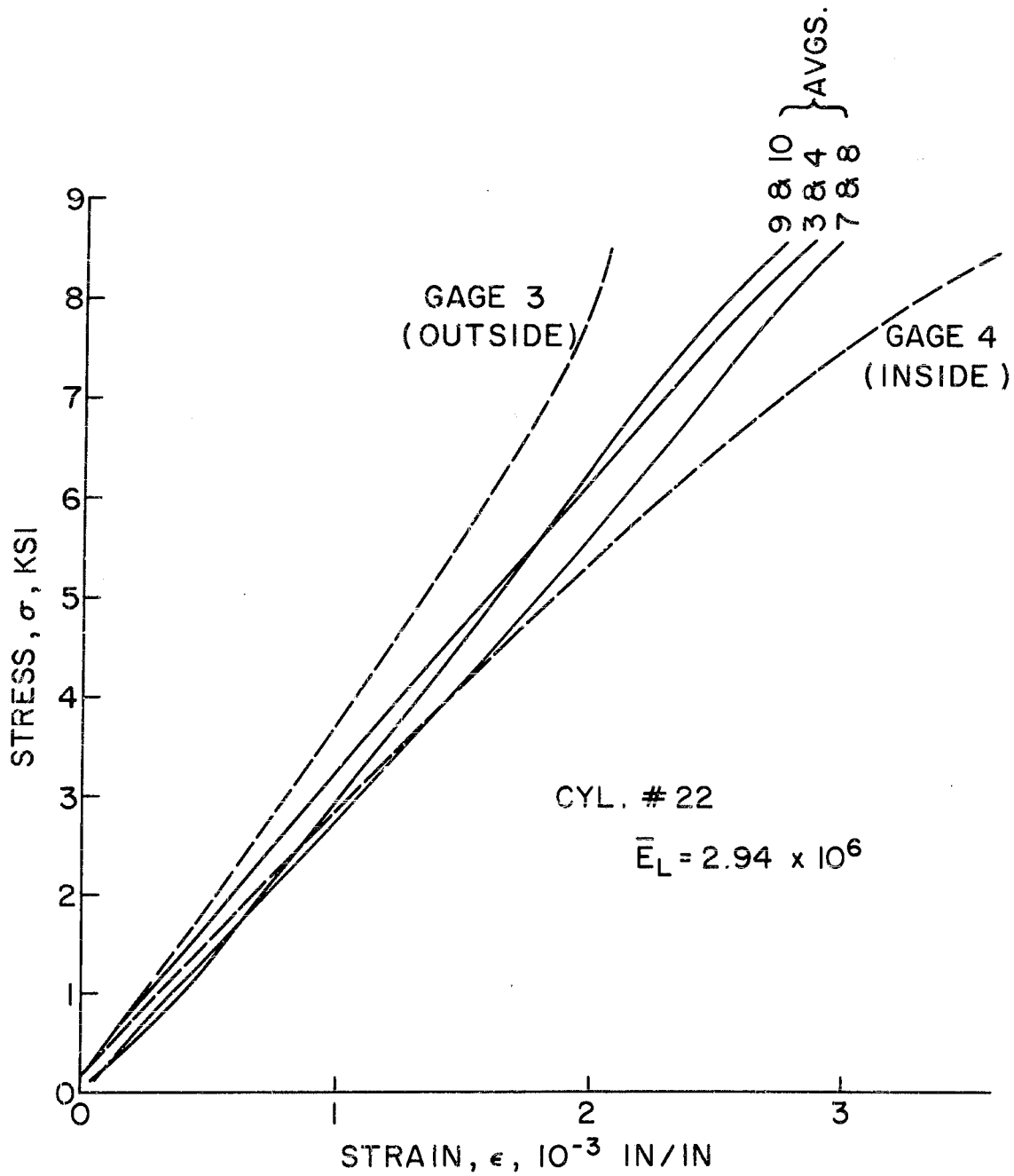

Figure 69. Stress-Strain Data for Typical Cylinder in Axial Compression

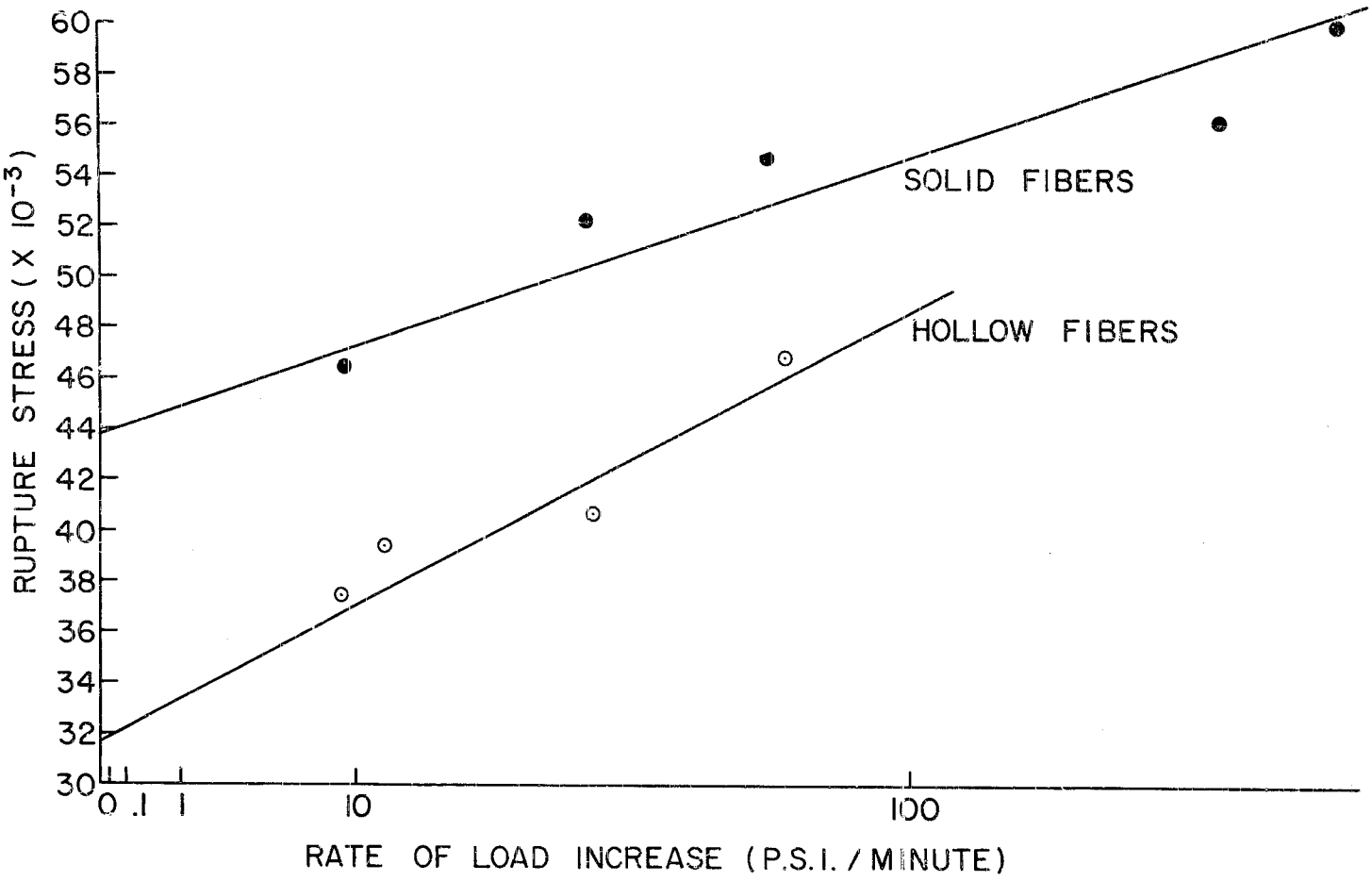

Figure 70. Prot Plot of Rate of Load Increase vs. Rupture Stress

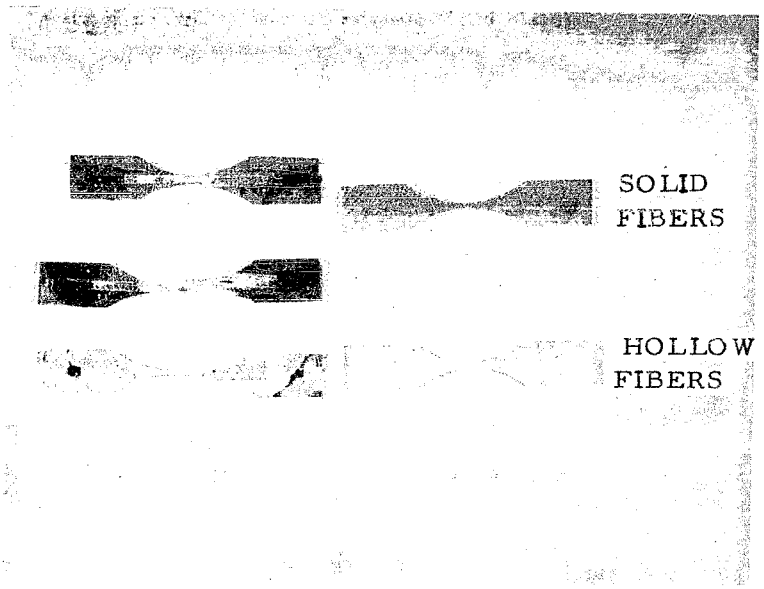

Figure 71. Fatigue Test Specimens

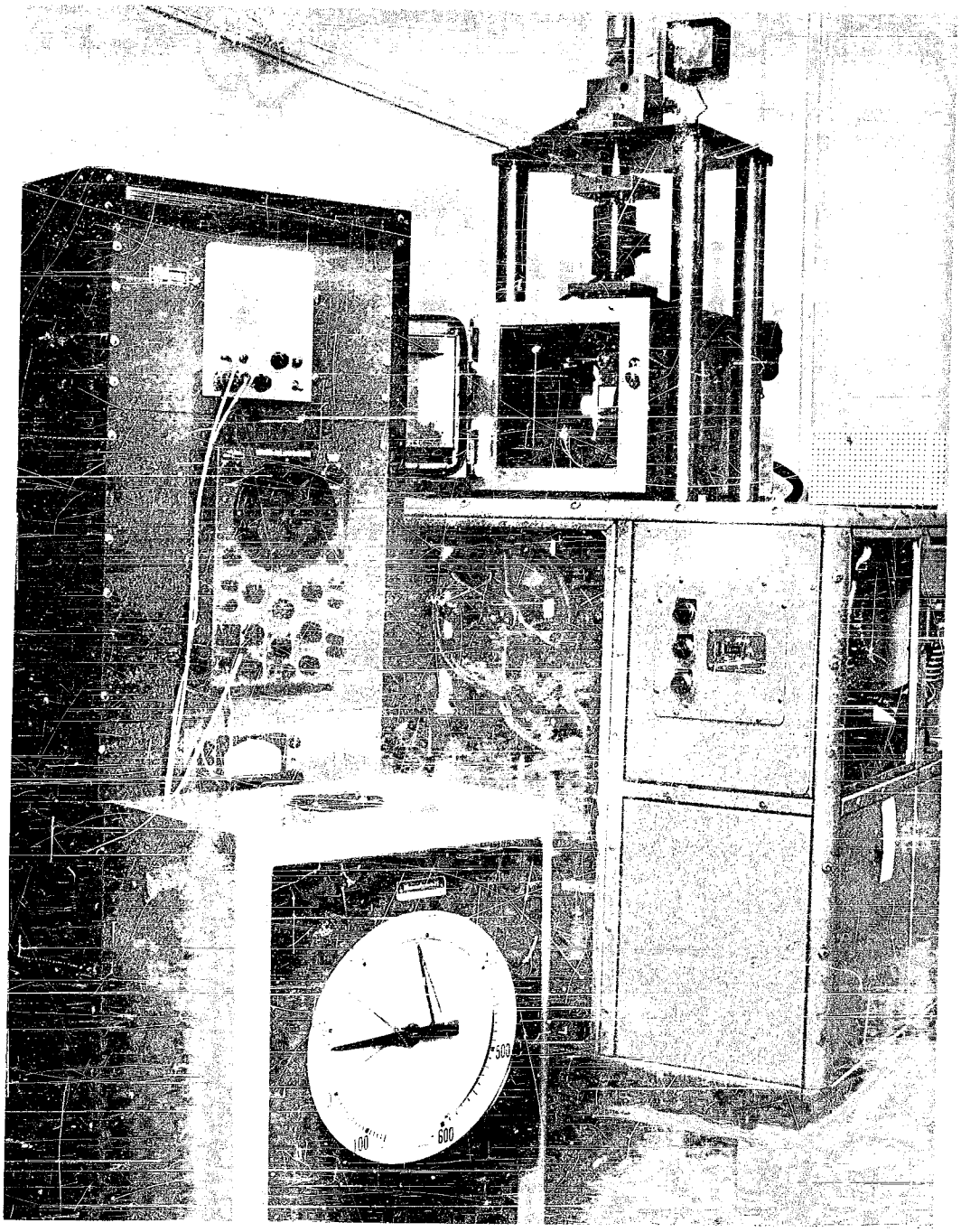

Figure 72. Fatigue Test Set-up

Naval Bureau of Weapons

DISTRIBUTION LIST

External (Contract)

Picatinny Arsenal
Dover, New Jersey
Attn: Mr. J. Matlack

PLASTEC (2)
Picatinny Arsenal
Dover, New Jersey

National Aeronautics and
Space Administration
Washington 25, D. C.
Attn: B. Achammer

Ordnance Materials Research
Watertown Arsenal
Watertown 72, Massachusetts

Office of Naval Research
Material Sciences Division
Washington 25, D. C.

David Taylor Model Basin
Carderock Maryland
Attn: Codes 734 and 735

Chief, Bureau of Ships
Washington 25, D. C.
Attn: Code 634C

U. S. Naval Ordnance Laboratory
White Oak
Silver Spring, Maryland
Attn: WM Division

U. S. Naval Research Laboratory
Washington 25, D. C.
Attn: Code 6210

U. S. Naval Ordnance Test Station
China Lake, California
Attn: Code 5557

Commander
Aeronautical Systems Div. (ASRCNC)
Wright-Patterson AFB, Ohio

Commander
Aeronautical Systems Div. (ASRCNF)
Wright-Patterson AFB, Ohio

The B. F. Goodrich Company
Research Center
Brecksville, Ohio
Attn: Mr. C. H. Stockman

Bjorksten Research Lab., Inc.
P. O. Box 265
Madison 1, Wisconsin
Attn: Mr. J. E. Henning

Boeing Aircraft Company
Seattle, Washington
Attn: M. Kushner
Aerospace Division

Allison Division of General Motors Corp.
Indianapolis 6, Indiana
Attn: Mr. R. L. Stedfeld

Massachusetts Institute of Tech.
Plastics Research Laboratory
Cambridge 39, Massachusetts
Attn: F. J. McGarry, Assoc. Prof.
of Materials

Narmco R&D
3540 Aero Court
San Diego 11, California
Attn: Mr. W. Otto

H. I. Thompson Fiber Glass Co.
1733 Cordove Street
Los Angeles 17, California
Attn: Mr. Leon Parker, V. P. Research

External (Contract) cont'd.

General Electric Company
General Engineering Division
Schenectady, New York

A. P. Smith Corporation
P. O. Box 584
Milwaukee 1, Wisconsin
Attn: Mr. Charter

Owens-Corning Fiberglas Corp.
Technical Center
Granville, Ohio
Attn: Mr. F. M. Veasie

Chief, Bureau of Naval Weapons
Special Projects Office
Washington, D. C.
Attn: Mr. H. Bernstein

Chief, Bureau of Naval Weapons
Washington 25, D. C.
Attn: RRMA-32

Westinghouse Electric Corp.
Materials Manufacture Division
P. O. Box 128
Blairsville, Pennsylvania
Attn: Mr. F. L. Orrell

Aerojet-General Corporation
P. O. Box 1168
Sacramento, California
Attn: Librarian

Pittsburgh Plate Glass Company
Glass Research Center
Box 11472
Pittsburgh, Pennsylvania
Attn: Mr. R. F. Siefert

Chief, Bureau of Naval Weapons (20)
Washington 25, D. C.
Attn: DLI-3 (for release to DDC)

UNCLASSIFIED